Towards Understanding Nonlinear Wave Propagation in Three-Dimensional Microscale Granular Crystals

Morgan Hiraiwa

A dissertation
submitted in partial fulfillment of the
requirements for the degree of

Doctor of Philosophy

University of Washington

2020

Reading Committee:

Nicholas S. Boechler, Chair

Junlan Wang

Jonathan T.C. Liu

Program Authorized to Offer Degree:

Mechanical Engineering

University of Washington

Abstract

Towards Understanding Nonlinear Wave Propagation in Three-Dimensional Microscale Granular Crystals

Morgan Hiraiwa

Chair of the Supervisory Committee:

Professor Nicholas S. Boechler

Department of Mechanical Engineering

Elastic waves and vibrations play central roles in numerous engineering fields and technologies such as impact mitigation, vibration isolation, ultrasonic imaging, and even electronic filtering components. Enhanced control over such dynamics has the potential to enhance existing applications or create entirely new technologies, with one avenue of such control being waveform manipulation using dispersion and nonlinearity. An attractive approach that has seen significant advancement recently is the field of phononic crystals and acoustic metamaterials, which use structure to tailor existing, and enable new, effective material properties. One such structure is the granular crystal, defined as ordered arrays of discrete elastic particles in contact, which supports dispersion tailoring in addition to nonlinearity resulting from the contact mechanics between the particles. This interplay between dispersion and nonlinearity has produced a large amount of research recently, however, it has mostly been limited to macroscale systems with millimeter to centimeter-sized spheres. Such macroscale systems have limited applicability to many engineering solutions with size and weight constraints. Using microscale spheres to create architectured material with enhanced functionality is a promising idea, however, the dynamic behavior can not be assumed to be identical to

macroscale systems because different physics are expected to become important at small scales, the most consequential being adhesive forces. This work experimentally investigates whether three-dimensional microgranular crystals support nonlinear dynamics analogous to their macroscale counterparts, which is currently an open question. Key elements known to allow wave tailoring in macroscale systems are studied individually before building up to direct analysis of nonlinear dynamics in three-dimensional microgranular crystals. First, a two-dimensional microgranular crystal monolayer adhered to a substrate is utilized to investigate, within linear dynamical regimes, interparticle vibrational modes and horizontal-rotational degrees of freedom, both known to affect propagation in three-dimensional systems. Using this experimental design, horizontal-rotational interparticle modes were observed, and described by a recently developed unified theory, for the first time in a microgranular crystal, with the key takeaway being that adhesive forces enhance the role of rotations and form interparticle networks that drastically alter the mode frequency. Next, the contact mechanics of a microsphere monolayer was studied with three different methods of estimating the adhesive force and compared by assuming an elastic contact mechanics model. This unique comparison found the measurements varied widely, suggesting adhesion-induced plasticity may play a major role for polymer microspheres. Subsequently, the behavior of a disordered three-dimensional assembly of microspheres was explored by controlling static and dynamic loading amplitudes, which directly reveal the nonlinear nature of the contact and the weakly nonlinear dynamics that result from it. It was discovered that the nonlinear behavior was drastically different from macroscale counterparts initially, however, the behavior was approximately similar after mechanical conditioning. Lastly, strongly nonlinear dynamics of an ordered three-dimensional microscale granular crystal was investigated in a preliminary study by characterizing the dependence of sound speed on acoustic wave amplitude and found to behave approximately similar to macroscale systems, though additional data is needed for a rigorous analysis. This finding bodes well for translating the promise of macroscale

granular crystals to the microscale. The work contained in this thesis lays out a path to exploring even more complex microgranular crystal dynamics.

TABLE OF CONTENTS

LIST OF FIGURES

LIST OF TABLES

DEDICATION

To my family and loved ones.

ACKNOWLEDGMENTS

Countless individuals have made my success possible, more than can be given fair recognition here, but what follows is my attempt. I could not have possibly asked for a better advisor than Dr. Nicholas Boechler, who has spent vast amounts of energy in training me to think critically, while simultaneously giving me the intellectual space to learn and explore on my own. Most of all, completion of the PhD program would have been impossible without his foremost concern for my personal well-being, and for that I consider him a friend in addition to a mentor. I'd like to thank my committee, Prof. Junlan Wang, Prof. Jonathan Liu, and Prof. Arka Majumdar, for their effort in helping me through this process. I've also had the pleasure of collaborating with Prof. Wang, whose guidance was critical to my success, in addition to use of her laser equipment. Dr. Alex Maznev offered his vast knowledge on countless questions throughout my academic career. Dr. Nicolas Vogel, a premier expert in self-assembly, was key to the fabrication processes used in much of my research. Additionally, past members of the Wave-Material Interaction Lab have be instrumental in everything I've learned. Dr. Maroun Abi Ghanem, who entered the lab as postdoc about a year after I joined, shared his extensive knowledge in photoacoustics when I was still a novice and helped guide me through the process of earning my degree. Dr. Sam Wallen was always capable of tackling even the most difficult analytical and numerical questions I could throw at him, and my publications would not have been possible without his modeling brilliance. Dr. Amey Khanolkar, who spent endless hours with me in G4 while we bootstrapped our optical skills from scratch, was always available to discuss ideas and assist with challenging problems. Outside the Wave-Material Interaction Lab, Melicent Stossel in the Wang Research Group

also provided essential support in designing and running experiments with equipment and techniques I was unfamiliar with. Beyond technical assistance, these individuals formed an environment where wild ideas flowed freely, and scientific endeavors truly felt like an exploration into the unknown. I'd also like to express my deepest gratitude to Wanwisa Kisalang, who helped me navigate the many administrative steps along the way and smoothed out any complications that arose.

My family's support through all of my education, and their unwavering confidence in my abilities, propelled me from a near high school dropout to holding a doctorate. At times it has felt as though that belief was misguided, but they turned out to be correct all along. My father provided me with the practical knowledge and intuition into mechanical systems that was the foundation to my technical knowledge, and my mother's relentless positivity kept my motivation from collapsing even during the bleakest times. My sister was always there to provide a moment of respite when I grew tired from running and analyzing experiments. My grandfather John helped fuel my intellectual curiosity at an early age and, little did I know, his monologues encompassing seemingly random scientific discoveries would set me on this trajectory. My grandmother Penny provided that special brand of wholesome encouragement that only a grandmother can. Finally, not least of all, is Alison Lo, whose tireless free spirit has remained a source of inspiration to all my pursuits, scholarly or otherwise.

Chapter 1

INTRODUCTION

1.1 Motivation

From sound waves traveling through air as a family sings happy birthday, to atomic lattice vibrations transporting heat in a computer's microprocessor, mechanical waves are ever present whether we notice them or not. In some cases, mechanical waves, and the energy they carry, are something that needs to be minimized. Sound isolation in homes, vehicles, and industrial processes aims to either reflect incoming acoustic waves or convert the energy into heat [1]. Concrete walls in an apartment complex have such a large impedance mismatch with air that they reflect most acoustic energy. Many mufflers are designed to act as acoustic resonators which force sound waves to reflect internally multiple times, during which acoustic energy is partially converted to heat before exiting the tailpipe [2]. Isolation of elastic waves traveling through solid material is similarly important for operation of reciprocating machinery, where selection of the material used to mount or secure the reciprocating components can minimize harmful vibrations [3–5]. Impact mitigation, which is simply the management of high amplitude transient elastic waves, is an age-old application still pursued with great interest today [6], from protective gear for soldiers [7] or athletes [8,9] to vehicular safety [10–12] and even spacecraft shielding from micrometeoroids [13].

In other cases, mechanical waves are necessary and leveraged as tools to perform various goals, such as acoustic imaging and sensing technologies. Medical ultrasound is an essential technique for imaging the human body using acoustic waves reflecting off different types of

tissue to produce spatial information in a sonogram [14, 15]. This same approach is used to image solid materials in a technique called Non-Destructive Testing (NDT) that can detect flaws and cracks in structural components such as beams and welds [16, 17]. When small wavelength acoustic pulses are used to image tissue biopsies and cells or flaws within microchips, the technique is called acoustic microscopy [18, 19]. Not only does acoustic imaging allow visualization of spatial informational, but mechanical properties can also be extracted in some schemes [20]. At the other end of the spectrum, with much longer wavelengths, Sonar is used for locating the position of large objects, typically underwater [21].

Mechanical waves can also be used to impart energy into objects remotely to perform various tasks. When used in medicine, this is called therapeutic ultrasound which has seen growing number of applications [22–24], most of which rely on focusing the acoustic waves to a point. One of the more common uses, called extracorporeal shockwave therapy [25], is for noninvasive pulverizing of kidney or gallstones such that fragments can be passed out of the body naturally. Another application is for localized heating of tissue within the body, called high intensity focused ultrasound [26], which can be used to ablate tumors. Various other medical uses have been proposed, such as sonodynamic therapy which uses ultrasound to locally activate drugs [23]. Applying force to small objects through acoustic waves has seen an explosion of research in a technique called acoustic tweezers, in which microscopic mechanical measurements can be obtained or continuous cell sorting by size and weight can be achieved [27]. At extremely high amplitudes, solid objects can be joined through a process called ultrasonic welding [28], which causes localized heating and melting at material interfaces, typically for polymers and low melting temperature metals.

In terms of impact on our everyday lives, the most widespread application of acoustic waves in elastic materials are surface acoustic wave (SAW) and bulk acoustic wave (BAW) filters [29], which are used for radio frequency signal conditioning in mobile devices. These filters convert electronic signals into acoustic waves through electrodes on piezoelectric materials then back to electronic signals. By designing the electrode geometry in a specific way, only a narrow

frequency band is efficiently excited and detected, allowing for passive filtering at a cost and form factor that continues to dominate the mobile device industry today [30]. Whether the goal is minimizing of transmission or utilization as a tool, mechanical waves are vital in a wide array of research and applications. From the perspective of engineering, control over mechanical waves has the potential to enhance existing applications or, with sufficient ingenuity and scientific breakthroughs, create entirely new technologies.

1.2 Mechanical Waves and Dispersion

When exploring how mechanical waves can be manipulated, consider the famous tag line from Ridley Scott's classic sci-fi film *Alien*: "In space no one can hear you scream". This provides a succinct, albeit unnerving, recognition that all mechanical disturbances such as acoustic waves require matter to support propagation, which in the vacuum of space, there is little-to-none. Since matter is a requirement, and all matter has mechanical properties, manipulation of acoustic waves can be achieved through material property tailoring, with one avenue being sound speed and dispersion.

In the context of acoustics, dispersion is a non-constant sound speed, or strictly speaking a phase velocity c_p, that depends on wavelength λ. The equation for phase velocity is generalized to account for this dependence $c_p(\lambda) = f(\lambda)\lambda$, where $f(\lambda)$ is the wavelength-dependent frequency. An equivalent representation that's typically preferred in acoustic analysis is $c_p(k) = \omega(k)/k$, where k is the wavenumber defined as $k = 2\pi/\lambda$ and $\omega(k)$ is the wavenumber-dependent angular frequency. In simple terms, a sound speed that changes with acoustic wavelength causes a broadband pulse made up of many wavelengths to spread out in space and time, i.e., it "disperses" as it propagates.

To better understand dispersive properties, it's instructive to first review non-dispersive waves, where the sound speed is a constant, independent of frequency or wavelength [31]. The one-dimensional longitudinal wave equation, assuming no amplitude dependence or dissipation, is given by Eq. 1.1, where u is particle displacement. The relationship between

sound speed, frequency, and wavenumber can be graphically understood through a dispersion relation, which plots frequency as a function of wavenumber $\omega = \omega(k)$. Since c_p is constant for a nondispersive medium, the dispersion relation is simply a straight line, where the phase velocity at any wavenumber is the slope of a line connecting $\omega(k)$ and the origin, shown in Fig. 1.1(a).

$$\frac{\partial^2 u}{\partial t^2} = {c_p}^2 \frac{\partial^2 u}{\partial x^2} \tag{1.1}$$

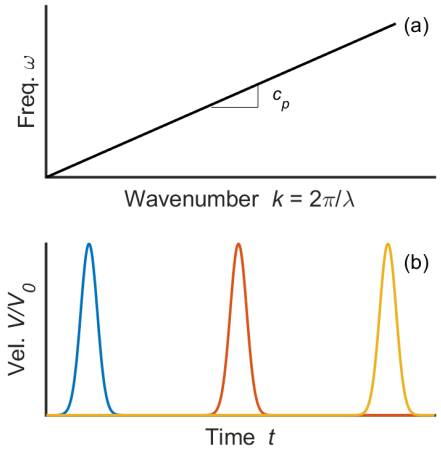

Figure 1.1: (a) Dispersion relation $\omega = \omega(k)$ for a non-dispersive wave with constant c_p. (b) Propagation of a forward traveling broadband pulse in a non-dispersive medium, displayed by plotting velocity V vs. time at three locations. The blue, red, and yellow curves correspond to the pulse at positions x_1, x_2, and x_3 such that $x_1 < x_2 < x_3$. All amplitudes are normalized by the maximum velocity V_0 at x_1.

A solution to this equation is given by Eq. 1.2 representing a forward traveling harmonic wave with complex amplitude A. We have assumed that c_p is a constant, such that all harmonic waves will travel at the same speed irrespective of wavenumber. Now recognize that a waveform of arbitrary shape, such as a broadband pulse, is simply the sum of infinite

harmonic waves of different amplitudes $A = A(\omega)$ found via Fourier decomposition [32]. Therefore, all Fourier components of an arbitrary waveform will travel together with velocity c_p, resulting in a non-dispersive wave that does not change shape as it propagates. This is demonstrated by propagation of a broadband pulse in Fig. 1.1(b). In this scenario, the only tunable parameter available is the frequency-independent sound speed, and it is not possible to alter the waveform shape using material properties.

$$u = Ae^{i(kx-\omega t)} = Ae^{ik(x-c_p t)} \tag{1.2}$$

On the other hand, the central element of a dispersive wave is a non-constant sound speed that depends on wavenumber and the dispersion relation is no longer a straight line. In this case, certain wavenumbers travel at different speeds such that a broadband waveform changes shape as it propagates, opening the prospect of waveform manipulation. Before demonstrating an example of a dispersive wave, consider how a wavenumber-dependent phase velocity can be achieved in physical systems. A one-dimensional longitudinal plane wave in an elastic material has a phase velocity $c_p = (E/\rho)^{1/2}$, where E is the elastic modulus and ρ is the mass density [32]. Moduli in some engineering materials can change with frequency, but in elastic materials this dependency is typically very weak and usually is well approximated as constant. Viscoelastic materials have frequency-dependent dynamic moduli, representing a transition from viscous to elastic behavior [33], but this a dissipative phenomenon and results in the conversion of kinetic energy to heat, which may not be desirable depending on the application. When restricted to intrinsic material properties, the design space is limited, and tailoring of acoustic waves in elastic materials is constrained.

One alternative to using intrinsic material properties for dispersion is to introduce material structure. A simple example of structure-induced dispersion involves longitudinal waves traveling along a one-dimensional monoatomic lattice of point masses M, connected by springs of linear stiffness K, and equilibrium spacing a as shown in Fig. 1.2(a). In this system, the dispersion relation is described by Eq. 1.3 and plotted in Fig. 1.2(b), where

there are three important regimes. In the long wavelength regime, when $ka \ll \pi$, we find a mostly straight line, indicating propagation is approximately non-dispersive. In the short wavelength regime, when ka approaches π, the dispersion relation begins to flatten, meaning shorter wavelengths will have slower phase velocities, up till $ka = \pi$. This point is called the cutoff frequency $\omega_c = 2\sqrt{K/M}$ because frequencies above it are not allowed to propagate and instead decay exponentially in space. These decaying waves, termed 'evanescent', are explained by inspecting Eq. 1.3 and recognizing that k becomes imaginary for $\omega > \omega_c$, which produces an exponential decay when inserted into the wave equation.

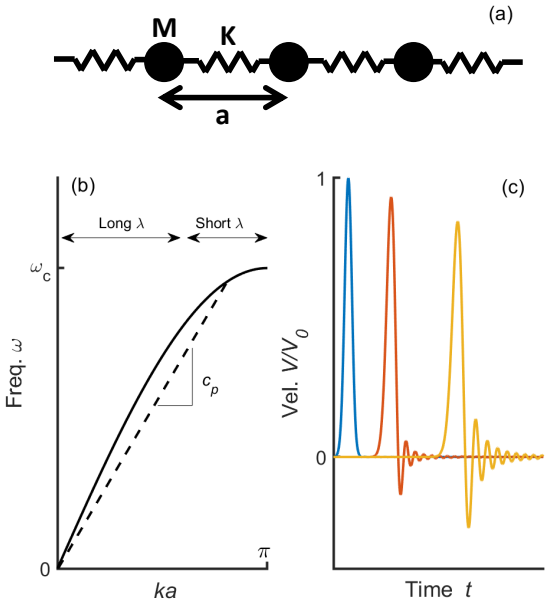

Figure 1.2: (a) Schematic of a one-dimensional monoatomic lattice of masses M connected by springs K with equilibrium spacing a. (b) Dispersion relation of the monoatomic lattice with wavenumber normalized by spacing a and displaying approximate long- and short-wavelength regimes, phase velocity c_p at an arbitrary point, and cutoff frequency ω_c. (c) Propagation of a forward traveling broadband pulse in a monoatomic lattice. The blue, red, and yellow curves correspond to the pulse at x_1, x_2, and x_3 such that $x_1 < x_2 < x_3$. All amplitudes are normalized by the maximum velocity V_0 at x_1.

$$\omega = 2\sqrt{\frac{K}{M}}\sin(\frac{ka}{2}) \tag{1.3}$$

An example of propagation in the short wavelength regime, but below the cutoff frequency, is shown in Fig.1.2(c), where a broadband pulse of many different wavenumbers stretches out according to its spectral content, with shorter wavelengths traveling slower than long wavelengths. The stark difference between Figs. 1.1(b) and 1.2(c) demonstrate that by altering the material structure, in this case by introducing discrete masses in a lattice instead of continuous material, waveform manipulation is possible.

1.3 Phononic Crystals and Metamaterials

Recently, significant advancements have been made in tailoring effective properties of materials called phononic crystals and metamaterials [34–36] which use structures with dimensions near or below the acoustic wavelengths to achieve unusual or uncommon behavior, such as bandgaps [37, 38], locally tunable properties [39], negative modulus [40–42], negative effective mass density [42, 43], and negative refractive index [44, 45]. The properties are thought of as effective because the collective, rather than individual, behavior of these structures is considered which simplifies the analysis by treating the repeating structures as a continuum [36, 46–51]. Although the intrinsic material properties remain the same, the effective material properties and behavior can be altered at will by designing the structure, thus providing the opportunity to break from the constraints of intrinsic properties and tailor behavior such as dispersion.

With phononic crystals, the key theme influencing dispersion is a periodic structure, hence the term "crystal" included in the name [34–36, 48]. The previously described monoatomic lattice is a simple theoretical example of a phononic crystal, with the structure, consisting of the spacing 'a' between discrete masses, having significant influence over the dispersion. A physical example of a phononic crystal is a compressed chain of steel spheres in contact shown in Fig. 1.3(a), where elastic deformation is localized near the contacts between spheres,

acting as linear springs at small displacements, and the spheres mostly move like rigid bodies, analogous to the monoatomic lattice [52]. Other physical examples of phononic crystals include alternating cells with different intrinsic material properties, such as steel pillars surrounded by air [53] or tungsten carbide spheres surrounded by water [54] for two- and three-dimensional systems, respectively, shown in Fig. 1.3(b,c). When a unit cell contains alternating regions of two materials, the dispersion relations are similar to that of a diatomic lattice, where the unit cell contains two different masses M_1 and M_2 connected in series by two different spring constants K_1 and K_2. The dispersion relation is different from a monoatomic lattice but is not relevant to this thesis and will not be discussed further.

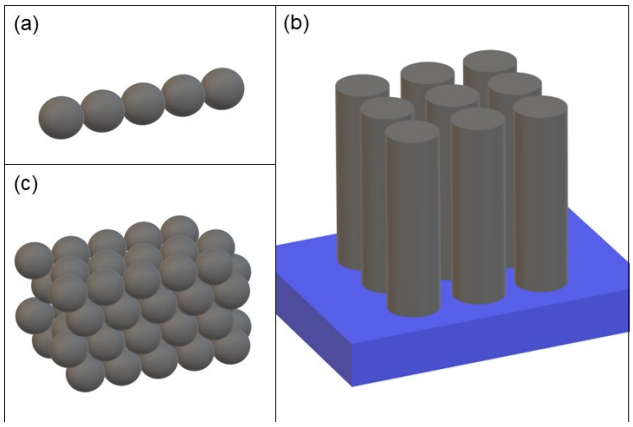

Figure 1.3: Schematics of physical phononic crystals. (a) One-dimensional phononic crystal made of steel spheres in contact, similar to Ref. [52]. (b) Two-dimensional phononic crystal made of pillars surrounded by air and mounted on a substrate (shown in blue), similar to Ref. [53]. In additional to behaving as a phononic crystal for waves traveling through air, in which the pillars are approximately rigid, it can also behave as a metamaterial for waves traveling through the substrate, in which the pillars' resonant bending modes are excited, as in Ref. [55]. (c) Three-dimensional phononic crystal made of tungsten carbide spheres surrounded by water, ordered in a hexagonally-close-pack arrangement, similar to Ref. [54].

Metamaterials, unlike phononic crystals, do not fundamentally rely on periodicity to ma-

nipulate dispersion, though in practice, many examples retain periodicity to ease analysis, simplify fabrication, or to combine the effects of both classes of materials. The key theme influencing dispersion in metamaterials is the inclusion of resonators that interact only with the local material deformation, termed 'locally resonant elements' [34, 48, 56–58].

A simple example that builds off the monoatomic lattice is to put a smaller sphere inside a hollow sphere, which makes up the chain, as shown in Fig. 1.4(a). Here the smaller spheres of mass M_2 are attached by springs of linear stiffness K_2 to a single hollow sphere and only interact with the local movement of the chain, thus acting as a locally resonant element. The dispersion relation of this metamaterial, shown in Eq. 1.4 [43] and Fig. 1.4(b), exhibits the splitting of the standard monoatomic lattice's dispersion relation into two branches, a result of the resonance of the internal mass. In the lower branch, the phase velocity slows as it approaches the local resonance frequency $w_0 = \sqrt{K_2/M_2}$ and does not cross it, ending at the lower cutoff frequency $\omega_{c,l}$. This trait is called an avoided crossing in the context of dispersion relations [59]. The upper branch begins at an onset frequency ω_{ons} above the local resonance, thus creating a frequency 'bandgap' in which waves decay exponentially in space and are not allowed to propagate. The upper branch ends at the upper cutoff frequency $\omega_{c,u}$ similar to the standard monoatomic chain acting strictly as a phononic crystal, which is a result of the periodic structure of the masses, i.e., the underlying factor controlling the $\omega_{c,u}$ is the wavelength reaching the spacing $\lambda = 2a$ $(ka = \pi)$ of the masses M_1. It should be noted the upper cutoff frequency differs quantitatively from the monoatomic lattice by the inclusion of the internal mass, but the basic concept of this being a phononic crystal effect remains the same. For the exact relationships between lattice parameters and onset and cutoff frequencies, see Refs. [43, 56].

$$M_1 M_2 \omega^4 - [(M_1 + M_2)K_2 + 2M_2 K_1(1 - cos(ka))]\omega^2 + 2K_1 K_2(1 - cos(ka)) = 0 \qquad (1.4)$$

An interesting trait of locally resonant metamaterials is that wavelengths considerably greater

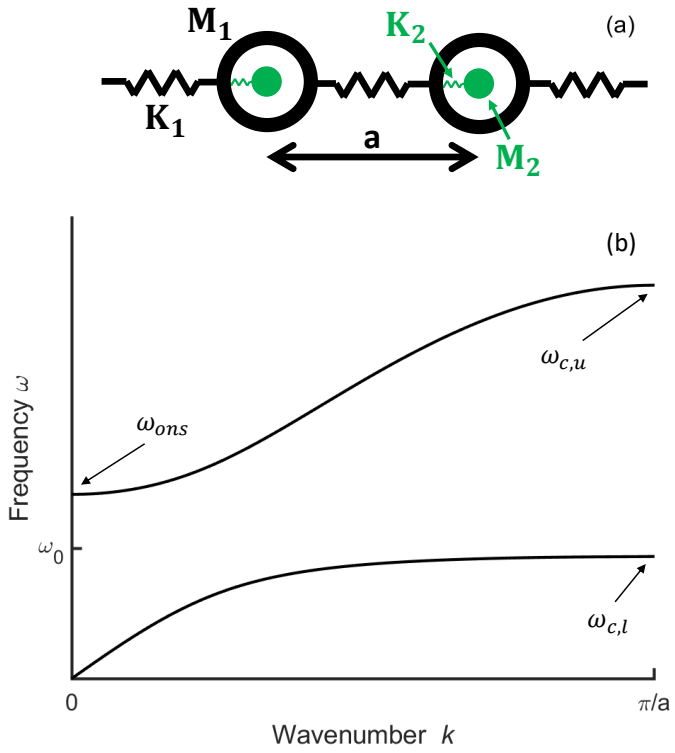

Figure 1.4: (a) Schematic of a metamaterial lattice, with the main chain composed of springs K_1 and masses M_1 with locally resonant inclusions composed of springs K_2 and masses M_2. (b) Dispersion relation of the metamterial lattice, with wavenumber k normalized by lattice spacing a and frequency ω normalized by the inclusions' resonant frequency $\omega_0 = \sqrt{K_2/M_2}$. The lower cutoff, onset, and upper cutoff frequencies are labeled as $\omega_{c,l}$, ω_{ons}, and $\omega_{c,u}$ respectively. For the plot shown, $M_2/M_1 = 1$ and $K_2/K_1 = 0.5$

than the lattice spacing can be manipulated simply by tuning the local resonance, thus freeing the phononic crystal constraint of needing wavelengths to approach the structure's periodic spacing in order to induce dispersion. In fact, replacing the discrete main chain of masses M_1 with continuous material such as a bar would still yield a metamaterial with dispersion induced by the attached local resonators. Various schemes of material structure have been used to fabricate metamaterials of different scale. Liu et al. studied bulk waves traveling through

an epoxy matrix with embedded silicone-coated centimeter-sized metal spheres acting as resonant [41]. Interaction of surface waves with a metamaterial was studied by Achaoui et al., where the structure consisted of microscale pillars, which have various resonant bending modes, attached to a substrate [55]. Whether the root of dispersion being periodicity, as with phononic crystals, or local resonance, as with metamaterials, manipulation of acoustic waves using material structure has proven to be a compelling strategy as evidenced by the significant research over the last several decades [36].

1.4 Mechanical Waves and Nonlinearity

Thus far, a linear relationship between stress and strain has been assumed, such that the behavior does not depend on wave amplitude. Removing this restriction allows for additional parameters to take advantage of. A systems dynamic response can change drastically when nonlinear elasticity is introduced, resulting in qualitatively different waveforms and further control over wave propagation. As a general concept across different disciplines, nonlinearity has enabled some of the most meaningful advancements in history. For instance, the electronic transistors and diodes required for modern day computing are nonlinear devices. In the context of mechanical waves, nonlinear systems have been applied to areas such as ultrasonic imaging [60], vibration control [61], and impact mitigation [62].

Continuing to build the upon the one-dimensional monoatomic lattice as an example, nonlinearity can be introduced by allowing springs with stiffness $K = K(u)$ that depends on the displacement. For the purposes of this work, a stiffness that increases with displacement, i.e., a 'stiffening nonlinearity', will be considered because this is the behavior of the physical systems examined in the following sections. The dynamics that result from this small change are highly complex, but in simple terms, one effect is that the sound speed and shape of the waveform can depend on wave amplitude. The nonlinear effect on sound speed can be understood as the system becoming stiffer with increasing amplitude. Waveforms, by definition, have displacements that vary in space, which when coupled with an amplitude dependent

sound speed, can fundamentally alter their shape as they propagate. For example, the peak of a compression pulse traveling in a medium with a stiffening nonlinearity will travel faster than the rest of the waveform because of the greater stiffness at high amplitudes, resulting in the pulse becoming steeper at the leading edge [63]. The opposite is true in the case of a softening nonlinearity, such that the trailing edge of the pulse becomes steeper [64].

An interesting phenomenon can occur when nonlinearity interacts with dispersion of broadband pulses, wherein the pulse steepening is balanced out by dispersion to create a stable waveform that does not change shape but travels at a speed that increases with excitation amplitude [65, 66]. Such a wave is termed a soliton and has been the topic of significant research in acoustic metamterials and phononic crystals over the past 30 years [52,56,67–71]. If the linear springs of the monoatomic lattice are replaced with nonlinearly stiffening springs, soliton formation can occur, as shown in Fig. 1.5, and a similar concept of the interplay between nonlinearity and dispersion is applicable in localized, temporally-periodic waves called breathers [69, 72].

Even when excitation amplitude is small, such that the nonlinear springs can be approximated as linear and nonlinear dynamics are neglected, tuning of the sound speed can be achieved by statically compressing the material through which waves travel. In this case, the acoustic waves can be thought of as small perturbations on the force-displacement curve about an equilibrium displacement induced by static compression, such that a linear spring constant can be approximated by the slope of the tangent line, as shown in Fig. 1.6. Static compression changes the equilibrium displacement, thus altering the linearized spring constant and sound speed in a monoatamic lattice as $c_p = a\sqrt{K_{lin}(u_{eq})/M}$, where $K_{lin}(u_{eq})$ is the linearized spring stiffness at the equilibrium compressive displacement u_{eq} and a is the lattice spacing. Acoustic waves can be approximated as linear in these systems if the dynamic displacement of the spring is much smaller than the equilibrium displacement. Regardless if wave amplitude meets the criteria of linear approximation or not, nonlinearity of the system has great potential to be exploited, either statically or dynamically, as an

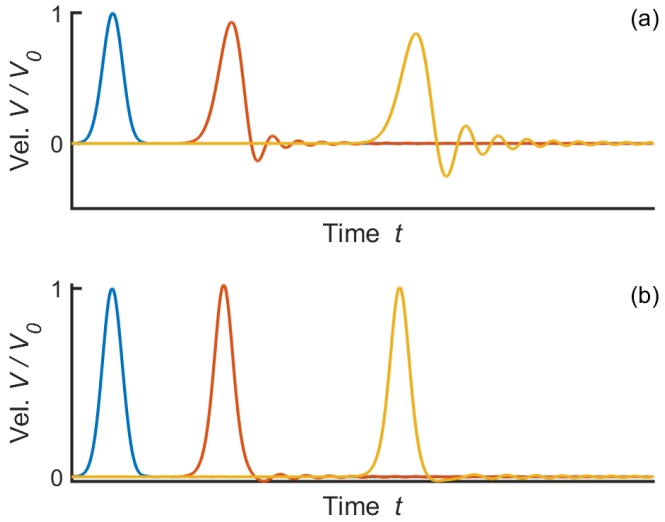

Figure 1.5: (a) Propagation of a forward traveling broadband pulse in a monoatomic lattice with linear springs. (b) The same input pulse as (a) but traveling through a monoatomic lattice with nonlinearly stiffening springs $K(u) \sim u^{1/2}$. In both panels the blue, red, and yellow curves correspond to the pulse at x_1, x_2, and x_3 such that $x_1 < x_2 < x_3$ and all velocities are normalized by the maximum velocity V_0 at x_1.

important parameter for wave manipulation.

1.5 Geometric Nonlinearity

Now that the utility of nonlinearity has been established, consider the physical realization of such behavior. The root of nonlinear acoustic waves in solids is amplitude dependent moduli, i.e., a nonlinear relationship between stress and strain, or more macroscopically, between force and displacement. Materials can have intrinsic nonlinear moduli stemming from multiple sources, such as alignment of polymer molecules in elastomers [73, 74] or the transition from elastic to plastic deformation in ductile solids, but tailoring of intrinsic properties is still limited to what materials can be synthesized. However, just as leveraging

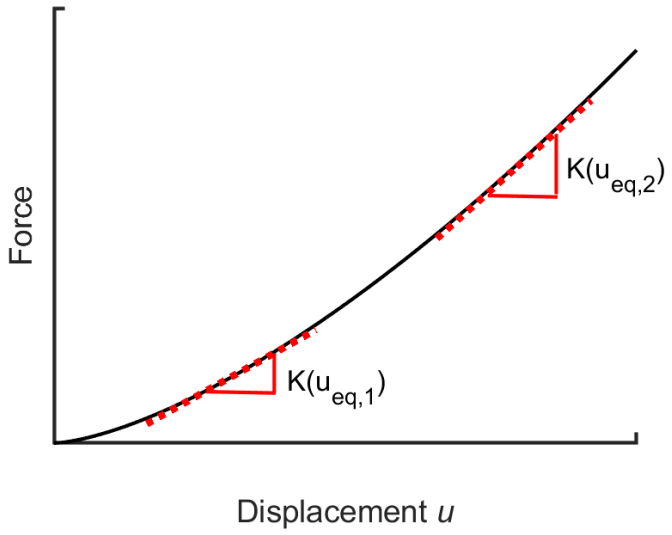

Figure 1.6: Force vs displacement of a nonlinearly stiffening spring defined by $F = u^{3/2}$. Dashed red lines indicate the slopes, i.e., the linearized stiffness, at two equilibrium displacements $u_{eq,1}$ and $u_{eq,2}$.

designed structure holds promise to achieve a high degree of dispersion tailoring, controlling nonlinearity from an effective material property standpoint is an attractive strategy. This approach is called geometric nonlinearity to distinguish it from intrinsic material nonlinearity.

One structure that can produce geometric nonlinearity is a simple case from the broader field of contact mechanics, in which two elastic bodies with curved surfaces are in contact with each other, e.g., two elastic spheres being compressed together as shown in Fig 1.7. This classic problem was solved by Heinrich Hertz by assuming a parabolic stress profile between the bodies [75], and if two spheres are considered, the solution relating the force compressing the spheres F and the displacement relative to the undeformed positions δ is given by Eq. 1.5, in which the effective elastic modulus $E_{eff} = [(1-{\nu_1}^2)/E_1 + (1-{\nu_2}^2)/E_2]^{-1}$, ν is Poisson's ratio, the effective contact radius $R_{eff} = [1/R_1 + 1/R_2]^{-1}$ (equal to $R/2$ for two spheres or R for a sphere and a planar surface), and subscripts correspond to each body.

The key element of this solution is that there is a 3/2 power relation between force and displacement. Stiffness of the contact is defined as the derivative $K = dF/d\delta$, which when applied in this case, produces a nonlinearly increasing stiffness proportional to $K(\delta) \sim \delta^{1/2}$ or equivalently $K(F) \sim F^{1/3}$.

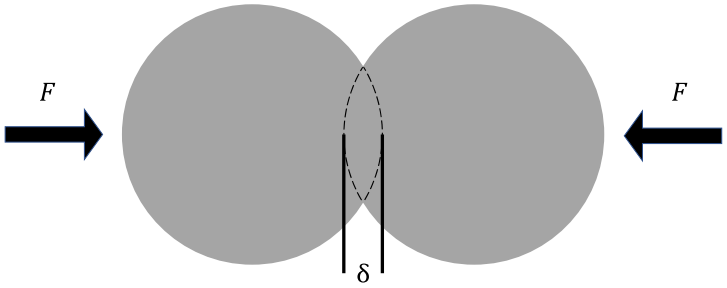

Figure 1.7: Two elastic spheres being compressed by force F with relative displacement δ, also known as static overlap or interpenetration depth.

$$F = \frac{4}{3} E_{eff} {R_{eff}}^{1/2} \delta^{3/2} \tag{1.5}$$

When many individual elastic bodies are in contact, they collectively are termed 'granular media', alluding to the discrete nature of these systems. Granular media is a wide field that includes disordered and irregular particles, but to simplify analysis for wave propagation, systems of macroscale uniform particles on the order of millimeters to centimeters are often studied in one- or two-dimensional ordered arrays. This sub-field, called macroscale granular crystals, has received significant attention since the 1980s [52, 56, 69, 76] due to supporting highly complex nonlinear dynamics such as solitons and breathers. Consider the previously

mentioned one-dimensional chain of spheres in Fig 1.3(a). This system has all the elements of a nonlinear phononic crystal: Hertzian contact mechanics providing nonlinear springs (assuming sufficient excitation amplitude), spheres acting as masses, and the uniform size and ordered arrangement enforcing periodicity of the system. Higher dimensional systems, such as ordered two- and three-dimensional packings of uniform spheres, retain these key elements as well. Granular media can also act as a metamaterial with local resonance when the grains are in contact with other elastic bodies, such as a single layer of spheres compressed against an elastic substrate by an attractive force [77]. Each sphere acts as a mass attached to the surface with a spring, therefore fulfilling the criteria of local resonance which can interact with surface waves traveling through the substrate similar to the pillars in Fig. 1.3(b), although the nature of the contacts allows additional nonlinear tailoring. Whether approaching these systems as phononic crystals, metamaterials, nonlinear mediums, or a combination of all three, the structure of granular media has the potential to manipulate waves by a variety of approaches.

Numerous creative applications of macroscale granular crystals have been demonstrated as the field has matured in recent years. Acoustic lenses have direct application for ultrasonic imaging and therapeutic procedures, and by taking advantage of the Hertzian geometric nonlinearity in an array of granular crystal chains, Spadoni et al. created a lens with a tunable focus by controlling the velocity of pulses within each chain individually via variable precompression, such that the spatial phase delay causes constructive interference at a focal point within the medium in contact with the lens [78].

Rectifiers, which allow energy transmission in only one direction, are one of the most essential electronic components used today, and typically composed of semiconductor junctions. Extending such control of energy into the acoustic and mechanical realms could have applications in energy harvesting and vibration control. An acoustic rectifier scheme using granular crystals was demonstrated by Boechler et al. that relied on inserting a small mass defect into the chain and driving the system above the cutoff frequency. Depending on the

defect location and driving amplitude, nonlinearly generated modes appear at frequencies below the cutoff frequency and can propagate across the rectifier [79].

Impact mitigation and vibration control is another area where the unique dynamics of granular crystals hold great promise [56]. By utilizing a three-dimensional granular crystal network of branched chains, Leonard et al. made significant performance improvements compared to the continuous, homogenous materials typically used in these applications [62]. In addition to the branched network distributing the impact load in space, the combined dispersive and nonlinear dynamics introduced by the granular geometry distribute the impact load in time, providing additional performance for minimizing the peak load amplitude. Another work by Leonard et al. manipulated wave front shape and direction of energy propagation in a two-dimensional array of spheres with cylindrical intruders placed in the interstitial spaces between spheres. By choosing either steel or polymer spheres and intruders, dramatic differences in wave fronts were seen [80].

While significant insight has been gained using macroscale granular crystals with particles diameters on the order of centimeters, and creative applications using these systems have been proposed, translation of these advancements to widespread use from an engineering standpoint has not be achieved. A major issue is that engineering applications usually have space and weight constraints. When granular crystals are composed of collections of particles with centimeter-scale diameters, often made of steel, one can imagine the how the potential applications become rather limited.

1.6 Microscale Granular Crystals

Returning to the idea of thinking of a material as having effective properties influenced by structure, consider taking these macroscale granular crystals, with their demonstrated potential for mechanical wave and vibration manipulation, and shrink them down to the microscale. Besides the obvious savings in weight and space, reducing the characteristic particle size also allows for access to higher frequencies and smaller wavelengths with potential

applications in acoustic microscopy, surface acoustic wave (SAW) and bulk acoustic wave (BAW) devices commonly used as electronic filters, and at extremely small scales, potentially even heat management via phonon manipulation [81].

While there are important advantages of reducing the particle size, there may also be drastic differences in behavior because different physics dominate microscale systems and can't be neglected. In the context of microscale granular crystals, the most important change to consider is adhesion, which is an attractive surface force primarily caused by Van der Waals intermolecular forces. Due to this attractive force acting on surfaces, a simple scaling analysis reveals how important adhesion is for microscale particles. For spherical particles, surface area A scales with particle radius r as $A \sim r^2$, while gravitational forces, proportional to particle mass, scale with volume as $V \sim r^3$. A rough approximation for relative magnitude of these forces is the surface area to volume ratio, which scales as r^{-1} and becomes very large for microparticles. This explains why a centimeter sized spheres do not cling to each other, but individual microparticles readily adhere and agglomerate into large clusters.

Incorporation of adhesive forces into the contact mechanics of microparticles has several different approaches, with the typically used models based off of the Hertzian elastic solution being the Derjaguin-Muller-Toporov (DMT) [82], Johnson-Kendall-Roberts (JKR) [83], and Maugis-Dugdale (MD) models [84]. The DMT model is applicable for small and hard spheres, where the attractive forces act only outside the contact area while JKR is best suited to large and compliant spheres, where attractive forces act within the contact area. The MD model represents a transition between DMT and JKR based off the Tabor parameter [85]. Since the DMT model builds upon the Hertzian elastic contact, the force-displacement relation of $F \sim \delta^{3/2}$ holds, but due to adhesion, there is a constant attractive force of $F_{DMT} = 2\pi w R_{eff}$, where w is the work of adhesion between the two materials in contact and R_{eff} is the effective contact radius defined in the same manner as for Eq. 1.5. To demonstrate the importance of adhesion with calculations from Chapter 3, a 1 μm diameter polystyrene sphere located on an alumina surface has a predicted adhesive force of $F_{DMT} = 0.36$ μN, while the gravitational

force on this sphere is seven orders of magnitude smaller at $F_{grav} = 5.5\ f\text{N}$.

The more obvious effect of these adhesive forces is that a constant precompressive load can drastically affect the dynamics of systems with Hertzian nonlinearities, as was shown in the previous section. The adhesive forces stiffen the system relative to the uncompressed macroscale analogues by inducing an equilibrium interparticle displacement, therefore creating a higher excitation amplitude threshold beyond which nonlinear dynamics appear. In the context of adhesion between particles and a substrate, the adhesion-induced deformation of the contact allows the spheres act as mass-spring resonators attached to the surface, effectively turning it into a metamaterial for surface waves [77]. These can be considered linear oscillators when excitation amplitude is small compared to the equilibrium deformation, or nonlinear oscillators when excitation amplitude is of similar magnitude or greater.

Less obvious effects of this adhesive precompression include supporting interparticle shear forces, opening the door for rotational dynamics, which have been studied in detail in macroscale granular crystals only within the past decade [86]. Adhesive forces can also be large enough such that plastic deformation occurs, even in typically brittle materials such as silica [87, 88], which causes deviations from the Hertzian power-law nonlinearity. Another important factor when working at the microscale is the spatial organization and load distribution of particles, which is known to be extremely important for determining wave propagation characteristics [62, 89–92]. The dominance of adhesion over gravitational forces is both a challenge for fabricating uniform samples, since particles tend to stick to the first surface they contact, but also an opportunity: i) to form stable structures that would otherwise require supports, or ii) to take advantage of low-cost fabrication techniques. Self-assembly is a bottom-up fabrication method centered around controlling environmental conditions such that particles suspended in liquid will naturally organize into desired arrays [93]. This approach is orders of magnitude less expensive than standard cleanroom top-down fabrication methods, in addition to being better suited for scalability to fabricate large amounts of material. Among various factors such as convective flow and evaporation,

surface forces such as adhesion are essential to self-assembly. All research performed for this thesis was conducted with self-assembled structures, with the various techniques that were used detailed within each chapter. Considering that such fundamental differences exist between micro- and macroscale granular crystals, exploration of these systems at small scales has increased in the past decade yet many questions remain open, particularly regarding nonlinear dynamics.

Various research has been conducted on three-dimensional packings of microparticles but has largely been limited to low excitation amplitude in the linear regime where probing the nonlinear nature of the contacts was not the focus. The dispersion relation of a microscale phononic crystal made of nanospheres was experimentally determined by Cheng et al., however the sphere assembly was infiltrated with fluids that supported acoustic waves, such that interparticle contacts did not dominate the dynamic behavior [94]. Mattareli et al. studied nanosphere assemblies without infiltrating fluids and modified the interparticle stiffness by changing the contact geometry through thermal annealing [95]. Eigen vibrations of a disordered film of silica nanoparticles was investigated to extract effective interparticle stiffnesses by Ayouch et al., who were able to change the sound speed by converting interparticle surface forces from Van der Waals bonds to hydrogen and covalent bonds [96]. In a related study by Lisiecki et at., an ordered assembly of nanoparticles coated with dodecanoic acid chains acting as interparticle springs were found to have a significant temperature dependent stiffness, reversibly changing by a factor of over 3.5 when temperature was cooled from $435K$ to $110K$ [97]. The effect of excitation amplitude on the dynamic response of microsphere assemblies in the presence of liquid has been studied by Buttinoni et. al. [98] and Brum et. al. [99], however, the presence of liquid, and the introduction of large viscous forces, significantly alters acoustic wave propagation compared to the dry state. The liquid environment also modifies attractive interparticle forces through the reduction of van der Waals forces and formation of a repulsive electrostatic double layer [100].

Studies with disordered assemblies of spherical particles ranging from tens of microns to

several millimeters in diameter have been investigated by changing static and/or dynamic loading amplitudes and found results consistent with the Hertzian contact model [101–105], although deviations have been observed where sound speed is more sensitive to static loads, typically at low confining pressures [101, 103, 106]. Similar dependence of sound speed on static load was also found using an ordered two dimensional assembly of compressed spheres [107]. However, adhesive forces are far less dominant in this size range compared to spheres on the order of a few microns or smaller, and the behavior cannot be assumed to be the same. Acoustic waves traveling through geological materials that are partially or completely composed of microscale particles have been investigated in the context of nonlinearity, but these are excluded from further discussion due to the complexity of analysis for particles with nonuniform size, shape, and composition [108–112].

Quasi-static force-displacement experiments on single micro- and nanospheres have also shed light on the behavior of contact mechanics at this scale [87, 113–117]. For example, measurements using a micromanipulator mounted inside a scanning electron microscope have been performed by Paul et al. and Romeis et al. [87, 113], where single silica nanospheres were compressed by a flat diamond punch while simultaneously measuring force and displacement. The contact mechanics were found to be well approximated as Hertzian up till the point of plastic deformation and fracture, however, the dynamic response was not investigated. A dynamic approach for studying the contact mechanics of single gold micro- and nanoparticles adhered to a flat substrate was used by Guillet et al. [118], who used a noncontact photoacoustic measurement scheme that simultaneously obtained the breathing and axial contact modes. The breathing mode can be directly related to the particle diameter, while the axial contact mode is related to the stiffness of the contact. The ratio of these modes can be predicted by assuming a contact mechanics model, which was in approximate agreement with Hertzian. However, the variable being changed was the particle diameter, and the nonlinear force-displacement relationship was not investigated.

It's clear from the literature on microscale granular crystals and disordered granular me-

dia that the stiffness derived from interparticle contacts is a key element for acoustic wave propagation and can be used to tune the sound speed. A few studies involving single particles, whether static [87, 113–116] or dynamic [118], suggest that the force-displacement relationship can be reasonably approximated as Hertzian in certain cases, however, it remains undetermined whether the collective acoustic behavior of microscale granular crystals are capable of supporting nonlinear dynamics analogous to their macroscale counterparts. Investigating the nonlinear behavior and how it relates to vibrations and acoustic wave propagation is essential to translating the promise of granular crystals from macro- to microscale and the broadening of practical applications that may result.

1.7 Organization of This Thesis

This thesis presents research conducted in the pursuit of understanding the open question of what nonlinear dynamics are supported by three-dimensional microscale granular crystals. Broadly, this starts out by probing the fundamental elements of such dynamics in two-dimensional granular crystals adhered to surfaces, then builds up to high-amplitude excitation of three-dimensional systems. The organization is as follows:

- Chapter 2: "Complex contact-based dynamics of microsphere monolayers revealed by resonant attenuation of surface acoustic waves". Collective dynamics of a two-dimensional monolayer of microspheres were found to couple with surface acoustic waves in an elastic substrate, inducing frequency-dependent attenuation due to three microsphere resonant modes. Two of these modes were composed of horizontal and rotational motion and highly dependent on interparticle contacts. Horizontal-rotational and interparticle modes are known to influence wave propgation in three-dimensional granular crystals. This extends a previous work of a similar system in which only one-dimensional particle motion and particle-substrate contacts were considered.

- Chapter 3: "Laser-induced spallation of microsphere monolayers". A monolayer of microspheres was excited with high amplitude bulk acoustic waves, such that the adhesion

to the substrate was overcome and particle ejection occurred, allowing for non-contact estimation of the pull-off force. By assuming an elastic contact mechanics model, the pull-off force was compared with measurements of the microsphere resonance via laser ultrasonics and visual estimation of the contact diameter via scanning electron microscope. The comparison varied widely, suggesting plastic deformation in the contact region.

- Chapter 4: "Longitudinal eigenvibration of few-layer granular crystals and the effect of nanoscale contact bridges". Standing wave vibrations of an ordered three-dimensional granular crystal were investigated at various thicknesses in the linear regime at low excitation amplitude. Variations in sample fabrication were shown to impact geometric alterations of the contact region, with drastic effects on the stiffness and longitudinal sound speed of the crystal.

- Chapter 5: "Acoustic wave propagation in disordered microscale granular media under compression". The nonlinear nature of interparticle contacts were directly probed in a disordered three-dimensional microsphere assembly by measuring the reversible change in sound speed under variable static and dynamic loading. The sound speed showed significant deviations from Hertzian behavior when testing on the as-fabricated sample, while after mechanical conditioning, the behavior was in approximate agreement. It is hypothesized that the as-fabricated sample contains particle networks with solid bridges of debris that alter the contact geometry, which then break under network reformation during the conditioning process.

- Chapter 6: "Strongly nonlinear acoustic wave propagation within ordered three-dimensional microscale granular crystals. The dependence of sound speed on acoustic wave amplitude in an ordered three-dimensional granular crystal was studied in preliminary experiments, which found behavior similar assemblies of macroscale spheres that span the linear, weakly nonlinear, and strongly nonlinear regime, where increasing amplitude causes the sound speed to asymptotically approach a power law relationship.

Chapter 2

COMPLEX CONTACT-BASED DYNAMICS OF MICROSPHERE MONOLAYERS REVEALED BY RESONANT ATTENUATION OF SURFACE ACOUSTIC WAVES [1]

Contact-based vibrations play an essential role in the dynamics of granular materials. Significant insights into vibrational granular dynamics have previously been obtained with reduced-dimensional systems containing macroscale particles. We study contact-based vibrations of a two-dimensional monolayer of micron-sized spheres on a solid substrate that forms a microscale granular crystal. Measurements of the resonant attenuation of laser-generated surface acoustic waves reveal three collective vibrational modes that involve displacements and rotations of the microspheres, as well as interparticle and particle-substrate interactions. To identify the modes, we tune the interparticle stiffness, which shifts the frequency of the horizontal-rotational resonances while leaving the vertical resonance unaffected. From the measured contact resonance frequencies we determine both particle-substrate and interparticle contact stiffnesses and find that the former is an order of magnitude larger than the latter. This study paves the way for investigating complex contact-based dynamics of microscale granular crystals and yields a new approach to studying micro- to nanoscale contact

[1] Included in this chapter contains material from Refs. [119, 120]. Copyright 2016 by the American Physical Society [119] and the American Institute of Physics [120].

Reprinted with permission from [M. Hiraiwa, M. Abi Ghanem, S. Wallen, A. Khanolkar, A. Maznev, and N. Boechler, Complex Contact-Based Dynamics of Microsphere Monolayers Revealed by Resonant Attenuation of Surface Acoustic Waves," Physical Review Letters, vol. 116, no. 19, p. 198001, 2016.] *https* : *//doi.org/*10.1103/*PhysRevLett*.116.198001 Copyright (2016) by the American Physical Society.

Reprinted from [A. Geslain, S. Raetz, M. Hiraiwa, M. Abi Ghanem, S. P. Wallen, A. Khanolkar, N. Boechler, J. Laurent, C. Prada, A. Duclos, P. Leclaire, and J.-P. Groby, Spatial Laplace transform for complex wavenumber recovery and its application to the analysis of attenuation in acoustic systems," *Journal of Applied Physics*, vol. 120, no. 13, p. 135107, 2016.], with the permission of AIP Publishing.

mechanics in multiparticle networks.

2.1 Introduction

Micro- and nanoscale particles in contact with other bodies experience strong adhesive forces that induce deformation near the point of contact [121]. The understanding of contact mechanics is critical to many fields, including areas such as surface science [121], contaminant removal [122], self-assembly [123], powder technology and processing [124, 125], and biomedicine [126]. In systems with adhered micro- and nanoscale particles, low frequency dynamic disturbances (compared to the intrinsic spheroidal modes of the spheres [127]) can induce contact-based vibrational modes in single- and multiparticle systems, where the particles move like rigid bodies and the local region of deformation around the contact acts as a spring [52].

Such contact-based vibrational modes form the foundation for the dynamics of particulate assemblies. The contactbased dynamics of granular media play a critical role in fields such as wave propagation in geological and other microstructured materials [52]. While there has been significant progress in the study of the contact-based dynamics of macroscale granular media [52, 128], the dynamics of micro- to nanoscale particle assemblies are less understood. This difference in scale is important from a fundamental perspective; in particular, adhesion forces negligible for macroscale particles become critical at micro- to nanoscales.

At the macroscale, studies of reduced dimensional systems, such as one- and two-dimensional granular arrays that are commonly referred to as "granular crystals," have yielded significant insights into the dynamics of granular materials [52, 128]. In contrast, studies of the contact-based dynamics of micro- to nanoscale particle assemblies have hitherto been restricted to three-dimensional, typically disordered, settings [52, 95, 96, 129].

Recently, a contact resonance of microspheres assembled into a two-dimensional monolayer adhered to a solid substrate was measured via its hybridization with surface acoustic waves (SAWs) traveling in the substrate [77]. The results agreed well with a simple model where

the particle motion was restricted to the vertical (out-of-plane) degree of freedom and the interaction between the particles was disregarded. However, models involving both rotations and interparticle interactions [130, 131] predicted more complex dynamics. For motion in the sagittal plane, a close-packed monolayer of spheres on a solid substrate is expected to yield three collective contactbased vibrational modes: one predominantly vertical, and two of mixed horizontal-rotational character, all of which should interact with SAWs [130]. It has remained a mystery as to why the previous experiment only showed the presence of a single contact resonance mode.

In this work, we reveal the presence of all three contact resonances predicted for the microsphere monolayer, by measuring the attenuation of SAWs using a scanned laser ultrasonic technique. We test the model by changing the interparticle contact stiffness via the deposition of a thin aluminum film on top of the spheres, which shifts the horizontal-rotational contact resonance frequencies upwards. We further confirm the nature of the modes using a complementary laser-ultrasonic technique that preferentially excites the vertical contact resonance. In addition to providing direct evidence of the rotational-vibrational dynamics of microgranular media, our work opens a new approach for the study of micro- to nanoscale particle contact mechanics by enabling measurements of both the interparticle and particle-substrate contact stiffness and offering insight into the role of shear contact rigidity.

2.2 Experimental Section

Our sample is a monolayer of $D = 2.0\mu$m diameter silica microspheres deposited on an aluminum-coated glass substrate, as shown in Figs. 2.1(a) and 2.1(b). The aluminum layer is 100 nm thick, and the glass is 1.5 mm thick. A wedge-shaped cell convective self-assembly technique is used to assemble the monolayer on the substrate [132]. To obtain a planar interface between substrate regions with and without the microsphere monolayer (hereafter referred to as the monolayer and blank regions, respectively), we use a microcontact-printing method, wherein a soft polydimethylsiloxane stamp is pressed into conformal contact with

the microsphere monolayer and then is removed, such that the spheres detach from the substrate in the stamped region (see Ref. [133] and Appendix A). A representative optical microscope image of the resulting interface is shown in Fig. 2.1(a).

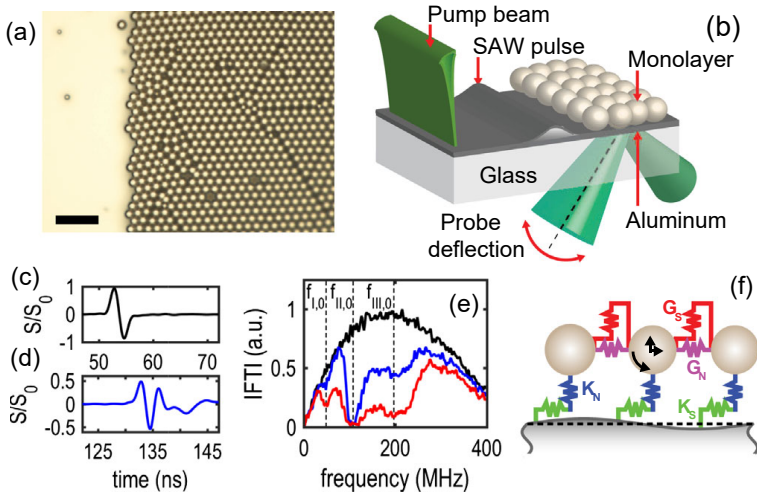

Figure 2.1: [Color online] Overview of the experiment. (a) Microscope image of the interface between monolayer and blank sample regions. The scale bar is 10 μm. (b) Schematic of the scanned laser ultrasonic experimental setup. Normalized signal measured in the (c) blank region and (d) 132 μm inside the monolayer region. (e) Normalized Fourier spectra of the signals in (c) and (d) using the same colors. The red spectrum is the spectrum of a signal measured 400 μm inside the monolayer region. Vertical dashed lines denote the identified contact resonance frequencies. (f) Schematic of the dynamical model.

To generate and measure SAW propagation in our sample, we utilize a scanning laser-ultrasonic technique, as shown in Fig. 2.1(b) (see Appendix A for details). We focus a subnanosecond laser pulse, which serves as a "pump," into a line on the aluminum surface of the blank region of the substrate. The absorbed laser light launches broadband SAW pulses that propagate as plane waves perpendicular to the line source. The acoustic response of the sample is measured via a knife-edge photodeflection technique [134]. A "probe" beam is incident through the substrate and focused to a small spot on the aluminum film. The

reflected probe light is focused onto a fast photodetector, after being partially blocked by a knife edge. Changes in the surface slope and refractive index caused by the SAWs deflect the probe beam, which translates to a change in intensity on the photodetector. To obtain spatial information, the sample is automatically scanned in the direction of the SAW propagation. Both the pump and probe are initially focused onto the blank region, then moved progressively closer to the interface, with the probe crossing into the monolayer region.

2.3 Results

Figures 2.1(c) and 2.1(d) show typical measured signals S, normalized to the maximum signal amplitude S_0 measured during the scan. Figure 1(c) corresponds to a probe position in the blank region, and Fig. 1(d) corresponds to a probe position 132μm inside the monolayer region. The distortion of the signal in Fig. 1(d) is a result of dispersion and dissipation induced by the monolayer.

The Fourier spectra of the normalized signals in Figs. 2.1(c) and 2.1(d) are shown in Fig. 2.1(e). The spectrum corresponding to the signal in the monolayer region shows a sharp dip at 108 MHz. We also observe two smaller dips surrounding this resonance, and denote the three dips with vertical lines drawn at $f_{I,0} = 49$ MHz, $f_{II,0} = 108$ MHz, $f_{III,0} = 197$ MHz. We also show a third spectrum, corresponding to a location 400 μm inside the monolayer region, which demonstrates the evolution of the attenuation zones.

To obtain position-dependent transmission spectra of SAWs traversing the interface, we normalize the Fourier spectra at each position by the average Fourier spectra of the incident SAW (averaged over all positions in the blank region). Figure 2.2(a) shows the measured transmission spectra as a function of distance from the interface. Three distinct attenuation maxima are evident, corresponding to the identified dips in Fig. 2.1(e). We interpret themeasured attenuation maxima as being caused by the interaction of SAWs with contact resonances of the microsphere monolayer, as described by the recently developed model of Ref. [130]. In this model, the microspheres are considered as rigid bodies, and the sphere-substrate

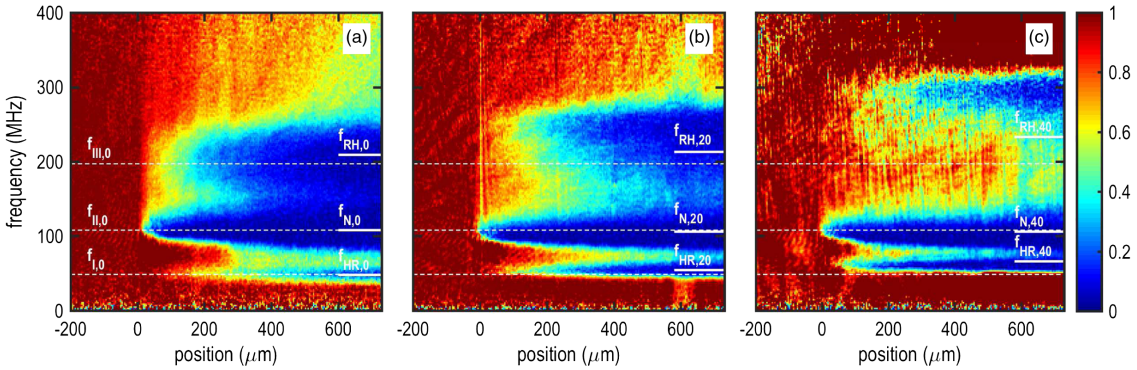

Figure 2.2: [Color online] (a-c) Transmission spectra for SAWs propagating across the interface between blank and monolayer regions. The color bar denotes the magnitude of the transmission coefficient. Horizontal dashed lines denote the identified contact resonance frequencies for the uncoated monolayer. Short horizontal lines on the right of the panels are the fitted contact resonance frequencies. Position denotes the distance from the interface. (a) Uncoated microsphere monolayer. (b) 20 nm of aluminum coating. (c) 40 nm of aluminum coating.

and sphere-sphere contacts are represented as normal and shear springs, as is shown in Fig. 2.1(f). This model predicts three collective vibrational modes of the monolayer involving vertical, horizontal, and rotational motion of spheres in the sagittal plane.

At long wavelengths (compared to the particle spacing), one of the modes is purely vertical, with a frequency given by:

$$f_N = \frac{1}{2\pi}\left[\frac{K_N}{m}\right]^{1/2} \tag{2.1}$$

while two others are of mixed horizontal-rotational character, with frequencies given by:

$$f_{RH} = \frac{1}{2\pi}\left[\left(\frac{K_S}{4m}\right)\left(20\gamma + 7 + \sqrt{400\gamma^2 + 120\gamma + 49}\right)\right]^{1/2}$$
$$f_{HR} = \frac{1}{2\pi}\left[\left(\frac{K_S}{4m}\right)\left(20\gamma + 7 - \sqrt{400\gamma^2 + 120\gamma + 49}\right)\right]^{1/2}, \tag{2.2}$$

where $m = \rho\pi D^3/6$ is the microsphere mass, K_N is the particle-substrate normal stiffness, K_S is the particle-substrate shear stiffness, G_S is the interparticle shear stiffness, and $\gamma = G_S/K_S$. The interparticle normal contact stiffness G_N does not affect these resonances at long wavelengths. The frequency f_{RH} corresponds to the predominantly rotational mode and is always higher than the frequency of the predominantly horizontal mode f_{HR}. If the monolayer is placed on an elastic substrate, all three modes are predicted to interact with SAWs [130]. In the absence of dissipation, this interaction results in the hybridization and avoided crossing of the Rayleigh SAW with the contact resonances. In the presence of dissipation, avoided crossing may or may not take place, but one would invariably expect a peak in attenuation at the contact resonance frequency [135]. As can be seen from Eq. 2.1 and Eq. 2.2, f_N is determined solely by the particle-substrate contact, whereas f_{RH} and f_{HR} are affected by both contacts. Hence, if we increase the interparticle contact stiffness, only f_{RH} and f_{HR} are expected to increase.

To test the model and verify the nature of the observed contact resonances, we coat the microsphere monolayer with a thin aluminum layer using electron beam evaporation, which stiffens the interparticle contact without affecting the particle-substrate contact (see Appendix A for SEM images of the aluminum deposition). Figures 2.2(b) and 2.2(c) show transmission spectra for the samples coated with aluminum. The highest and the lowest attenuation maxima shift upwards upon the deposition of the aluminum, while the middle maximum remains nearly unaffected. The relatively small downshift of the middle resonance, which is approximately consistent with the predicted frequency downshift of $\sim 4\%$ due to extra mass loading, confirms our assignment of the middle resonance to f_N. In all cases, the middle zone has the largest attenuation, indicating stronger coupling of this resonance to

the propagating SAWs.

For further confirmation of the assignment of the resonances, we conduct a separate experiment on the sample coated with 40 nm of aluminum, wherein a pump beam entering through the substrate is focused to a large diameter (240 μm at $1/e^2$ intensity level) spot. In this configuration, thermal expansion of the aluminum layer excites the vertical contact resonance of the spheres directly, while horizontal-rotational resonances are not excited because of symmetry constraints. The displacement of the spheres is measured with a grating interferometer [136], which is also only sensitive to vertical motion. The measured signal shown in Fig. 2.3(b) contains oscillations at a frequency of $\sim$ 100 MHz, as can be seen from the Fourier spectrum in Fig. 2.3(c), thus confirming the middle resonance in Figs. 2.2(a)–2.2(c) as the vertical mode.

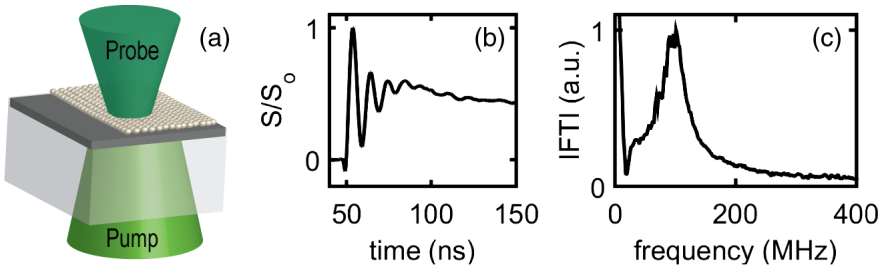

Figure 2.3: (a) Schematic of the experiment with large spot excitation and grating interferometer detection. (b) Normalized signal measured with the interferometer. (c) Fourier spectrum of the signal in (b).

We compare the frequencies of the observed attenuation maxima shown in Fig. 2.2 with those predicted by Eq. 2.1 and Eq. 2.2. While the equations have three unknown parameters (K_N, K_S, and G_S), we relate K_S to K_N via the Hertz-Mindlin contact model [137], which leaves two independent parameters. In the Hertz-Mindlin contact model, assuming a no-slip condition at the contact, the normal stiffness for a given contact is related to the shear stiffness, such that $K_S/K_N = 4G^*/E^*$, where $E^* = [(1-\nu_1^2)/E_1 + (1-\nu_2^2)/E_2]^{-1}$ is the

effective Young's modulus of the contact, and $G^* = [(2-\nu_1)/G_1 + (2-\nu_2)/G_2]^{-1}$ is the effective shear modulus, where E_1 and G_1 are the moduli for the silica microspheres, and E_2 and G_2 are the moduli for the aluminum substrate, as detailed in Appendix A. Using Eq. 2.1 and the measured value of $f_{II,0} = f_N$, we find a particle-substrate normal contact stiffness of $K_N = 4.0$ kN/m, and thus also obtain the particle-substrate shear stiffness $K_S = 3.5$ kN/m. We then use a least-squares fit to determine the interparticle shear stiffness G_S, where the quantity $((f_I - f_{HR})/f_I)^2 + ((f_{III} - f_{RH})/f_{III})^2$ is minimized, with f_{HR} and f_{RH} defined as in Eq. 2.2. For the uncoated sample, we obtain an interparticle shear stiffness of $G_S = 0.3$ kN/m (see Appendix A for stiffness calcualtions). In Fig. 2.2, we denote the fitted contact resonance frequencies using white solid lines on the right side of each panel. For the uncoated sample, we see an excellent agreement between the measured attenuation frequencies and the fitted contact resonance frequencies. For the sample coated with 40 nm of aluminum, the agreement is not as good. This difference may be due to deviations from the physical scenario described by our model due to the presence of the aluminum, including asymmetric interparticle contacts and the formation of "necks", which may lead to bending resistance not taken into account in the model.

2.4 Discussion

A particularly intriguing result is that the interparticle shear contact stiffness is over an order of magnitude smaller than the particle-substrate contact stiffnesses. As a comparison, we use the Hertz-Mindlin elastic contact model with theDMTmodel of an adhesive contact [138] to calculate theoretical contact stiffnesses. This results in predicted stiffnesses $K_{N,DMT} = 1.6$ kN/m, $K_{S,DMT} = 1.4$ kN/m, $G_{S,DMT} = 0.8$ kN/m, which gives a ratio of less than 2 between the particle-substrate and interparticle stiffnesses. Consistent with the trend observed in recent studies [77, 139], the measured particle-substrate normal contact stiffness is also over twice as large as predicted. A discrepancy between the estimated and measured values can be ascribed to factors such as uncertainty in the work of adhesion [121], plastic deformation, which may stiffen the contact [88, 140], or microslip at the contact, which may decrease the

shear contact stiffness [141].

For instance, prior studies have shown higher than predicted adhesion between dielectrics and reactive metals such as aluminum [142]. In addition, an examination of SEM images (shown in Appendix A) showed that the interparticle contact network is not uniform: even in closely packed regions, most particles do not form adhesive contacts with all six neighbors. This raises the question of how adhesive contact networks form following self-assembly, and may contribute to lower than predicted interparticle contact stiffnesses. Our measurement approach offers a unique opportunity to investigate this issue.

We have also studied the effect of the microspheres on SAW dispersion. Figure 2.4 shows the normalized magnitude of the two-dimensional Fourier transform of the scanned measurements taken in the monolayer region. Figure 4 shows the normalized magnitude of the two-dimensional Fourier transform of the scanned measurements taken in the monolayer region. Figure 2.4(a) shows spectra corresponding to the uncoated sample. Figure 2.4(b) shows spectra corresponding to the sample with 40 nm of aluminum. The spectra show a line corresponding to Rayleigh SAWs in the substrate, which has three gaps or regions of attenuation corresponding to the attenuation zones seen in Fig. 2.2. The highest and lowest zones appear as lighter-colored, attenuated regions, whereas the middle zone shows a clear gap with a curvature indicative of an avoided crossing. An emerging band gap can also be seen at the lowest resonance in Fig. 2.4(b).

Using the fitted contact resonance frequencies with the effective medium model for a monolayer of microspheres on an elastic substrate [130], we plot the calculated dispersion curves as the red dash-dotted lines in Fig. 2.4 (see Appendix A for material properties used). For the strong middle resonance and also the emerging avoided crossing at the lowest resonance in Fig. 2.4(b), we see reasonable agreement between experiment and theory in the curvature of the branches, which confirms that our model captures the coupling strength between the contact resonances and the SAWs. For resonances with weak coupling and low quality factors, hybridization gaps can appear as attenuation zones instead of avoided crossings [135],

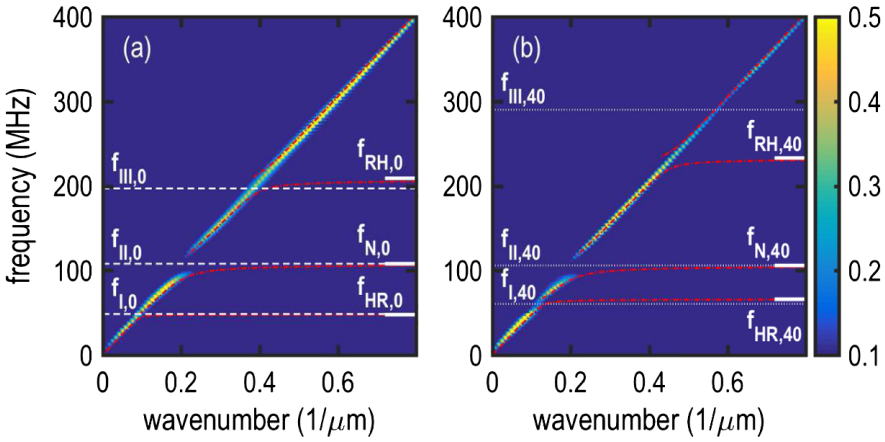

Figure 2.4: Surface acoustic wave dispersion in samples with (a) an uncoated monolayer and (b) a 40 nm thick aluminum coating. The color plot denotes the normalized magnitude of the calculated 2D Fourier spectra. The horizontal dashed and dotted lines correspond to the identified contact resonance frequencies for the uncoated sample and the sample with 40 nm of aluminum, respectively. The short horizontal lines on the right of the panels are the fitted contact resonance frequencies. The red dash-dotted lines are the dispersion curves calculated using the fitted resonance frequencies.

which explains why weaker horizontal-rotational resonances were not identified previously in Ref. [77].

As further analysis of the attenuation, we have applied a recently developed signal processing method called Spatial LAplace Transform for COmplex Wavenumber (SLaTCoW) recovery to the spatiotemporal data [120]. The 2D FFT used for Fig 2.4 only supplies a real wavenumber magnitude by taking the FFT in the spatial domain, however, the attenuation properties are not analyzed in this plot because attenuation is characterized by the complex wavenumber. Briefly, the SLaTCoW method allows for analysis of the complex wavenumber by taking the spatial laplace transform at each frequency, identifying the number of modes, and minimizing the cost function (Eq. 3 in Ref. [120]) to solve for numberwave amplitude,

phase, and real and imaginary parts of the complex wavenumber.

The SLaTCoW method is applied to the scanned data obtained from the uncoated sample, which produces dispersion curves related to the real and imaginary wavenumbers k_r^1 and k_i^1, as seen in Figs. 2.5(a,b), respectively. When analyzing only k_r^1, only the normal resonance f_N is clearly seen because of the bending due to the avoided crossing, while $f_H R$ and $f_R H$ do not appear because the weaker coupling does not induce a curvature of the dispersion relation, just as in Fig. 2.4. Turning to the dispersion curve corresponding to the imaginary wavenumber k_i^1, the utility of the SLaTCoW method is apparent, as the imaginary component shows peaks at all three resonance frequencies, with f_N having the largest magnitude, followed by $f_R H$ and lastly $f_H R$. The magnitude of k_i^1 corresponds to the rate of attenuation, which can also be seen by the spatial decay of the transimission spectra in Fig. 2.2(a), where the SAW pulse decays fastest at f_N and slowest at $f_H R$. Using this method allows for quantitative analysis of the attenuation which is not present with the 2D FFT in Fig. 2.4.

2.5 Conclusion

This work opens the door for the study of the contact based dynamics of low-dimensional microgranular systems, which, in contrast to their macroscale counterparts [128], may have additional acousto-optic [143] or acousto-plasmonic [144] functionalities, be rapidly and inexpensively manufactured via self-assembly, and find future use in chip-scale applications. The discovery of collective vibrational modes including rotations as well as displacements, along with the characterization of shear and normal contact stiffnesses in microscale particle assemblies, will lead to better and broader understanding of wave propagation in microgranular media with applications in shock mitigation, energetic materials, seismic exploration, and powder processing, and have implications for future studies of colloidal crystal systems [145,146]. This study reveals the critical role of particle rotations: for instance, without rotations, the upper rotational-horizontal resonance would not be present [130]. Our characterization method is complementary to existing techniques [118,147–149], as it is noncontact

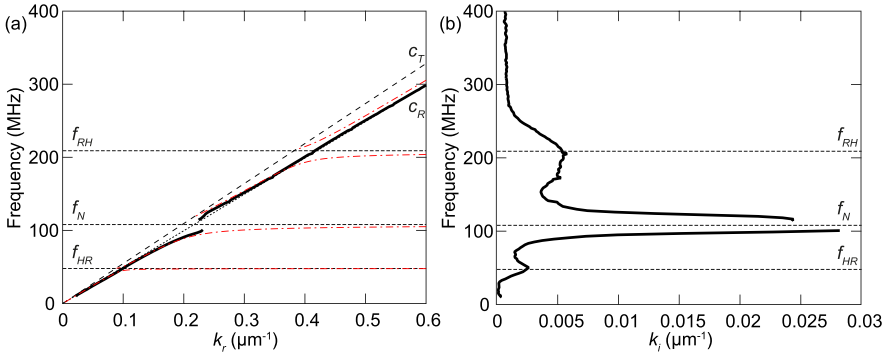

Figure 2.5: (a) Dispersion curves of SAWs propagating in a substrate with an adhered microsphere monolayer, corresponding to the real part of the wavenumber,k_r^1. Solid lines are dispersion curves calculated using the SLaTCoW method. Red dash-dotted lines are the dispersion curves calculated using a lossless model and the fitted contact resonance frequencies (denoted by the horizontal dotted lines). Rayleigh (c_R) and transverse (c_T) wave speeds are the straight dotted and dashed lines, respectively. (b) Dispersion curves of SAWs propagating in a substrate with an adhered microsphere monolayer calculated using the SLaTCoW method, corresponding to the imaginary part of the wavenumber, k_i^1. Horizontal dotted lines denote the fitted contact resonance frequencies.

and nondestructive, offers information about equilibrium contact stiffnesses, and, in contrast to other dynamic techniques involving isolated particles [118, 147, 148], enables the measurement of the interparticle contact stiffness in a microscale multiparticle assembly. Finally, the sensitivity to contact forces in the microgranular monolayer may be used in sensors for bioanalytical [150] and other applications.

2.6 Collaborator Contributions

M. Abi Ghanem contributed to signal analysis, particularly the 2D FFT, and the concept of electron-beam evaporation for coating on interparticle contacts. S. P. Wallen provided guidance for using the contact resonance equations to design the experiments to tune the

resonance via interparticle stiffness, as well as codes to produce and fit the theoretical dispersion relations. A. Khanolkar fabricated the microsphere samples via self-assembly. A. A. Maznev provided guidance of interpretation of experimental results. A. Geslain, S. Raetz, J. Laurent, C. Prada, A. Duclos, P. Leclaire, and J.-P. Groby developed and applied the SLaTCoW method to the scanned spatiotemporal data.

Chapter 3

LASER-INDUCED SPALLATION OF MICROSPHERE MONOLAYERS [1]

The detachment of a semiordered monolayer of polystyrene microspheres adhered to an aluminum-coated glass substrate is studied using a laser-induced spallation technique. The microsphere-substrate adhesion force is estimated from substrate surface displacement measurements obtained using optical interferometry, and a rigid-body model that accounts for the inertia of the microspheres. The estimated adhesion force is compared with estimates obtained using an adhesive contact model together with interferometric measurements of the out-of-plane microsphere contact resonance, and with estimated work of adhesion values for the polystyrene-aluminum interface. Scanning electron microscope images of detached monolayer regions reveal a unique morphology, namely, partially detached monolayer flakes composed of single hexagonal close packed crystalline domains. This work contributes to the fields of microsphere adhesion and contact dynamics, and demonstrates a unique monolayer delamination morphology.

3.1 Introduction

Microparticle adhesion is central to fundamental areas such as surface science [121], geological material mechanics [124], granular media dynamics [119], and even planet formation [152]. Improved understanding of microparticle adhesion has implications for applied areas including self-assembly [123], laser cleaning of semiconductors [153], powder processing [124, 125],

[1] Included in this chapter is material from Ref. [151]. Reprinted with permission from [M. Hiraiwa, M. Stossel, A. Khanolkar, J. Wang, and N. Boechler, "Laser-Induced Spallation of Microsphere Monolayers," *Langmuir*, vol. 32, no. 31, pp. 7730-7734, 2016.] Copyright 2016 American Chemical Society.

and drug delivery [115]. One method to study microparticle adhesion is to use laser-generated acoustic waves to eject the particles from a surface. This method has previously been used to study the adhesion of disordered assemblies of particles adhered to substrates [154, 155]. A closely related technique, which is typically used to study interfacial adhesion of thin films, is laser-induced spallation [156], wherein, a laser-generated acoustic compression pulse reflects from the free surface of the sample as a tensile pulse that causes delamination near the surface.

In this work, we study the delamination of semiordered microsphere monolayers adhered to an aluminum-coated glass substrate, which contain both hexagonal close packed (HCP) and disordered domains, using a laser-induced spallation technique. The particle-substrate adhesive force is estimated by monitoring the time-resolved displacements of the surface of the monolayer-coated substrate via optical inteferometry, and applying a rigid-body model that accounts for the microsphere inertia. We compare the estimated adhesive force with estimates made using an adhesive contact model with measurements of the out-of-plane contact resonance of the microspheres obtained using optical inteferometry [119], and with estimated work of adhesion values for the polystyrene- aluminum interface. Scanning electron microscope (SEM) images of the delaminated monolayer areas reveal a unique morphology wherein the monolayer has fractured into flakes that have partially reattached to the substrate and are composed of mostly single crystalline domains.

3.2 Experimental Section

A schematic of the sample used in this study is shown in Fig. 3.1(a). The substrate was purchased from EMF Corp. and consists of a 1.5 mm thick glass slide coated with a 100 nm thick aluminum film used to reflect light during the optical inteferometry measurements. A 400 nm thick aluminum film was applied on the opposite side via magnetron sputtering in order to absorb the pump pulse laser light. A 10μm thick waterglass film is deposited on the back of the 400 nm thick aluminum film via spin-coating, to increase the amplitude

of bulk longitudinal waves traveling through the substrate. A monolayer of 1μm diameter polystyrene (PS) microspheres is assembled on the top of the aluminum-coated substrate using a modified Langmuir-Blodgett technique [157], in which the microspheres are self-assembled at an air- water interface and then transferred to the substrate. This process results in a semiordered monolayer, with HCP crystalline domains of differing orientations as well as highly disordered regions, as can be seen in Fig. 3.1(b). To excite acoustic waves in the substrate, pump laser light is focused on the 400 nm aluminum layer. In all experiments, the plane of the sample surface is oriented vertically.

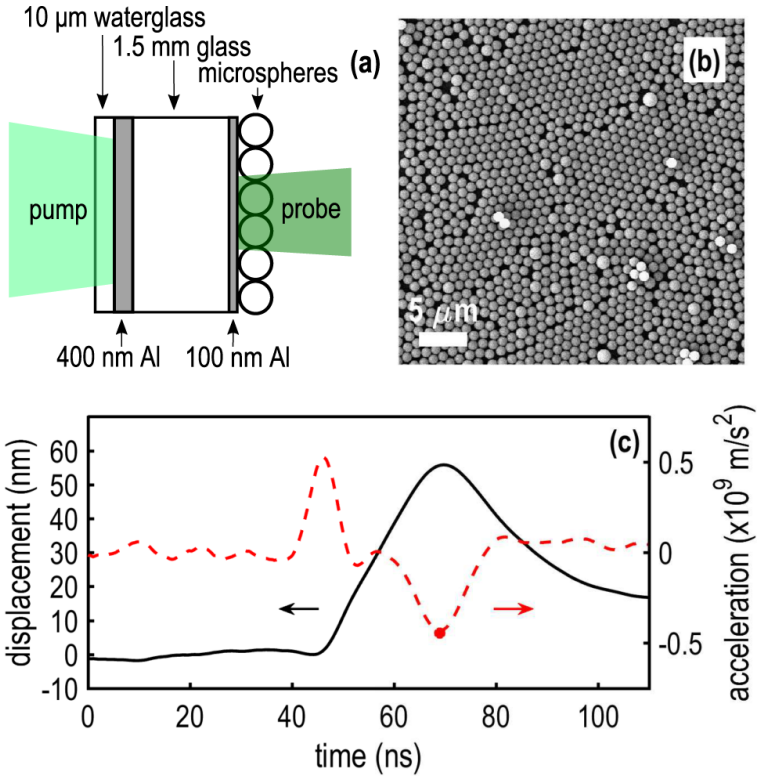

Figure 3.1: (a) Schematic of the sample and the laser-induced spallation setup. (b) SEM image of an untested monolayer. (c) Measured surface displacement (black solid curve) and calculated surface acceleration (red dashed curve) for a pump energy of 32 mJ. The marker indicates the identified point of maximum tensile force at the microsphere- substrate contact.

In the laser-induced spallation experiments, the pump light (1064 nm wavelength, 5 ns pulse duration) is focused to a spot size of approximately 2.5 mm diameter (determined by burn marks on ZAP-IT paper). Since the excitation ablates the energy-absorbing aluminum layer, new monolayer positions are tested after each pump pulse. To calculate the force acting on the monolayer, surface displacements are monitored with a Michelson interferometer, which consists of an argon laser (514.5 nm wavelength, continuous wave) focused on the 100 nm aluminum layer below the microsphere monolayer to a spot with an estimated diameter of approximately 30μm (at the $1/e^2$ intensity level). Interferometer signals are measured with a photodetector of 300 ps rise time (Electro-Optics Technology, model ET- 2030) and digitized on a 2.5 GHz oscilloscope (Tektronix DPO 7245C) at a sample rate of 20 Gsample/s. Surface displacements are obtained from the measured signal via the interference equation shown in Appendix B.

3.3 Results and Discussion

Figure 3.1(c) shows an example of the measured surface displacements induced by a 32 mJ pump pulse, for a case in which spallation occurred. We observe the arrival of an acoustic pulse of greater than 40 ns duration traveling at the longitudinal sound speed in the glass. We obtain the acceleration of the substrate by numerically differentiating the measured substrate displacement twice, and applying numerical smoothing to the photodetector output, displacement, velocity, and acceleration signals, as detailed in Appendix B. An example of such an acceleration profile, corresponding to the plotted displacement signal, is also shown in Fig. 3.1(c).

To calculate the force acting at the particle-substrate contact, we employ a simple model that accounts for the inertia of the microspheres and considers the microspheres to be rigid bodies that follow the substrate surface motion until detachment [154]. We calculate the force applied to the contact as $F = ma$, where m is the microsphere mass, calculated using a density provided by the manufacturer (Corpuscular, Inc.) of 1.06 g/cm^3, and a is

the measured substrate acceleration. This type of model is valid when the pulse duration is significantly longer than the period of the microsphere contact resonance (a vibrational mode where the microsphere moves like a rigid body, but has localized deformation around the point of contact that acts as a spring [118]). If the maximum tensile force induced at the contact exceeds the adhesive force, microsphere detachment occurs.

To identify the threshold at which spallation occurs, and thus the microsphere-substrate adhesive force, we make measurements over a range of pump pulse energies and search each measurement location for potential monolayer detachment using an optical microscope. For each pump energy, we observe a significant distribution in the measured surface acceleration, which we attribute to variations in the pump laser intensity and sample variations, such as the local thickness or consistency of the water glass layer. We identify a pump pulse energy of 32 mJ as an approximate threshold for which spallation occurs. Monolayer detachment is not consistently observed for pump pulse energies below 32 mJ, while the opposite is true for energies above 32 mJ. For a pump pulse energy of 32 mJ, spallation of the monolayer was observed for 5 out of the 10 tests conducted. By taking the average maximum deceleration measured for the 10 tests with 32 mJ pump pulse energy, and applying the inertial microsphere model, we obtain an estimated adhesion force of $F_{spall} = 0.22 \pm 0.07\mu$N. The magnitude of the uncertainty of the estimated adhesive force is the sum of the standard deviation of the identified maximum deceleration, and the average of the difference between the smoothed and unsmoothed acceleration signals at the identified point of maximum deceleration, multiplied by the microsphere mass, for the 10 measurements as detailed in Appendix B. As such, we note that the amplitude of the error bars do not account for inaccuracies that may result from fast changes in the substrate motion and the use of the inertial model, for instance, in the case of resonant particle removal where the rigid body assumption no longer holds.

After the spallation experiments, the sample is examined using a SEM. Images of the postspallation monolayer are shown for varied excitation amplitudes in Fig. 3.2. A mono-

layer region tested with a pump pulse just below the spallation threshold is shown in Fig. 3.2(a), and appears similar to the untested region, with no evidence of microsphere detachment. When the pump energy is slightly increased, noticeable gaps in the monolayer are observed, as is shown in Fig. 3.2(b). At higher energies, the amount of monolayer delamination increases, as can be seen in Fig. 3.2(c). Since the adhesive force is expected to have a statistical variation throughout the monolayer [158], it is not surprising that some patches of monolayer remain adhered to the surface near the onset of microsphere removal. We also observe that detached monolayer flakes resettle on the sample surface. Resettling of ejected particles has been observed previously by others [154], despite the plane of the sample's surface being oriented vertically. This was explained by the slowing of ejected particles by the Stokes drag in air, while long-range attractive forces eventually cause some particles to readhere to the surface [154].

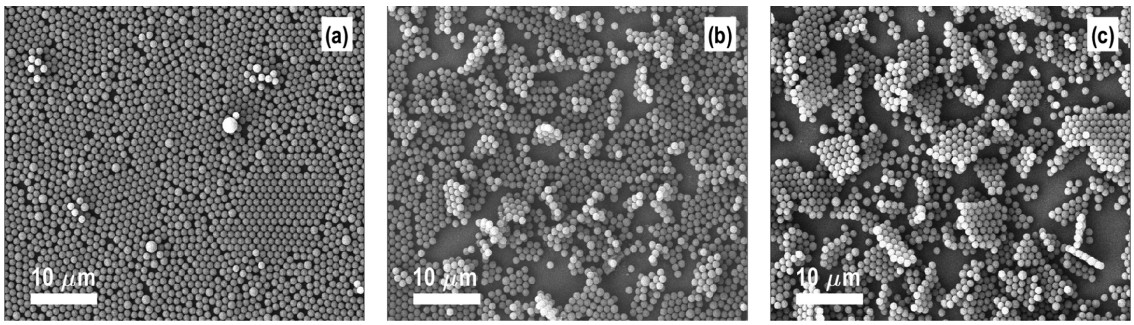

Figure 3.2: SEM images of a monolayer after excitation, which had surface acceleration (a) below, (b) just above, and (c) significantly above the spallation threshold.

We find that almost all of the delaminated flakes are composed of single HCP crystalline domains. We suggest that fracture of the monolayer into flakes is the result of interparticle decohesion along the weak boundaries that develop during the spallation process. In previous spallation experiments with continuous, ductile thin films, the excessive stress tended to lead to large scale plastic deformation in the film manifested by "blister" formation following the film delamination [159]. We speculate that the ordering of the monolayer flakes is due to

stronger interparticle cohesion for HCP regions than disordered regions. For instance, in disordered regions, particles are in contact with fewer of their neighbors, and as a result are more susceptible to fragmentation caused by in-plane and shearing stresses induced during the spallation process.

We compare the adhesion force obtained from the laser induced spallation experiments with that estimated from the out-of-plane microsphere contact resonance measured on a different region of the same sample. To excite the contact resonance, we generate a broadband bulk longitudinal acoustic pulse using a configuration similar to the spallation experiment, but at an amplitude significantly below the microsphere detachment threshold, as shown in Fig. 3.3(a). The out-of-plane contact resonance is excited upon arrival of the longitudinal wave, while the horizontal-rotational resonances [130] are not excited due to symmetry constraints. Out-of-plane displacements of the microspheres are measured using a grating interferometer [136], wherein a probe beam is focused on the microspheres and a reference beam is focused on a stationary region of the sample. Probe and reference beams (514 nm wavelength, continuous wave) are both focused to a diameter of 240μm (at $1/e^2$ intensity level), while the pump (532 nm, 430 ps pulse duration, 11μJ per pulse) is focused to a diameter of 400μm (at $1/e^2$ intensity level). The interferometric signal is measured with a photodetector of 500 ps rise time (Electro- Optics Technology, model ET-2030A), digitized with a 2.5 GHz oscilloscope (Tektronix DPO 7245C) at a sample rate of 20 Gsamples/s, and low-pass filtered with a cutoff frequency of 500 MHz. Using this setup, we obtain the signal shown in Fig. 3.3(b). The signal exhibits oscillations that begin when the bulk longitudinal acoustic wave arrives at the surface containing the microsphere monolayer. The Fourier spectrum of the oscillations following the broadband pulse is shown in Fig. 3.3(c) along with spectra corresponding to measurements made at two additional locations on the sample. Each of the three measurements show a single clear peak with an average frequency of $f_0 = 164$ MHz. While we observe little variation in frequency between the three measurement locations, we note that there can be large variation in the contact resonance frequency

between different samples [160]. We relate the resonant frequency to the contact stiffness by assuming the spheres act as a spring mass oscillator with resonant frequency f_0, such that $f_0 = 1/2\pi\sqrt{K_c/m}$. By linearizing the Hertzian contact model around the equilibrium contact area, we obtain the adhesive force in terms of the contact stiffness, K_c, such that $F_{CR} = (2K_c/3)^3/RK^2$, where F_{CR} is the adhesive force, K is the effective modulus, defined as $K = [(3/4)(((1-\nu_s^2)/E_s) + ((1-\nu_l^2)/E_l))]^{-1}$, and R is the effective radius of curvature of the contact (equal to the microsphere radius for spherical-planar contact geometry) [75]. The effective modulus K is expressed in terms of Young's modulus, E, and Poisson's ratio, ν, and the subscripts s and l denote the sphere and the substrate, respectively. Using elastic properties of Young's modulus $E_l = 62$ GPa and Poisson's ratio $\nu_l = 0.24$ for the aluminum layer [161], and $E_s = 4.04$ GPa and $\nu_s = 0.32$ for the PS microspheres [139], we find an adhesive force of $F_{CR} = 3.8$ μN and a contact radius of 70 nm.

The adhesion force estimated from the contact resonance measurements is significantly larger than the force estimated from the spallation measurements. To further investigate this discrepancy, we measure the contact radius of the microspheres by taking an average of five side-view SEM images of different microsphere-substrate contacts, for the same sample upon which the spallation and contact resonance measurements were conducted. A representative SEM image of the microsphere contact is shown in Fig. 3.4. According to the Hertzian contact model, larger adhesive forces should result in larger contact radii. Using the estimated adhesion forces with the Hertzian contact model, we predict a contact radius of 70 nm based on the contact resonance measurements, and a contact radius of 27 nm based on the spallation measurements. From the SEM images, we measure an average contact radius of 150 ± 20 nm, which is significantly larger than predicted by both measurements. As a further point of comparison, using the Derjaguin- Muller-Toporov (DMT) model for adhered microparticles [138, 162] we calculate an adhesive force of $F_{DMT} = 2\pi wR = 0.36\mu$N and a contact radius of 32 nm, where $w = 0.113$ J/m^2 is the estimated work of adhesion between PS and alumina (assuming a native oxide layer) [139]. While there can be significant uncer-

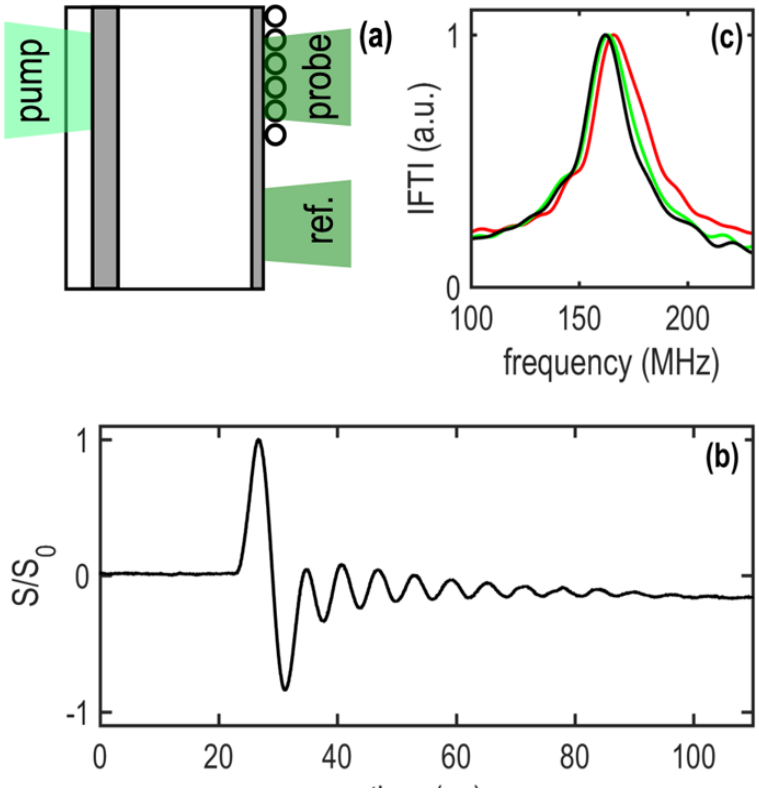

Figure 3.3: (a) Schematic of the experimental setup used to measure the microsphere contact resonance. The sample is the same as in Fig. 3.1a. (b) Measured signal. (c) Fourier spectrum for measurements made on three different sample locations. The black curve in panel c corresponds to the signal in panel b.

tainty in predicting work of adhesion values (particularly in the case of reactive metals such as aluminum), and higher values of work of adhesion have been observed than are predicted by van der Waals adhesion models [142], the size of the contact radius measured from the SEM measurements would require unrealistically large adhesive forces in the context of an elastic contact model. The large, measured contact radius may instead indicate the presence of plastic deformation near the contact. By observing PS microspheres adhered to substrates using a SEM, previous studies have also found the contact radius to be larger than predicted by elastic contact models [163, 164].

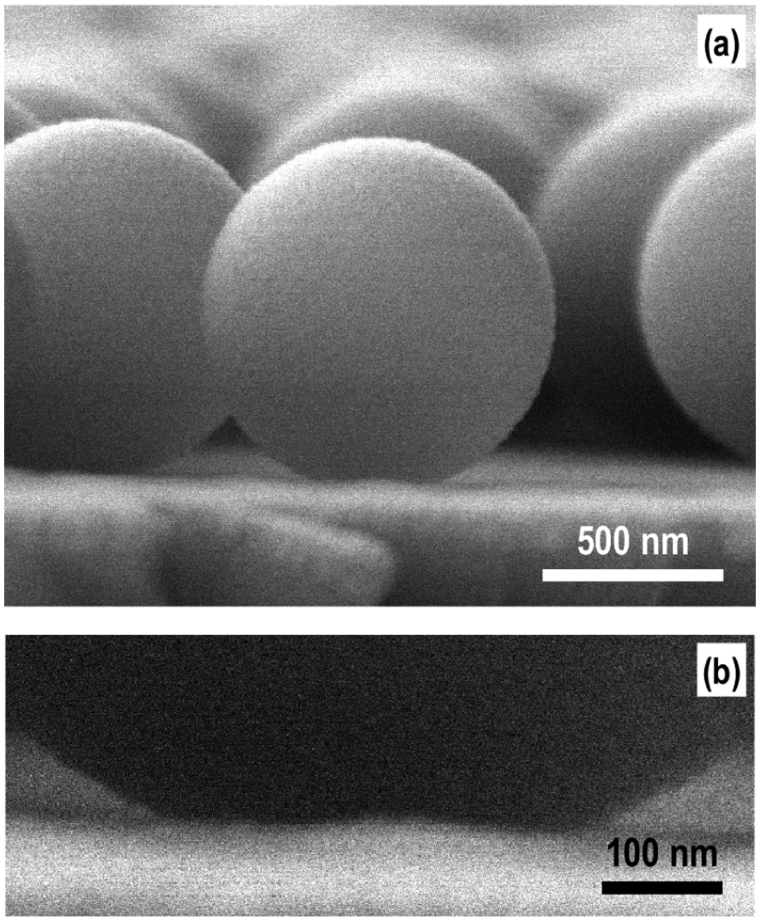

Figure 3.4: (a) Side-view SEM image of a microsphere monolayer. (b) Close up of the interface between a microsphere and the substrate.

The presence of plastic deformation adds further complexity to the analysis, as the adhesion force estimated from the contact resonance measurements and the contact radius estimated from both the contact resonance and spallation measurements are based on an elastic contact model. Estimation of the adhesion and contact properties utilizing an elastoplastic contact model can prove challenging, both near particle equilibrium and separation, because of the uncertainty involved with the choice of a plasticity model and the interplay of material softening, hysteric material behavior, and geometric nonlinearity [165, 166].

Independent of potential plastic deformation of the contact, it is surprising that the adhesion force estimated from the spallation experiments, which did not involve the assumption of any contact model, is so low, given the large contact radii observed in the SEM images. This difference may be due to assumptions used in the spallation adhesion force estimation process, such as the microspheres being approximated as rigid bodies. In addition, the discrepancy between the adhesion force estimated from the contact resonance and spallation measurements highlights a potential fundamental difference between the two methods related to variations in particle size and particle-substrate adhesion. For instance, in the spallation experiments, a few particles of larger size or weaker particle- substrate adhesion may pull adhered neighboring particles away from the substrate at lower accelerations, and result in the identification of an effectively lower detachment threshold. In contrast, in the contact resonance measurements the observed resonance is representative of the average contact stiffness across the measurement area, and would see the effect of polydispersity in broadening of the resonance. In future studies, a more extensive comparison between dynamic adhesion characterization methods and quasi-static, contact-based techniques, such as atomic force microscopy [149], may prove useful in clarifying the sources of the observed discrepancies.

3.4 Summary and Conclusions

This work provides data regarding the adhesion, contact mechanics, and delamination of microsphere monolayers. The unique monolayer flakes may find future application in laser induced particle transfer applications [167], and provide an opportunity to study the in-plane fracture mechanics of microsphere monolayers. Comparison of the contact properties estimated from the spallation, contact resonance, and SEM measurements showed significant discrepancies, which we speculate may stem from effects not accounted for in the modeling process such as plastic deformation, nonrigid body microsphere dynamics, and variations in particle size and adhesive forces. The microsphere monolayer studied in this work represents a microscale analogue of a macroscale granular crystal [128]. While many studies have shown macroscale granular crystals to exhibit rich physics, the study of their microscale

counterparts is an emerging field [76]. This work paves the way for the study of spallation and highly nonlinear phenomena in three-dimensional microscale granular crystals. Related laser induced spallation techniques generating shear [168] or mixed-mode [159] elastic waves may be useful to study the shear strength of adhered microparticles, or the propagation of rotational modes in three-dimensional microscale granular crystals. Rotational modes have only recently been observed in three-dimensional macroscale [86] and two-dimensional microscale granular crystals [119]. Finally, the microparticle adhesion measurements obtained as part of this study may find future use in self-assembly, laser cleaning, powder processing, or drug delivery applications.

3.5 Collaborator Contributions

Melicent Stossel collected data using the laser-induced spallation technique and assisted with signal processing. Amey Khanolkar fabricated the samples via self-assembly. Professor Junlan Wang provided use of the high-amplitude nanosecond laser setup and overall guidance on all components of this chapter.

Chapter 4

LONGITUDINAL EIGENVIBRATION OF MULTILAYER COLLOIDAL CRYSTALS AND THE EFFECT OF NANOSCALE CONTACT BRIDGES [1]

Longitudinal contact-based vibrations of colloidal crystals with a controlled layer thickness are studied. These crystals consist of 390 nm diameter polystyrene spheres arranged into close packed, ordered lattices with a thickness of one to twelve layers. Using laser ultrasonics, eigenmodes of the crystals that have out-of-plane motion are excited. The particle–substrate and effective interlayer contact stiffnesses in the colloidal crystals are extracted using a discrete, coupled oscillator model. Extracted stiffnesses are correlated with scanning electron microscope images of the contacts and atomic force microscope characterization of the substrate surface topography after removal of the spheres. Solid bridges of nanometric thickness are found to drastically alter the stiffness of the contacts, and their presence is found to be dependent on the self-assembly process. Measurements of the eigenmode quality factors suggest that energy leakage into the substrate plays a role for low frequency modes but is overcome by disorder- or material-induced losses at higher frequencies. These findings help further the understanding of the contact mechanics, and the effects of disorder in three-dimensional micro- and nano-particulate systems, and open new avenues to engineer new types of micro- and nanostructured materials with wave tailoring functionalities via control of the adhesive contact properties.

---

[1] Included in this chapter is material from Ref. [169].

[M. Abi Ghanem, A. Khanolkar, S. P. Wallen, M. Helwig, M. Hiraiwa, A. A. Maznev, N. Vogel, and N. Boechler, Longitudinal eigenvibration of multilayer colloidal crystals and the effect of nanoscale contact bridges," *Nanoscale*, vol. 11, no. 12, pp. 5655-5665, 2019.] - Reproduced by permission of The Royal Society of Chemistry.

4.1 Introduction

Colloidal self-assembly has emerged as a "bottom-up" approach to manufacturing nanostructured materials with controlled hierarchical architectures, and has enabled their fabrication inexpensively and on a large scale [93]. Primarily investigated for their unprecedented features in areas like photonics [143, 170], plasmonics [171], and biosensing [172, 173], self-assembled colloidal crystals, which consist of ordered, close-packed lattices of micro- to nanoscale spherical particles [174], have also shown promise in the context of their vibrational dynamics or "phononic" properties [94, 175].

In a colloidal crystal, particles may be dispersed in a liquid or in a solid matrix, or the host medium may be absent (e.g. a "dry" colloidal crystal) [176–178]. Macroscale analogues of dry colloidal crystals, often referred to as "granular crystals", have also been a topic of significant interest due to their unique dynamics [52, 76, 128]. In granular crystals, spheres arranged in close packed arrays can be thought to move similar to rigid bodies and interact via small contact regions (compared to the particle size) that elastically deform and act as massless springs. Such contact-based dynamics have underlied the large interest in granular crystals, as the interplay of the contact nonlinearity, typically modeled by the Hertzian contact model [75], coupled with dispersion induced by mechanisms such as structural periodicity [128] and local resonances [86, 179, 180] have been shown to enable new acoustic wave tailoring strategies [76, 128]. However, until recently, studies concerning the contact-based dynamics of granular crystals have been restricted to systems composed of millimeter to centimeter-sized spheres. Acoustic studies of colloidal crystals, on the other hand, mostly focused on colloids in a host medium [94, 95, 181]. Until recently, the contact based dynamics of dry colloidal crystals or "micro- to nanoscale granular crystals", wherein the Hertzian contacts are preserved and play a major role, remained an unexplored territory.

The contact-based dynamics of dry, two-dimensional (2D) colloidal crystal monolayers have been examined in several recent studies [77, 119, 130, 160, 182, 183]. In these works, it was

shown that adhesive van der Waals forces [121] statically compress the interparticle and particle–substrate contacts, and effectively linearized the crystal dynamics for small displacements (relative to the static deformation). This compression resulted in the formation of multiple contact resonances of the crystal, including modes with both translational as well as coupled translational-rotational motion [119, 130, 182, 183]. In contrast, the contact-based dynamics of three-dimensional (3D) colloidal crystals remain largely unexplored. Using a Brillouin Light Scattering spectroscopic technique, a previous study exploring 3D colloidal crystal dynamics revealed a single resonant peak that was attributed to a band of contact-based modes; however, the individual eigenmodes were not resolved [95]. Laser ultrasonic techniques have also been used to measure the transmission of hypersonic acoustic waves traveling through dry 3D colloidal crystals [143, 184]. In contrast to the study presented herein, the vibrational modes observed in Ref. [184] were eigenmodes of isolated spheres (with frequencies significantly higher than the contact-based modes concerned in this work). A presence of an overdamped "low-frequency continuum mode" that was attributed to shear waves was also suggested in Ref. [184]; however, its frequency was not identified. Similarly, the measurements presented in Ref. [143] provided limited information concerning the acoustic modes of the crystal, no characterization of the interparticle contact stiffnesses, and, due to the sintering of the crystal, we expect limited dynamic deformation of the particle contacts was involved. Several studies have also explored the contact-mediated acoustics of 3D colloidal films; however, these were either disordered [96, 185], or the spheres were separated by large ligands [97, 186, 187] or polymer tethers [129] that approach the particle size and result in non- Hertzian contact mechanics.

In this work, we study the longitudinal contact-based vibration of self-assembled, dry, 3D colloidal crystals with long range order of varied thicknesses, and measure multiple, discrete eigenmodes of the crystal. In contrast to prior studies, using our laser ultrasonic technique, we are able to access the low-frequency, contact-based modes of the 3D crystals, and our spheres are not functionalized with large connective ligands that can cause deviation from the

Hertzian mechanics of elastically deforming spheres in contact. We correlate the resulting contact stiffnesses, extracted by way of a coupledoscillator model, with scanning electron microscopy (SEM) and atomic force microscopy (AFM) observation of the contacts, and find that nanometric bridges surrounding the contacts, which are much smaller than the particle size, can more than triple the contact stiffness. In all cases, we find higher contact stiffnesses for our self-assembled crystals than those predicted using adhesive elastic contact models [137, 138]. We find also that the bridge sizes and contact stiffness vary with sample fabrication method, and that the contact stiffness can decrease with increasing numbers of crystal layers. By studying the quality factors of the measured eigenmodes, and comparing them with an analytical model that estimates acoustic energy radiation into the substrate based on the estimated impedance mismatch between the colloidal crystal and the substrate, we gain insight into energy loss mechanisms in our system. From this comparison, we suggest that energy leakage plays a large role for low frequency modes but is surpassed by disorder- or material-induced losses as the modal frequency increases. Improved understanding of the dynamics of self-assembled, dry, 3D colloidal crystals will help enable the design of new microstructured materials with ultrasonic wave tailoring capabilities that leverage contact-based nonlinearities analogous to those present in macroscale granular crystals [52, 76, 128]. We expect that potential applications for such materials may range from signal processing to impact mitigation and energetic material design.

4.2 Methods

For the colloidal crystal fabrication, we use monodisperse polystyrene spheres of diameter D = 390 nm that form a high crystalline order. The colloidal crystal is assembled on a substrate that consists of a 1.5 mm glass microscope slide, which is coated with a 100 nm thick layer of aluminum to absorb the optical pump energy and then a 20 nm thick silica layer to facilitate the self-assembly process. The polystyrene spheres are synthesized using a surfactant-free emulsion polymerization process [188]. The crystals are fabricated using a vertical convective self-assembly technique [174, 189], using varied solvents and purification

strategies, as is detailed in Appendix C. A 20 mL capacity glass scintillation vial is filled with 10 mL of the colloidal suspension. The substrate is then held vertically while being immersed in the suspension. The substrate and suspension are then left to dry in an oven or in ambient laboratory conditions, as listed in Appendix C. After complete drying, colloidal crystals with millimeter areas of defined and uniform thicknesses are obtained.

Laser ultrasonic characterization is performed with optical pump pulses (450 ps pulse duration, 532 nm wavelength, 7μJ pulse energy, and 1 kHz repetition rate) incident through the glass slide are focused onto the aluminum film. The pump pulse is focused to an elliptical spot (436μm $\times$ 76μm at $1/e^2$ intensity level) or a 200μm diameter circular spot, depending on the size of the layer being characterized (see Appendix C for details). The vibrations are detected with a phase-mask based interferometer [136] in which a single continuous wave (CW) laser beam (514 nm wavelength and 52 mW average power) is incident on a phase-mask and split into ± 1 diffraction orders to produce probe and reference beams focused to 40μm diameter spots. The probe is focused through the colloidal film onto the aluminum surface, while the reference beam is incident directly on the aluminum surface of a blank region of the substrate. The separation between the probe and reference beams is 4 mm. Upon reflection from the sample, the probe and reference are recrossed onto the phase mask, and recombined interferometrically onto an amplified silicon photodetector where the signal is digitized and recorded using an oscilloscope, and averaged over $10^4 - 10^6$ pump pulses.

4.3 Results and Discussion

Our colloidal crystals consist of close-packed, ordered arrangements of polystyrene spheres of diameter $D = 390$ nm, which are assembled on an aluminum-coated glass microscope slide, and are fabricated by vertical convective self-assembly [174, 189], as shown in Fig. 4.1(a). Regions with uniform layer thickness can be easily identified under a microscope from their different coloration, as is illustrated in Fig. 4.1(c). In the most densely packed case, this geometry represents perfectly registered stacks of hexagonally close-packed (HCP) or face-

centeredcubic (FCC) colloidal monolayers. A representative SEM image of our colloidal crystal can be seen in Fig. 4.1(d). The distinct structural coloration enables us to identify regions with defined layer thickness and thus study, in detail, the thickness-dependent contact-based acoustic properties of the crystals. To characterize the longitudinal acoustic response of the colloidal crystals, we use a laser ultrasonic technique that is illustrated in Fig. 4.1(b). Absorption of the pump pulse energy by the aluminum film induces a rapid thermal expansion that excites mechanical vibration of the crystal and launches acoustic waves in the substrate. In the colloidal crystal, longitudinal vibrations with out of plane motion are predominantly excited, as the excitation of transverse vibrations is hindered by symmetry constraints. These vibrations are detected with a phase-mask-based interferometer [136], which is preferentially sensitive to out-of-plane displacements [119]. As a result of the semi-transparency of the colloidal crystal, we expect that the probe signal contains contributions due to displacement of the surface of the colloidal crystal, scattering and refractive index changes within the colloidal crystal, and displacement of the aluminum–silica interface.

Figure 4.2(a) shows a signal acquired on a twelve-layer-thick region of a colloidal crystal sample, using the optical characterization method shown in Fig. 4.2(b). A sharp initial rise due to the arrival of the pump pulse at the sample followed by a slow decay associated with thermal diffusion is observed. The periodic oscillations in the signal represent the out-of-plane longitudinal vibrations of the colloidal crystal. The power spectrum (amplitude squared of the Fourier transform spectrum) of the time-derivative of the signal in Fig. 4.2(a) is shown in Fig. 4.2(b), wherein five spectral peaks can be distinguished. The fundamental peak has a frequency $f_1 = 70$ MHz. The intensities of the subsequent peaks decrease with increasing frequency, such that the intensity of the fifth peak is over three orders of magnitude lower than that of the fundamental peak. We suggest that this is due, in part, to the step-like nature of the excitation, which more efficiently excites modes at lower frequencies, and the increased susceptibility of shorter-wavelength, higher-frequency modes to disorder-induced scattering [190]. Each of the modes identified in the spectrum shown in Fig. 4.2(b) are

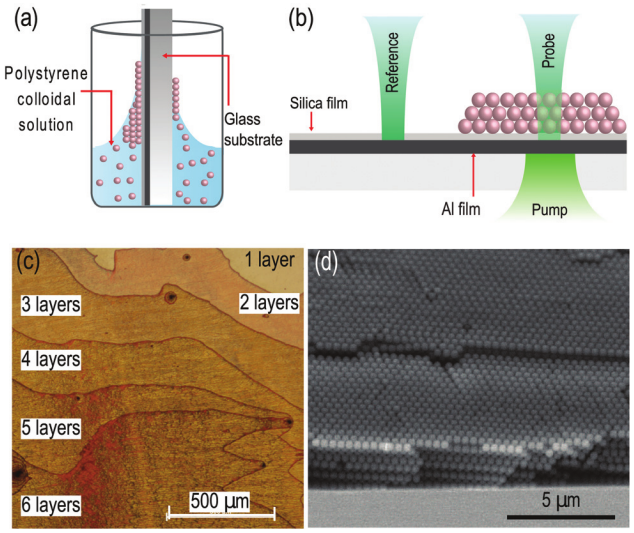

Figure 4.1: (a) Schematic of the multilayer convective self-assembly technique. (b) Illustration of the laser ultrasonic technique used to excite and measure eigenmodes of the colloidal crystal. (c) Optical microscope image showing multiple regions of the colloidal crystal with different layer thicknesses. (d) Representative SEM image of the colloidal crystal.

denoted by open diamond markers, and are plotted as function of mode number in Fig. 4.2(d) using the same markers. We compare the measured frequencies to the modal frequencies of a continuous film with boundaries that are fixed on one side and free on the other, given by $f_i = \frac{(2i-1)c}{4H}$, where i is the mode number, and c and H are the longitudinal sound speed and thickness of the film, respectively [186]. In our sample, the substrate and the crystal are mechanically coupled, with the substrate not strictly rigid. We expect much of the measured vibrations to be confined to the colloidal crystal, due to the large impedance mismatch between the crystal and the substrate. The modal frequencies of the continuous film fixed to the substrate on one side are plotted using blue filled circle markers in Fig. 4.2(d), where the sound speed of the film is chosen such that the frequency of its fundamental mode matches the experimentally measured fundamental mode. From Fig. 4.2(d), we see that the five measured modes approximately follow the linear trend of the calculated fixed-free

film modes as the mode number increases. Similar observations have been made in previous studies on nanocrystal superlattices interacting via ligands that have shown equally-spaced modes [186].

While the observed modes are well described by the linear relationship corresponding to the continuous film model, we develop a quasi-one-dimensional coupled oscillator model to describe our system and analyze the contact stiffnesses, in which we treat the spheres as rigid bodies connected by massless springs. Similar springs-in-series models (without the lumped masses) have been previously used to study the quasistatic nanoindentation of multilayer colloidal crystals composed of hollow silica nanospheres [191]. We implement a discrete element model because the measured frequencies are lower than the lowest intrinsic spheroidal mode of the particles (2.62 GHz) [127], and the discrete model enables us to separately describe particle–substrate and interlayer contact stiffnesses. A schematic of our quasi-one-dimensional coupled oscillator model is illustrated in Fig. 4.2(c). The particle–substrate contact between the first layer and the substrate is represented by an axial contact spring of stiffness K_N, while the interparticle normal and shear contacts involved in subsequent layers are represented by axial and transverse springs of stiffness G_N and G_S, respectively. The normal and shear stiffnesses are modeled using linearized Hertzian [75] and Hertz–Mindlin contact models [137]. We define an effective interlayer contact stiffness G_e oriented along the out-of-plane direction, which incorporates the contributions from the three pairs of interparticle normal and shear contact springs, and can be expressed as:

$$G_e = G_N(2 + \nu^*) \tag{4.1}$$

where for statically compressed Hertzian and Hertz–Mindlin contacts, $\nu^* = \frac{G_S}{G_N} = 2\frac{1-\nu_P}{2-\nu_P}$ is the ratio of the interparticle shear and normal contact stiffnesses, and ν_P is the Poisson's ratio of the polystyrene spheres (see Refs. [137,192] and Appendix C for stiffness calculations). Using Eq. 4.1, the colloidal crystal can be simplified to a quasi one-dimensional coupled oscillator system, where each of the oscillators have mass per unit area M, and are connected

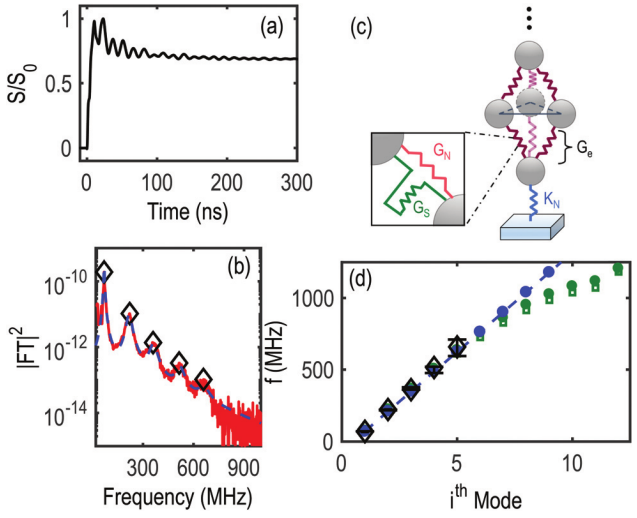

Figure 4.2: (a) Time domain signal corresponding to the out-of-plane eigenvibrations of a 12-layer-thick colloidal crystal. The signal amplitude S is normalized to its maximum amplitude S_0. (b) The solid red line denotes the power spectrum of the time-derivative of the signal in (a), and the dashed blue line denotes the sum of five Lorentzians fitted to the measured spectrum. (c) Schematic of the quasi-one-dimensional coupled oscillator model. (d) Modal frequencies as a function of mode number. Black diamond markers are the modes identified in (b) denoted by the same marker type. The blue circle markers represent the calculated modal frequencies for a fixed-free continuum film adhered to a rigid substrate, where the first mode is matched to the measured fundamental mode. The blue dashed line is a visual guide to the blue circle markers, and represents a wave speed of 1060 m s^{-1}. The green markers represent the calculated modal frequencies of the coupled oscillator system using a particle-substrate stiffness obtained via a monolayer region of the same sample measured in (a, b) and an interlayer contact stiffness fitted to the fundamental measured mode (open square markers), and to all five measured modes (filled circle markers). The error bar half-widths in the measured spectral peaks denote the maximum shift in the position of the peaks when the power spectrum time window is adjusted by up to 4 ns.

to one another by springs of stiffness per unit area G. Here, $M = m/A_P$ and $G = G_e/A_P$, where m is the mass of one of the spheres and $A_P = \sqrt{3}D^2/2$ is the area of the primitive unit cell in the HCP lattice. Although the crystal may also be in the FCC configuration, we assume HCP packing for the purpose of this article. The equivalent one-dimensional coupled oscillator system reduces to a chain of spheres of mass m connected to one another by springs of stiffness G_e, and connected to the substrate by a spring of stiffness K_N. The mass of the sphere is calculated using the density $\rho = 1060$ kg m^{-3} of polystyrene [139]. Since our measurements are sensitive to the out-of-plane direction only and we excite primarily longitudinal plane waves, we neglect adhesive contact forces in the transverse direction between neighboring spheres within the same layer.

We first apply our quasi-one-dimensional coupled oscillator model to the spectrum shown in Fig. 4.2(b). Using a single oscillator model, we first determine the particle–substrate contact stiffness K_N by measuring the out-of-plane contact resonance frequency f_1, m for a monolayer region of the same sample and using the relation $K_N = (2\pi f_{1,m})^2 m$. Using our coupled oscillator model and the experimentally determined particle–substrate contact stiffness K_N, we then solve for the effective interlayer contact stiffness G_e of the measured twelve layer region (assuming that all interlayer effective contact stiffnesses are the same), by matching each of the measured modes shown in Fig. 4.2(b) to the corresponding eigenfrequency. Taking the average value of these effective interlayer stiffnesses, determined for each mode, we obtain a value of $G_e = 0.42$ kN m^{-1}. If only the fundamental mode is used, we obtain an effective interlayer thickness $G_e = 0.38$ kN m^{-1}, which is 8% lower than the corresponding stiffness obtained by fitting all five measured modes. We note that these effective contact stiffnesses are similar to the stiffness found in Ref. [95] for colloidal crystals composed of similar-sized PS spheres with FCC packing. Using these effective interlayer stiffnesses, we then recalculate and plot the resulting modes in Fig. 4.2(d), where the green open squares were calculated using the stiffness found by fitting only the fundamental mode and the green closed circles using all five measured modes. In both cases, the highest calculated mode

deviates from the dispersion trend defined by the lower frequency modes due to the defect caused by the differing particle–substrate contact stiffness.

To similarly characterize the contact stiffnesses of colloidal crystals of different layer thicknesses, we perform measurements on multiple samples with defined layer thicknesses, ranging from one to twelve layers, as is shown in Fig. 4.3. Each sample was also fabricated using different fabrication parameters, including particle concentration, solvent (deionized water or ethanol), temperature of the drying environment, and number of times the colloidal suspension was centrifuged and the supernatant discarded to remove impurities from the solution. A tabulated list of the fabrication parameters used for each sample is included in Appendix C. We note that, in contrast to the spectrum shown in Fig. 4.2(b), fewer peaks were observed for other measurement regions and samples. In addition to being a result of the higher number of averages (106) used for the measurement location of Fig. 4.2(b), the presence of the additional peaks in Fig. 4.2(b) suggests reduced dissipation, which consequently may indicate lower disorder within that measurement area. This is further supported by an observed higher quality factor of the fundamental mode for this region ($Q \sim 12$), compared to other measured regions ($Q \sim 3 - 7$). The quality factor is obtained by fitting a Lorentzian distribution to the fundamental mode in the measured power spectra.

Figure 4.3(a) shows the Fourier spectra measured for regions of different layer thicknesses across the two samples where we could obtain a measurement of the out-of-plane contact resonance in the monolayer region. The red curves in Fig. 4.3(a) correspond to the sample characterized in Fig. 4.2, which we refer to as "Sample 1", and the blue to a different sample, which we refer to as "Sample 2". Figure 4.3(b) shows the frequency of the fundamental mode for all regions measured, as a function of the number of layers in that region. Each marker type corresponds to a different sample. The red and blue markers in Fig. 4.3(b) correspond to the spectra denoted by the same markers in Fig. 4.3(a). The gray markers denote samples for which a resonance was not detected in the monolayer region. We suggest that the absence of a monolayer resonance may be due to a combination of low quality

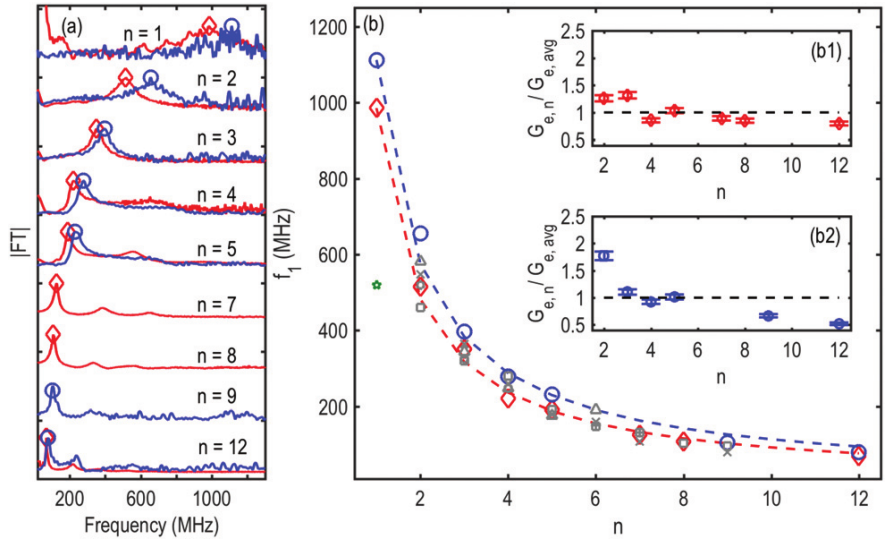

Figure 4.3: (a) Fourier Transform spectra of the time-resolved interferometric signals recorded from measurements on two colloidal crystal samples with thickness ranging from one to twelve layers. The Fourier Transform amplitude is plotted in linear scale, and offset for each layer thickness. (b) Frequencies of the fundamental mode plotted for colloidal crystals of varying number of layers (n) in the two samples from the peaks in the spectra in (a). The blue and red dashed lines indicate the frequencies of the fundamental eigenmode of a coupled oscillator system using the particle–substrate contact stiffness from the monolayer measurement (K_N) and the measured mean effective interlayer contact stiffness ($G_{e,avg}$). The gray markers represent frequencies of the fundamental modes of colloidal crystals fabricated with differing selfassembly parameters, but for which a monolayer resonance could not be measured. The green star marker represents the frequency measured on a monolayer that was pre-assembled at an air/water interface and subsequently transferred to a solid substrate. The inset highlights the variation of the effective interlayer contact stiffness for different layer thicknesses ($G_{e,n}$) in the two samples shown in (a). Red makers and lines correspond to Sample 1 and blue markers and lines to Sample 2 in all panels.

factors observed for many of the monolayer regions, as can be seen by the broad peaks of the monolayer spectra in Fig. 4.3(a), and the possibility that the monolayers have frequencies above our detection bandwidth of $\sim$ 1 GHz. For all samples we observe a similar, and expected, trend of decreasing fundamental mode frequency with increasing layer thickness. As a point of comparison to the samples fabricated using the vertical deposition convective self-assembly technique and prior studies on monolayer contact resonances [77,119,139,160], we fabricated and measured a sample consisting entirely of a colloidal crystal monolayer using a modified Langmuir–Blodgett technique involving pre-assembly of the monolayer at an air/water interface and subsequent transfer to a solid substrate [157]. The monolayer contact resonance on this air/water monolayer sample is found to be significantly lower than those measured for the samples fabricated using the vertical convective self-assembly technique, and is denoted by the green star marker in Fig. 4.3(b).

We repeat the previously described process to determine the effective interlayer contact stiffness for the different layer thicknesses tested on Samples 1 and 2. As the effective interlayer contact stiffness estimated using the fundamental and higher order modes was found to be reasonably close, and we do not have access to higher order modes for many of the regions tested, we fit only using the measured fundamental mode and the particle–substrate contact stiffness, determined from the monolayer region on the same sample, to find the effective interlayer contact stiffness for each thickness ($G_{e,n}$). The resulting effective interlayer contact stiffnesses, normalized by the average interlayer contact stiffness (Ge, avg) (across all layer thicknesses for the corresponding sample), are plotted in the insets Fig. 4.3(b1 and b2) as a function of thickness. The half-width error bars for each marker in the insets represent the 8% error in the effective interlayer stiffness calculated using the fundamental mode only or the first five eigenmodes in the coupled oscillator model. Each sample is denoted with the same marker type and color throughout Fig. 4.3.

The insets in Fig. 4.3(b1 and b2) show the variation of the effective interlayer stiffness in regions of differing thicknesses within the same sample. The effective interlayer stiffness

measured on different layer thicknesses in Sample 1 shows little variation, with an average value of 0.44 kN m^{-1}. On the other hand, we find that the effective interlayer stiffness decreases with increasing layer thickness in Sample 2, ranging from 1.2 kN m^{-1} in the bilayer region to 0.35 kN m^{-1} in the twelve-layer region of the sample. We speculate the decrease in stiffness could be due to increased disorder, as has been previously suggested in Ref. [185], or to a reduced density of impurities near the contact with increasing layer thicknesses. The presence of such impurities is to be expected as a by-product of colloidal synthesis processes. A decreasing density of impurity aggregation near the contacts with increasing layer thickness could thus also be expected, as thinner layers are deposited first in the drying process, and the impurities would first aggregate in these regions, leaving the solution, and reducing their availability for thicker layers deposited later in time. To verify the chemical nature of such impurities, we conducted IR spectroscopy on the material left over by separating the polystyrene particles from the colloidal dispersion, and then condensing and drying the supernatant (shown in Fig. 4 in Ref. [188]). In addition to signals of polystyrene, the IR spectrum of this material showed additional peaks associated with comonomer groups, which confirmed the presence of shortchained polymers in the colloidal dispersion. Indeed, spectroscopic and interfacial analyses of polymer colloidal dispersions reported previously in the literature [193], have shown that impurities, consistent with what was found in our IR spectroscopic measurements, occur in emulsion polymerization processes, and consist of low molecular weight polymers that form during the process and remain water soluble. During the assembly process, these impurities will be co-deposited by capillary forces at the contact points between the colloidal particles and at the substrate/particle contact. Along these lines, we note that the colloidal suspension for Sample 2 was centrifuged three times, while the suspension for Sample 1 was only centrifuged once, as can be seen in the Appendix C. The average interlayer stiffness calculated from measurements on all regions of Sample 2 is 0.68 kN m^{-1}.

The red and blue dashed lines in Fig. 4.3(b) indicate the resulting fundamental eigenfre-

quencies of coupled oscillator systems with two to twelve masses connected to each other via contact springs having stiffness equal to the measured average interlayer stiffness Ge, avg and to the substrate via a contact spring of stiffness equal to the measured particle–substrate contact stiffness K_N for Sample 1 and 2, respectively. We find that the measured frequencies follow the trend predicted by the coupled oscillator model, including in the case of the samples where a monolayer resonance was not detected.

We find considerable disparity between the monolayer contact resonance frequency measurements for the two colloidal crystal samples ($\sim$ 1 GHz) and that for the monolayer fabricated by the pre-assembly at the air/water interface (520 MHz). Table 1 lists the average effective interlayer stiffness and the particle–substrate contact stiffness calculated from the measured frequencies for the two multilayer samples and the air/water monolayer sample. Potential causes for this disparity, as well as comparisons with adhesive contact models will be discussed in the following.

We compare the average effective interlayer stiffness and the particle–substrate contact stiffness obtained from our measurements to estimates made using the Derjaguin–Muller–Toporov (DMT) adhesive elastic contact model [138]. The DMT adhesive elastic contact model is derived from the Hertz contact model [75], with the addition of a static adhesive force. Based on the DMT model contact mechanics, the linearized normal contact stiffness around the equilibrium displacement is expressed as $K_{DMT} = \frac{3}{2}(2\pi w {R_e}^2 {E^*}^2)^{3/2}$ [77], where w is the work of adhesion between the two surfaces in contact [121], R_e is the effective radius (equal to the radius of the sphere for the particle–substrate contact, and half the radius of the sphere for the particle–particle contact) and $E^* = [(3/4)((1-\nu_P^2)/E_P + (1-\nu_S^2)/E_S)]^{-1}$ is the effective modulus of the contact. Using a work of adhesion between the polystyrene spheres and the silica coated substrate obtained using the Lifshitz theory of van der Waals forces [121] of $w_{P-S} = 0.06$ J m^{-2}, and $\nu_P = 0.32$, $\nu_S = 0.17$, $E_P = 4.04$ GPa and $E_S = 73$ GPa as the Poisson's ratio and Young's modulus of the polystyrene sphere [139] and the substrate [161], respectively, we estimate the linearized normal contact stiffness between the

Table 4.1: Measured and predicted (using the Derjaguin–Muller– Toporov, or "DMT" adhesive elastic contact model) particle–substrate and average interlayer contact stiffness. The DMT model assumes $w_{P-S} = 0.06$ J m $^{-2}$ and $w_{P-P} = 0.06$ J m $^{-2}$

	K_N (kN m $^{-1}$)	$G_{e,avg}$ (kN m $^{-1}$)
Sample 1	1.3	0.4
Sample 2	1.6	0.7
Air/water monolayer	0.4	-
DMT model	0.1	0.1

particle and the substrate to be $K_{N,DMT} = 0.1$ kN m^{-1}. Similarly, we find $G_{e,DMT} = 0.1$ kN m^{-1}, using a work of adhesion between the spheres of $w_{P-P} = 0.06$ J m^{-1} (see Appendix C).

From Table 4.1, we observe that the particle–substrate and the effective interlayer stiffnesses predicted by the DMT model are much lower than all the corresponding measured contact stiffnesses. The discrepancy between measured contact stiffnesses and those predicted by the DMT model has been reported previously for silica [77, 119] as well as polystyrene microspheres [139, 160], and could be explained by the uncertainty in the work of adhesion between contacting surfaces [121], plastic deformation [194], or solid [195] or liquid [122, 140, 176] material bridges around the contacts.

To gain insight into the source of the difference between the measured contact stiffnesses of the multilayer samples and the air/water monolayer sample, as well as that between the measurements and DMT model prediction, we analyze the contact surface by means of scanning electron microscopy. Representative side-view SEM images of the particle–substrate contacts in the air/water monolayer sample, and the monolayer regions of the two multilayer colloidal crystal samples investigated in Fig. 4.2(a) (i.e., Sample 1 and Sample 2) are shown in Fig. 4.4(a)–(c). The SEM image of the air/water monolayer sample, shown in Fig. 4.4(a), indicates a large particle–substrate contact diameter (of $\sim$ 50 nm), which is

significantly higher than that predicted by the DMT model (28 nm). The large contact diameter in the air/water monolayer sample suggests that the spheres may have plastically deformed under the action of adhesive forces during the self-assembly process [194]. The SEM image of the monolayer region of Sample 1, shown in Fig. 4.4(b), reveals a similar particle–substrate contact diameter as in the air/water monolayer sample. Although the particle– substrate contact diameters in the air/water monolayer sample and Sample 1 appear to be comparable, the particle– substrate contact stiffness measured in Sample 1 being over three times that measured in the air/water monolayer sample suggests that there may be other mechanisms responsible for the added stiffness of the contacts. Side-view SEM images of the particle–substrate contacts in the monolayer region of Sample 2, shown in Fig. 4.4(c), appear considerably different from the previous two cases. The spheres seem to be partially embedded in a solid matrix that forms a 'well'-like structure around the particle. The well-like structures appear to be formed from a thin film on the substrate. However, although the particle–substrate contacts in Samples 1 and 2 appear qualitatively different, the contact stiffnesses measured on these samples were comparable.

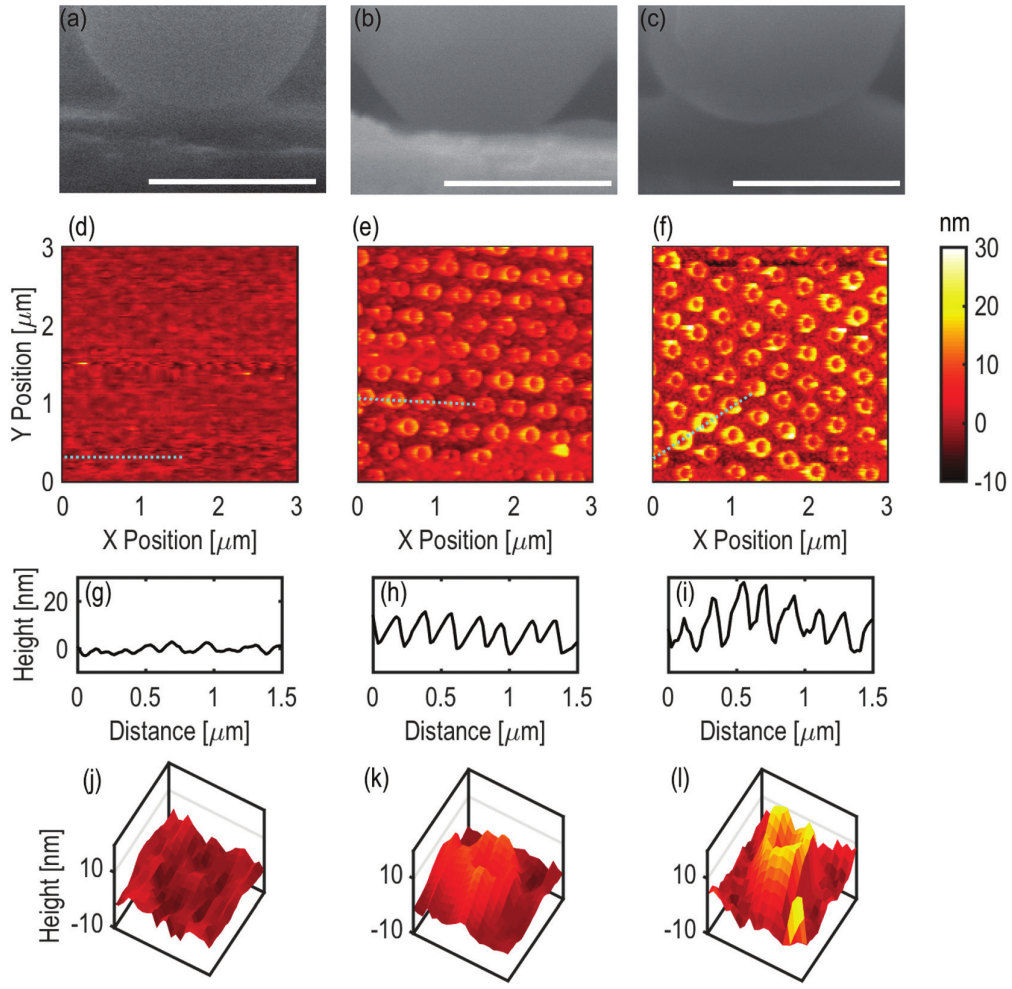

Figure 4.4: Scanning electron microscopy images of the monolayer regions in: (a) the air/water monolayer sample; (b) Sample 1; and (c) Sample 2. We note some minor lateral image distortion in the SEM image in panel (c). Scale bars represent 250 nm in all panels; however, significant uncertainty should be assumed due to variations in the distance between the focal plane and the contact. (d)–(f) Tapping-mode Atomic Force Microscopy images of the substrate after removal of the spheres. (g)–(i) Surface topology of the substrate along the dashed line shown in the corresponding panel directly above. (j)–(l) Isometric views of the AFM images of single 'well'-like features on a 0.4μm x 0.4μm area of the substrate. All panels in the same column correspond to the same sample.

To further explore potential causes for the differing contact stiffnesses, we investigate the topography of the surface of the substrate after removal of the spheres by tapping-mode AFM. The spheres in the monolayer regions were removed by placing a piece of adhesive tape on the monolayer region, followed by gentle application of pressure on the surface of the tape. The spheres adhered to the tape when it was peeled off, leaving a region of blank substrate on the sample. The AFM images of the regions of the substrate where the monolayer was peeled off on the three samples are shown in Fig. 4.4(d)–(f). For the case of the air/water monolayer sample, the AFM image in Fig. 4.4(d) shows variations in the surface height within $\sim$ 3 nm, which we attribute, in part, to the roughness of the silica film deposited on the substrate. However, the AFM image also reveals ring-like patterns of diameter $\sim 150 - 200$ nm at the sites previously occupied by the spheres, suggesting that these patterns could be due to residue on the surface. The corresponding AFM images of the multilayer colloidal crystal samples show a similar, but more pronounced, substrate surface topography. The AFM image of the substrate in Sample 1, shown in Fig. 4.4(e), shows very pronounced ring-like structures, $\sim 5 - 16$ nm in height, with hemispherical openings. Even more pronounced ring-like structures exceeding 20 nm in height are seen in the AFM image of Sample 2, which is illustrated in Fig. 4.4(f), and complements the relatively larger observed contact stiffness. The diameter of the hemispherical openings of the ring-like structures in Samples 1 and 2 is $\sim 160 - 200$ nm, similar to that of the ring-like structures observed on the air/water monolayer sample. Representative profiles of the surface height in the three samples are plotted in Fig. 4.4(g)–(h). Isometric close-up views of the ring-like structures revealed by the AFM images are shown in Fig. 4.4(j)–(l). A clear meniscus shape of solid material around a central depletion caused by the removed sphere is seen.

The SEM and AFM images of the regions around the particle– substrate contacts in the colloidal crystals compliment the contact stiffnesses obtained from the laser ultrasonic measurements, and provide possible explanations for the discrepancies in the particle–substrate contact stiffness between the air/water monolayer and multilayer samples, as well as discrep-

ancies between our measurements and predictions made by the DMT contact model. For instance, the ratio of the contact stiffness between the air/water and Sample 2 monolayers was measured to be 3.3, as is shown in Table 4.1. The difference in contact stiffness can be estimated by comparing the vertical particle deformation distance d_1 with the height of the added impurity d_2 material such that $K_2/K_1 = \sqrt{(1 + d_2/d_1)}$. Using a particle deformation distance of $d_1 = 3$ nm, calculated from the measured contact resonance frequency of the monolayer, and assuming an impurity well height of $d_2 = 20$ nm, we obtain a ratio of contact stiffness $K_2/K_1 = 2.7$, which is close to the measured difference.

The previously described bridging can also be observed in the interparticle and particle-substrate contacts in the multilayer regions of the colloidal crystal samples. Representative views of the particle–substrate and interparticle contacts in the multilayer regions of Samples 1 and 2 are illustrated in Fig. 4.5(a) and (b), respectively. For both samples, a thin 'bridging' material ($\sim$ 10 nm in width) is seen in the region around the particle–substrate contact, as well as in the interstitial space between neighboring spheres. As before, the 'bridging' material is more evident in Sample 2 (shown in Fig. 4.5(b)), which can be seen as a continuous thin film along the substrate that forms well-like structures around the particle–substrate contact. Similar to the case of the monolayer regions, the material is also deposited at the contact points between neighboring spheres. We attribute these solid bridges to the presence of solid impurities within the colloidal suspension.

The differences between the various samples in this study, as seen from measurements of the contact stiffnesses via laser ultrasonic characterization as well as in the SEM and AFM images of the contacts, can be attributed to the different nature of the self-assembly fabrication process. In the modified Langmuir–Blodgett technique, a floating monolayer of spheres is pre-assembled at an air/water interface, which is then transferred onto a substrate [157]. Solid impurities in the colloidal suspension, such as water-soluble polystyrene oligomers, other reaction side-products from the emulsion polymerization process [188], or polymer impurities that may leach from the vials containing the colloidal solution, are much more diluted as

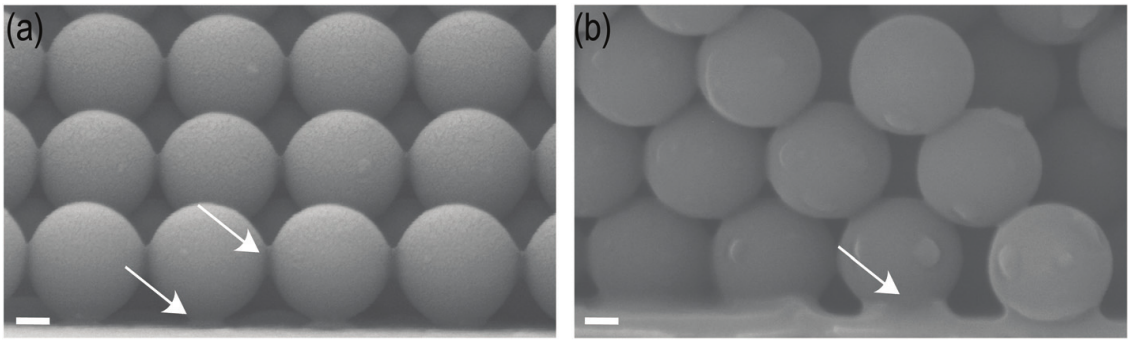

Figure 4.5: Scanning electron microscopy images illustrating particle–substrate and inter-particle contacts in (a) a seven-layer-thick region of Sample 1 and (b) a six-layer-thick region of Sample 2. The scale bar is 100 nm in both panels. The arrows indicate representative material bridges observed between the contacts.

the water subphase provides an enormous reservoir. This may explain the smaller ring-like structures seen in the AFM images of the air/water monolayer sample, Fig. 4.4(d). On the other hand, the 'bridging' material seen between the sphere contacts in Samples 1 and 2 may be formed by solid impurities occupying interstitial sites in the crystal lattice. Unlike the case of the air/water pre-assembly technique, it is possible that the solid impurities in the vertical deposition technique are pulled towards spheres that have already deposited on the substrate by convective forces. Subsequently, these impurities are concentrated in liquid capillary bridges that form between the spheres and the substrate, where they finally solidify upon drying. As a result, the purity of the assembly suspension (i.e., the amount of impurities) will determine the quality of the colloidal crystal sample, which in turn would be expected to affect the contact properties, wherein cleaner suspensions should give less solid bridges and suspensions with more solid impurities should result in colloidal crystals with more solid bridges. As suggested earlier, multiple cycles of centrifuging the colloidal suspension and removing the supernatant prior to self-assembly deposition can alter the quantity of impurities in the colloidal suspension. The use of repeated centrifuge purification steps in

the preparation of Sample 1 readily explains the slightly higher particle–substrate contact stiffness in Sample 2 over Sample 1, and the thicker film on the surface of the substrate. In addition to affecting the average interlayer contact stiffness of the multilayer, an increased density of impurities at the lower layers may also contribute to the observed decrease in stiffness with increasing layer thickness shown in Fig. 4.3(b2). Our measurements, therefore, open avenues to potentially assess the packing and contact quality in three-dimensional colloidal crystals.

For further insights into the mechanical wave propagation properties in our colloidal crystals, we estimate the long wavelength longitudinal sound speed v in the colloidal crystal samples from the measured average interlayer contact stiffnesses using the relation $v = \sqrt{\frac{G_{e,avg}}{m}} D^*$, where $D^* = \frac{\sqrt{6}}{3} D$ is the unit cell spacing, and find $v_1 = 1166$ m s^{-1} and $v_2 = 1445$ m s^{-1} for Samples 1 and 2, respectively. Our estimated values are about half the longitudinal sound speed in bulk polystyrene, $v_{PS} = 2350$ m s^{-1} [139], and about two times higher than the sound speed calculated using the interlayer contact stiffness predicted by the DMT model, $v_{DMT} = 617$ m s^{-1}. We also calculate the long wavelength sound speed obtained from the observed contact diameter, assuming DMT contact mechanics. Using a contact diameter of 150 nm yields a sound speed of 1582 m s^{-1}, which is in reasonable agreement with the sound speed calculated from the measured average interlayer stiffness. At the macroscale, an uncompressed granular crystal is often described as a sonic vacuum (i.e., zero sound speed) wherein the particle–particle interactions are purely nonlinear [76]. As this system is compressed, it becomes more linear, with a finite low-amplitude sound speed. Compared to sound speeds as low as ~ 200 m s^{-1} measured in slightly compressed macroscale granular crystals [102], the relatively high speeds in our samples suggest a highly linearized system. Strategies to increase the coupling between macroscale spheres in contact and therefore modify their dynamic response have been studied previously, for instance by welding a finite chain of millimeter-sized steel spheres [196], where the contact diameter was $\sim 30\%$ of the sphere diameter. Controlling the size of the material bridges between the spheres may

therefore be used as an analogous mechanism to tune the coupling between particles at the micro- and nanoscale.

Finally, we compare the quality factors of the peaks of the measured eigenfrequencies to those estimated from the acoustic impedance mismatch between the colloidal crystal and the glass substrate. We estimate the acoustic impedance of the colloidal crystal to be $Z_1 = \rho_c v_1 = 0.92$ MPa s m^{-1}, where v_1 is the longitudinal sound speed calculated previously for Sample 1 using the average interlayer contact stiffness and effective density of the colloidal crystal of $\rho_c = \frac{6\phi m}{\pi D^3} = 784$ kg m^{-3}, which is calculated using a solid volume fraction $\phi = 0.74$ assuming HCP packing. Similarly, we calculate the acoustic impedance of the glass substrate to be $Z_s = \rho_s v_s = 14.2$ MPa s m^{-1}, where $\rho_s = 2500$ kg m^{-3} is the density of the substrate and $v_s = 5697$ m s^{-1} is its sound speed [197]. The resulting amplitude reflection coefficient r at the colloidal crystal/substrate interface is calculated to be $r = \frac{Z_s - Z_l}{Z_s + Z_l} = 0.88$ We estimate the expected quality factor of the fundamental mode, accounting for radiation from the colloidal layer, using the relation $Q_i = \frac{\pi(2i-1)}{1-r^2}$. For the fundamental mode ($i = 1$), we estimate a quality factor of $Q_1 = 14$, which is slightly larger than the observed quality factor for the fundamental mode of the 12 layer thick region of Sample 1, and respectively larger than the other measured fundamental modes. Furthermore, for the 12 layer thick region of Sample 1, the measured quality factors of the higher-order peaks vary between $\sim 7 - 10$, which is in contrast to the increase in quality factor with mode number that is expected for damping stemming from radiation into the substrate. The observed quality factors for the higher-order, shorter-wavelength modes thus suggest additional susceptibility to material or disorder-related loss mechanisms, including mechanisms arising from disorder in the contact stiffnesses.

4.4 Conclusions

In summary, we have studied the contact-based longitudinal eigenvibrations of ordered, three-dimensional colloidal crystals adhered to solid substrates. We identify regions of uniform

layer thickness in the colloidal crystal by their structural color. This enables us to measure the longitudinal eigenvibrations of the colloidal crystal as a function of layer thickness. Using non-contact laser ultrasonic measurements, along with a coupled oscillator model, we extract the particle–substrate and effective interlayer contact stiffness in the samples, and in one case find the effective contact stiffness between each layer to decrease with increasing number of layers. The laser ultrasonic measurements, supplemented by SEM and AFM images, show that nanometric-sized bridges around the contacts can drastically affect the contact stiffnesses. In the future, we expect that the rational control of contact stiffness via deposition of solid bridges can be systematically exploited to tailor the acoustic properties of self-assembled structures, which may in turn lead to a new class of tunable "micro- and nanoscale granular crystals". For instance, the intentional inclusion of additional short-chain polymers in the solution could tune the contact stiffness by at least four times, as was shown in this study (comparing the contact stiffness obtained using the Langmuir–Blodgett technique to the one using vertical deposition). This study furthers the understanding of the dynamics of self-assembled micro- and nanoparticulate structures, which may have potential for ultrasonic wave tailoring applications analogous to macroscale granular crystals.

4.5 Collaborator Contributions

Several collaborators contributed to the work presented in this chapter. The project grew out of an observation by M. Abi Ghanem of eigenmodes of a three-dimensional granular crystal the author of this thesis had fabricated and was investigating for other purposes. The author of this thesis provided guidance on sample fabrication and discussions and analysis of the experimental results. The laser ultrasonic measurements and data analysis were performed by M. Abi Ghanem and A. Khanolkar. Development of the coupled oscillator model and contact stiffness calculations were performed by S. Wallen. The samples used in this chapter were fabricated by M. Helwig and A. Khanolkar. Sample visualization via SEM and AFM were performed by A. Khanolkar. A. Maznev gave guidance on the analytical analysis of acoustic radiation.

Chapter 5

ACOUSTIC WAVE PROPAGATION IN DISORDERED MICROSCALE GRANULAR MEDIA UNDER COMPRESSION[1]

We investigate the effect of dynamic and uniaxial static loading on the wave speeds and rise times of laser generated acoustic waves traveling through a disordered, multilayer aggregate of 2μm diameter silica microspheres, where the excited dynamic amplitudes are estimated to approach the level of the static overlap between the particles caused by adhesion and externally applied loads. Two cases are studied: a case where the as-fabricated particle network is retained, and a case where the static load has been increased to the point where the aggregate collapses and a rearrangement of the particle network occurs.We observe increases in wave speeds with static loading significantly lower than, and in approximate agreement with, predictions from models based on Hertzian contact mechanics for the pre- and post-collapse states, respectively. The measured rise time of the leading pulse is found to decrease with increasing static load in both cases, which we attribute to decreased scattering and stiffening of the contact network. Finally, we observe an increase in wave speed with increased excitation amplitude that depends on static loading, and whether the system is in the pre- or postcollapse state. The wave speed dependence on amplitude and static load is found to be in qualitative agreement with a one dimensional discrete model of adhesive spheres, although the observed difference between pre- and post-collapse states is not captured. This investigation, and the approach presented herein, may find use in future studies of the contact

[1]Included in this chapter is material from Ref. [198]. Reprinted with permission from M. Hiraiwa: Springer, *Granular Matter*, "Acoustic wave propagation in disordered microscale granular media under compression," M. Hiraiwa, S. P. Wallen, and N. Boechler, Copyright 2017.

mechanics and dynamics of adhesive microgranular systems.

5.1 Introduction

The velocities of acoustic waves in granular media are known to be highly dependent on applied static and dynamic loads, due to factors including the configuration of the internal microstructure and the nonlinear mechanics of particles in contact [52]. This dependence has had implications for applied areas, such as geological exploration and analysis [199], and proven useful for studying the effective constitutive properties of granular media [52, 101–104, 106–108, 200–205]. The effect of applied static and dynamic loading on acoustic wave propagation has been explored in many experimental studies of granular materials that have particles with diameters ranging from tens of microns to several millimeters [52, 66, 70, 101–104, 106, 107, 128, 200, 203, 205]. This includes studies of assemblies of uniform spherical particles [52, 66, 70, 101–104, 106, 107, 128, 203, 205], wherein highly nonlinear phenomena that stem from the Hertzian mechanics [75] of spherical particles in contact, such as sonic vacua and solitary wave propagation [52, 66, 70], have been demonstrated.

The dynamics of granular media having particles with diameters of a few microns and below are of fundamental interest, as they involve physical phenomena distinct from their macroscale counterparts. For instance, while interparticle adhesion [121] may be neglected for systems of macroscale particles, it can play a major role in the dynamics of systems of microscale particles, as has been demonstrated in several recent studies of two-dimensional microscale granular crystals [77, 119, 130]. In microgranular systems, adhesive forces induce large deformations at the particle contacts, which can effectively linearize the dynamical response [52], induce plasticity near the contact [88], and increase the role of shear interactions [119].

In this work, we investigate the dependence of acoustic wave speeds and pulse rise times on applied dynamic and uniaxial static loading for a disordered, multilayer aggregate of 2μm diameter silica microspheres, where the excitation amplitudes are estimated to approach

the level of the adhesion- and external-load-induced static overlap between the particles. The wave speed is determined from the time of flight of a laser generated acoustic pulse traveling through the multilayer. Two cases are considered: a "pre-collapse" case, in which the as-fabricated particle network is mostly retained, and a "post-collapse" case, where the particle network has rearranged after the applied static compressive stress was increased to a point where the multilayer collapses. We find that these two cases exhibit distinct behaviors. In the post-collapse case, we see a power law dependence of the sound speed c on the static load F of approximately $c \propto F^{1/6}$, consistent with previous experimental studies [101–104, 107, 205] on granular assemblies, theoretical models [101, 201, 202] based on Hertzian contact mechanics, and studies of the contact- and breathing-mode dynamics of isolated sub-micron spheres [118]. In the pre-collapse case, we find an anomalous dependence of sound speed on static load (where the sound speed increases much less than predicted by Hertz theory). Deviation from the Hertzian 1/6 power law dependence has been observed experimentally in systems consisting of spheres with diameters of a few hundred microns or greater [101, 103, 106, 107] and also predicted theoretically [202, 204]. However, in contrast to our work, these studies found a power law dependence with an exponent greater than the Hertzian prediction (e.g. 1/4) and, in many cases, the exponent was found to be static load dependent, wherein the exponent transitioned from 1/4 to 1/6 as static load increased [101, 103, 107, 202, 204]. In addition to the wave speed dependence on static load, we observe that the rise time of the first-arriving acoustic pulse decreases with increasing applied static load for both cases. Finally, we study the amplitude dependence of the wave speeds in both preand post-collapse cases. We find the amplitude dependence of wave speed depends on the level of static loading, and whether the system is in the pre- or post-collapse state. The dependence on amplitude and static load is found to be in qualitative agreement with a one-dimensional (1D), discrete element model (DEM) describing waves propagating through a compressed chain of adhesive spheres, although the observed differences between pre- and post-collapse states are not captured.

5.2 Experimental Setup

A schematic of the apparatus used for the experiments is shown in Fig. 5.1(a). The microsphere array is fabricated by depositing a suspension of microspheres into a well, which dries to form a multilayer microgranular adhesive network. The microsphere suspension consists of silica spheres, with $D = 2\mu$m diameter, in water, and has a concentration of 25 mg/mL (purchased from Corpuscular Inc.), he microsphere suspension is deposited on a 1.5 mm thick glass microscope slide coated with a 100 nm thick aluminum (Al) film (purchased from EMF Corp.), which serves as the substrate. Sections of 180μm thick glass coverslips are glued onto the Al- coated side of the substrate, such that the arrangement creates an approximately 5 mm by 5 mm square well with a depth equal to the coverslip thickness. To ensure the multilayer is thicker than the coverslip thickness, we use a solution volume greater than the volume enclosed by the coverslips, which we contain by adding a slab of 3 mm thick polydimethylsiloxane (PDMS) on top of the coverslip well that has a 5 mm by 5 mm square cut out. The microsphere solution is deposited into this well and allowed to dry overnight, after which the PDMS slab is removed. A scanning electron microscope (SEM) image of the surface of the depositedmultilayer is shown in Fig. 5.1(b). Once dried, the multilayer protrudes past the coverslips and has a slightly curved surface. To create a nominally flat surface for the compression experiments, the top of the multilayer is removed by sliding a razor blade along the coverslips, which results in a multilayer with a thickness of 180μm, as is shown in the SEM images of Fig. 5.2(a,b). We note that the images in Fig. 5.2(a,b) are likely not representative of the morphology throughout the thickness of the sample, as modification with the razor blade primarily affects a region localized near the surface.

To apply a specified static load F_0 to the microspheres, we designed and used the compression setup shown in Fig. 1a. The substrate and microsphere-filled well are attached to a fixed metal bracket. Opposite from the sample, a load cell washer with a hole through the center (model LW1020-5, Interface Load Cells) is used to monitor the applied load, and is mounted on a spring loaded, motorized translation stage. A 1.5 mm glass slide coated with 100 nm of

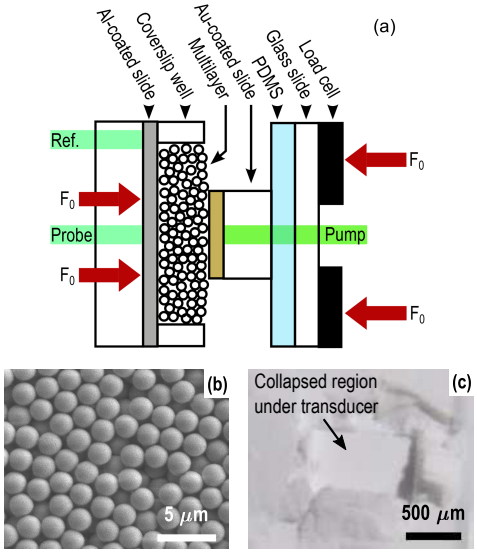

Figure 5.1: [Color online] Overview of the experiment. (a) Schematic of the compression setup. (b) SEM image of the as-deposited multilayer surface, prior to modification with the razor blade and application of compression. (c) Photograph of a post-collapse multilayer, taken at a 45° angle

gold (Au) purchased from EMFCorp. is cut into a 1 mm by 1 mm square using a diamond saw, and mounted on the load cell with a 2 mm thick PDMS slab and clear glass slide sandwiched in between. The role of the PDMS slab is to compensate for relative tilt between the Au-coated slide and multilayer sample, as shown in Appendix D.

Acoustic pulse generation is accomplished by irradiating the Au film, which we will refer to as the 'transducer,' with pulsed laser light (532 nm wavelength, 0.5 ns pulse duration, 1 kHz rep rate, 400 μm spot size at $1/e^2$ intensity level). For 'high' and 'low' amplitude excitations, we use pulse energies of 13 and 3.7 μJ per pulse, respectively. Rapid thermal expansion induced by the absorption of the laser light launches a short duration acoustic pulse that travels through the thickness of the multilayer. Acoustic pulses are detected with a grating interferometer [136], which reflects both probe and reference beams off the same sample to aid

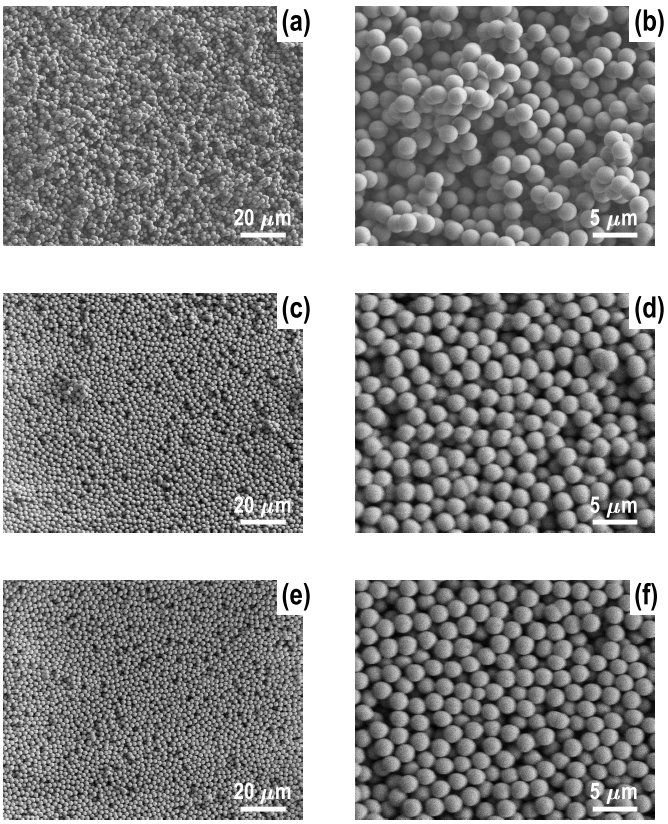

Figure 5.2: SEM images of the multilayer surface in various states. (a,b) After having a razor blade slid across the coverslip well. Pre- (c, d) and Post-collapse (e, f) states after having the applied load cycled multiple times. Panels (b, d, f) are magnified versions of (a, c, e), respectively

stability. For the grating interferometer, we use a continuous wave laser (514 nm wavelength and 21 mW power for each of the probe and reference beams). Both the probe and reference beams are focused on the Al film to a spot size of 240 μm (at $1/e^2$ intensity level), with the probe positioned so that it is axially aligned with the pump beam. The reference beam is separated from the probe beam by 5 mm, and is focused onto a stationary region of the sample. Interferometric signals are detected with a silicon photodetector (ET-2030A, Electro-Optics Technology Inc., 2 GHz bandwidth), recorded with a digital oscilloscope (2.5

GHz bandwidth), and then averaged over 10^4 trials. Changes in multilayer thickness during compression are measured using a laser distance sensor (model IL-030, Keyence Inc.), that has 1 μm resolution.

5.3 Experimental Procedure

The steps in the experimental procedure are outlined in Fig. 5.3. A tabulated list of all experiments conducted is listed in Appendix D.1. We initially condition the sample by cycling the applied compression between approximate 'minimum' and 'maximum' conditioning loads while monitoring the The minimum conditioning load is set to 0.25 N for all experiments, while the maximum conditioning load ranges from F_C = 2.0 to 3.1 N. The loading cycle is repeated until the arrival time of the acoustic pulse converges to a steady value. After the conditioning procedure is complete, we record acoustic measurements at various applied static loads, from the minimum static load F_{min} = 0.25 N to the maximum measurement static load F_{max} (which varies as shown in Appendix D.1). First, at F_{min}, we measure acoustic signals at the high- and low-excitation amplitudes, in that order. Next, acoustic signals are measured at incrementally increasing static loads using only the high excitation amplitude. Once F_{max} is reached, we again measure acoustic signals at the high- and low-excitation amplitudes. To demonstrate repeatability, this process is repeated three times for one experiment (denoted as Experiment #4 in Appendix D.1). After obtaining acoustic signals, changes in the multilayer thickness are measured using the laser distance sensor by recording displacements at incrementally increasing static load, from F_{min} to F_0 = 2.0 N. This displacement measurement process is repeated a total of three times for each experiment. To minimize potential effects of the compression fixture tilting, the sensor is focused onto a piece of cardboard spanning the hole in the load cell washer, such that it is aligned with the axis of the pump. We subtract measurements performed on a bare substrate from those performed on the multilayer sample to remove the displacement due to movement of the fixture, mostly caused by compression of the 2 mm thick PDMS slab sandwiched between the Au-coated transducer and the glass slide. We find a standard deviation of the sample

displacements measured at a static load of $F_0 = 2.0$ N to be 4 μm (no consistent trend in the displacement variation was observed between repeated loading cycles), which we consider the upper limit of possible changes in multilayer thickness at this load.

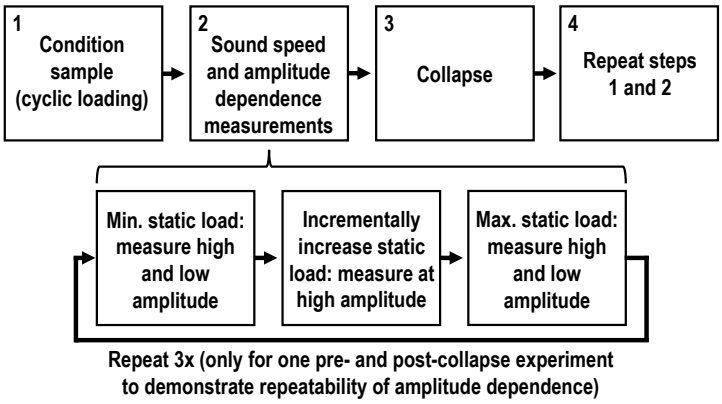

Figure 5.3: Outline of experimental procedure

After the experiments are performed on the as-fabricated multilayer, we increase the static load until the multilayer buckles underneath the transducer. This involves large-scale structural rearrangement, where microspheres flow past the sides of the transducer, resulting in a decreased multilayer thickness under the transducer and an increased multilayer thickness in the immediately surrounding regions, as can be seen in Fig. 5.1(c). The buckling process occurs rapidly and typically at static loads in the range of 3 to 6 N. After the collapse, we further increase the load to 6.4 N to induce rearrangement and improve the uniformity of contact between the multilayer and transducer. During the buckling and re-arrangement process, the laser distance sensor is focused on the side of the fixture, so that we can simultaneously monitor acoustic signals and changes in multilayer thickness, which we estimate to have been reduced from the original value of 180 μm to thicknesses ranging from 36 to 56 μm, as is detailed in Appendix D.1. We note that our method for determining the post-collapse multilayer thickness is approximate, as the measurements do not account for uneven sample thickness and transducer tilt. The cyclic loading, acoustic measurements at incremental

static loads, amplitude dependence experiments, and laser distance measurements are then performed in the same manner as the pre-collapse case, with the exception that the maximum conditioning load $F_C = 6.4$ N for all post-collapse experiments. After completing the acoustic measurements, the load is removed. We note that the region of granular material under the transducer typically disintegrates upon removal of the applied load. A photograph of a sample for which this region did not disintegrate, and the square collapsed region can be seen, is shown in Fig. 5.1(c). Scanning electron microscope images of the multilayer surface after having the load cycled with the transducer in the pre- and post-collapse states are shown in Fig. 5.2(c-f).

5.4 Experimental Results: Dependence on Static Load

5.4.1 Pre-Collapse Case

Representative acoustic signals measured for the pre-collapse case are shown in Fig. 5.4. Each of the measured signals S is normalized to the maximum amplitude of that signal S_0. Time $t = 0$ corresponds to the generation of the acoustic pulse at the Au-coated transducer surface. Figure 5.4(a) shows a signal recorded at the minimum static load. We define a normalized static load $F_R = (F_0/N + F_{adh})/F_{adh}$, where F_0 is the applied force, $N = A_T/(\frac{1}{2}\sqrt{3}D^2)$ is the number of spheres that cover the Au-coated transducer area A_T assuming hexagonal-close-packing, $F_{adh} = 2\pi wR = 0.20$ μN is the adhesive force between the silica microspheres estimated using Derjaguin-Muller-Toporov (DMT) contact mechanics [138, 162], $w = 0.063$ J/m^2 is the work of adhesion between silica particles [119], and R is the Hertzian effective radius of contact (equal to half the microsphere radius for the case of two identical spheres in contact). For the case of Fig. 5.4(a), this results in a normalized minimum static load of FR = 5.3. The arrival time of the leading acoustic pulse, which we term the '1L pulse,' at the Al-coated substrate is identified as the point when the normalized signal amplitude first reaches 0.1, and is denoted by the vertical solid line. The 1L pulse has a rise time of approximately 33 ns, which we measure as the elapsed time between normalized signal

thresholds of 0.1 and 0.9. Using a granular multilayer thickness of 180 μm and the measured transit time, we calculate a sound speed of 900 m/s. The calculated sound speed at the minimum static load for each of the samples tested is listed in Appendix D.1. We observe that the large initial pulse is followed by a second large pulse of approximately half the amplitude of the first. This second pulse is followed, and sometimes preceded, by additional small oscillations. As can be seen by the alignment with the vertical dashed lines in Fig. 5.4, this second pulse, which we term the '3L pulse,' has a transit time close to what we would expect for reflections traveling through the multilayer and reflecting between the two metal-coated glass slides. Previous studies on acoustic wave propagation in compressed granular media have also observed the phenomenon of a primary pulse followed by smaller subsequent oscillations, which were attributed to disorder-induced scattering [203]. Figure 5.4(b) shows the data from Fig. 5.4(a), superimposed with a signal measured on the same sample during the same load cycle (red curve), but at $F_0 = 2.0$ N (corresponding to a normalized force of $F_R = 36$). We observe a faster arrival time, an increased sound speed of 1020 m/s, and a shortened rise time of 24 ns.

The dependence of sound speed on static load, corresponding to the part of the loading cycle where the static load is increased, for four different spots located on two different samples is shown in Fig. 5.5. We show measured normalized sound speeds for a range of applied static load ranging from $F_{min} = 0.25$ N to $F_0 = 2.0$ N, which encompasses all four data sets. The sound speeds C_L are normalized to the speed $C_{L,min}$ measured at the minimum applied static load F_{min}. We estimate the error in the applied static load to be $F_R = 0.44$, which is obtained by summing the smallest resolvable load cell output and the difference between a load cell measurement and a known reference weight. As can be seen in Fig. 5.5, there are three experiments in close agreement and one that appears as an outlier. We fit the four experiments with a power law relationship, and find the exponent to be $\beta = 0.06$. This exponent is significantly smaller than the 1/6 ($\approx .17$) exponent predicted by models based on Hertzian contact mechanics. Additional measurements were performed

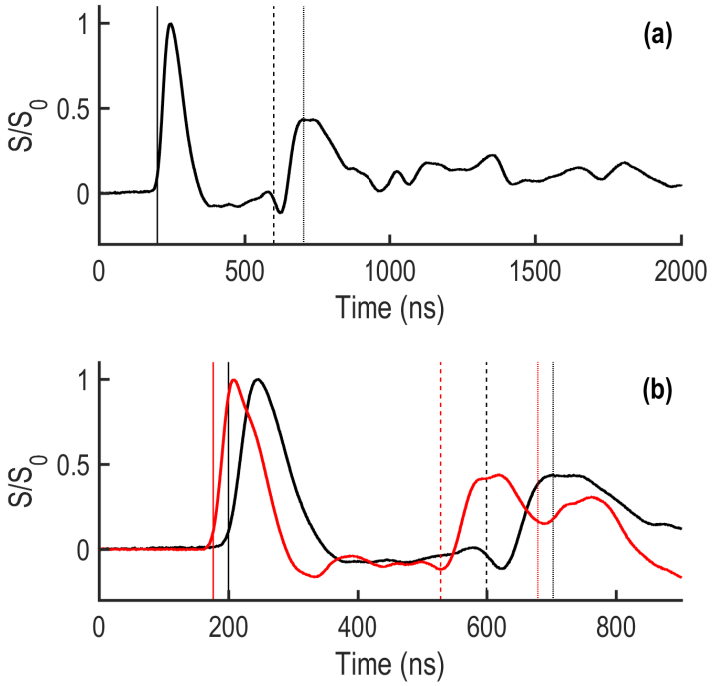

Figure 5.4: [Color online] (a,b) Representative measured signals for the pre-collapse case using the low amplitude excitation. Black and red curves correspond to static loads of F_{min} ($F_R = 5.3$) and $F_0 = 2.0$ N ($F_R = 36$). Vertical solid and dashed lines denote the arrival times of the 1L and 3L pulses, respectively, for curves of the same color. Vertical dotted lines are the time of first pulse arrival, plus the estimated round trip travel time for acoustic pulses traveling in the glass substrates. (a) Extended time window for the signal measured at static load F_{min}. (b) Shortened time window, comparing the signals measured at static loads of F_{min} and $F_0 = 2.0$ N.

by focusing the pump and probe beams at different locations across the transducer, as described in Appendix D.2. Although the measured power law exponent β describing the dependence of sound speed on static load varied across the transducer, all locations resulted in an exponent significantly smaller than 0.17, with a mean value of $\bar{\beta} = 0.02$. As a reference,

we plot the static load dependence of a 270μm thick PDMS sample (Sylgard 184 Silicone Elastomer Kit mixed with a 10 : 1 base to curing agent ratio) in the place of the microsphere multilayer, using the same experimental procedure, and find minimal change in sound speed with static load, as is shown by the black triangle markers in Fig. 5.5. In contrast to the experiments on the microsphere multilayers, the PDMS sample thickness decreases by a significant amount during the application of the static load. However, as can be seen in Fig. 5.5, by accounting for the change in thickness using displacements obtained with the laser distance measurements, this results in a nearly constant sound speed.

5.4.2 Post-Collapse Case

Representative time domain signals for the post-collapse case are shown in Fig. 5.6 in the same manner as in Fig. 5.4. The signal is noticeably different from the pre-collapse case, displaying a sharp rise followed by a slow decay superimposed with echoes, and a reduced 1L arrival time. The rise time has also decreased by approximately 45%. These observations (excepting the slower decay) are consistent with expectations for a decrease in multilayer thickness, where the reduced rise time is expected as a result of the decreased length for scattering and dispersive effects to occur. An enlarged view of the data in Fig. 5.6(a) is shown in Fig. 5.6(b), superimposed with the time domain signal at $F_0 = 2.0$ N. Similar to the pre-collapse case, the measured 1L arrival time decreases when the static load is increased, and the 3L pulse arrives approximately when it is expected based on the 1L transit time. This alignment can be contrasted with the estimated arrival times corresponding to reflections within the glass substrates, which is denoted by the vertical dotted lines in Figs. 5.4 and 5.6.

The measured dependence of normalized sound speed on static load is shown in Fig. 5.7 for four different regions across two samples. The dependence of normalized sound speed versus normalized static load between the different experiments shows significantly more scatter than the pre-collapse case, with exponents ranging from $\beta = 0.11$ to 0.25. By averaging

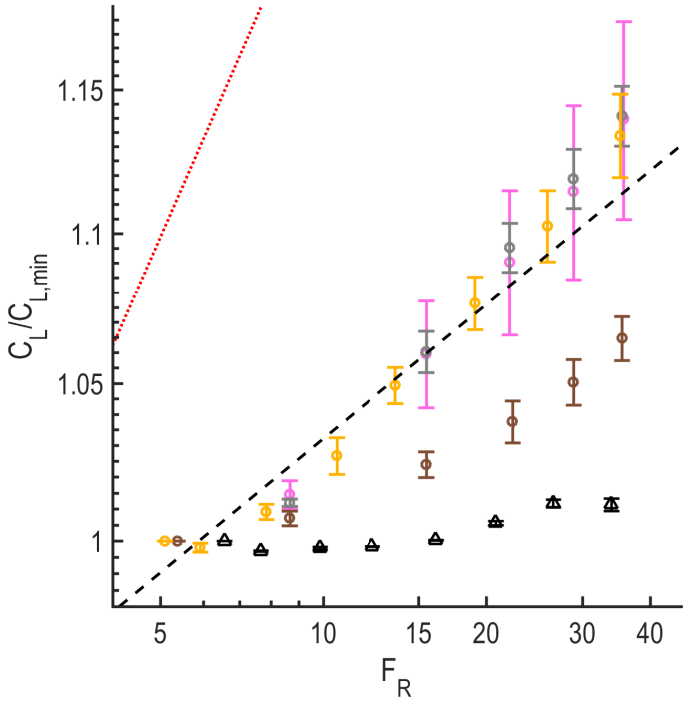

Figure 5.5: [Color online] Dependence of sound speed C_L (normalized to the sound speed $C_{L,min}$ at the static load F_{min}) on normalized static load F_R, for the pre-collapse case, plotted using a logarithmic scale on both axes. Circle markers correspond to microscale granular experiments, with the colors denoting experiments performed at different positions on two samples, as denoted in Appendix D.1. Error bars denote the difference between normalized sound speeds calculated with the thresholds of $S/S_0 = 0.1$ or 0.9 used to identify the pulse arrival time. Horizontal error is estimated to be 0.44 in terms of normalized static load. The dashed black line is fitted to the data, and has a slope of 0.06. The dotted red line has a slope of 1/6. The black triangles denote sound speeds measured for a 270μm thick PDMS sample as a function of applied static load. The yellow markers correspond to the data shown in Fig. 5.4

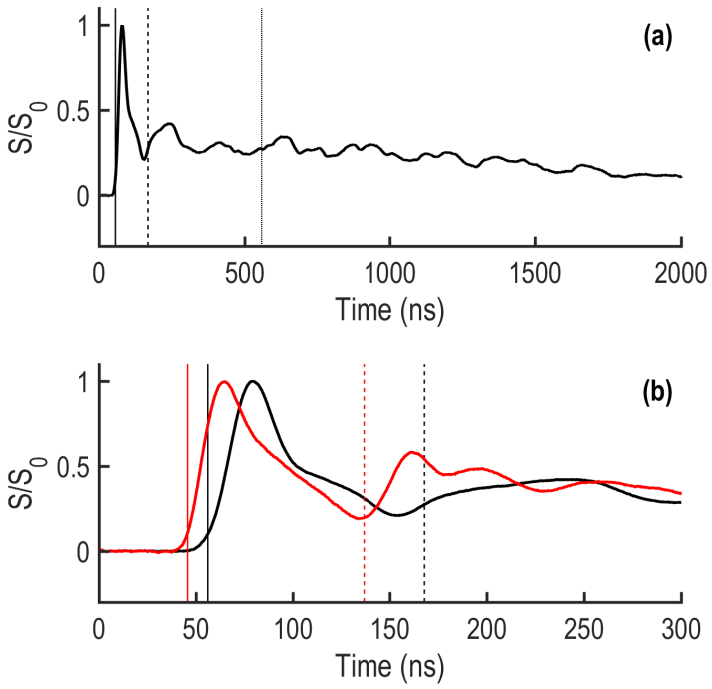

Figure 5.6: [Color online] (a,b) Representative measured signals for the post-collapse case using the low amplitude excitation. Black and red curves correspond to static loads of F_{min} ($F_R = 5.3$) and $F_0 = 2.0$ N ($F_R = 36$). Vertical solid and dashed lines denote the arrival times of the 1L and 3L pulses, respectively, for curves of the same color. The vertical dotted line is the time of first pulse arrival, plus the estimated round trip time for acoustic pulses traveling in the glass substrates. (a) Extended time window for the signal measured at F_{min}. (b) Shortened time window, comparing the signals measured at static loads of F_{min} and $F_0 = 2.0$ N

all four experiments, we find an exponent for the static load and sound speed power law relationship of $\bar{\beta} = 0.16$, which is in approximate agreement with the 1/6 exponent predicted based on Hertzian contact mechanics. Focusing the pump and probe onto different regions of the transducer revealed that the rate of increase of the sound speed with static load is

highly position dependent, as is shown in Appendix D.2. However, we observed no consistent pattern of the spatial dependence when comparing pre- and post-collapse states, likely due to the random nature in which the multilayer rearranges during the collapse.

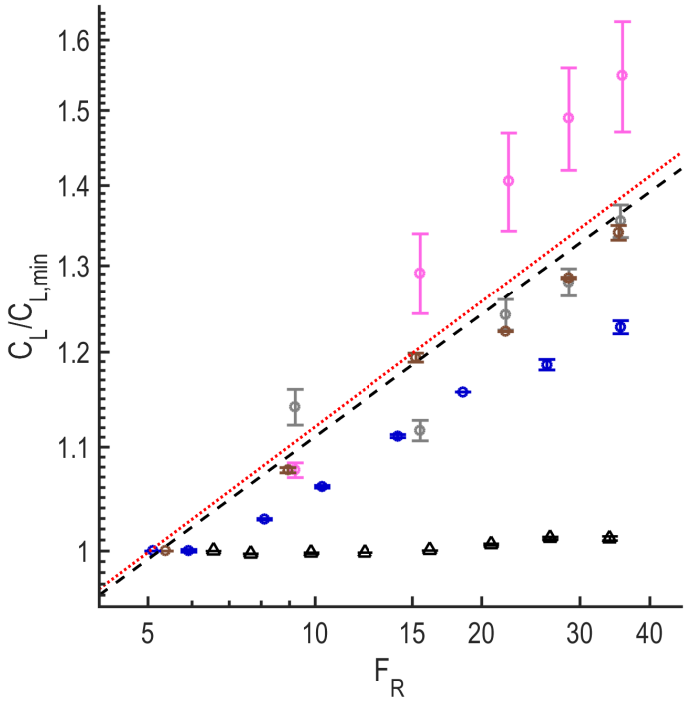

Figure 5.7: [Color online] Dependence of sound speed C_L (normalized to the sound speed $C_{L,min}$ at the static load F_{min}) on normalized static load F_R, for the post-collapse case, plotted in logarithmic scale on both axes. Circle markers correspond to microscale granular experiments, with the colors denoting experiments performed at different positions on two samples, as denoted in Appendix D.1. Error bars denote the difference between normalized sound speeds calculated with the thresholds of $S/S_0 = 0.1$ or 0.9. Horizontal error is estimated to be 0.44 in terms of normalized static load. The dashed black line is fitted to the data, and has a slope of 0.16. The dotted red line has a slope of 1/6. The black triangles denote sound speeds measured for a 270μm thick PDMS sample as a function of applied static load. The blue markers correspond to the data shown in Fig. 5.6

5.4.3 Dependence of Rise Time on Static Load

In addition to altering the sound speed, static loading may affect the shape of waves propagating through granular media by mechanisms including modification of the multilayer dispersion or scattering characteristics. We consider these effects by measuring the rise time of the 1L pulse as a function of static load. The rise times for the pre- and post-collapse cases, normalized to the rise time at F_{min}, are shown in Fig. 5.8. Each of the experiments has the same marker color as the corresponding data in Figs. 5.5 and 5.7. We find that the rise times systematically decrease with increasing static load (with the exception of the sample corresponding to the pink markers in Fig. 5.8(b)). The PDMS film also shows a decreasing rise time, although to a far lesser extent than the multilayer samples. This may be due to frequency dependent attenuation, which was found to scale as $\approx 1/f^2$ for PDMS [206]. The decreased thickness of the PDMS sample under increased loading may contribute to the retention of high frequency components of the acoustic signal, and thus a faster rise time.

5.5 Experimental Results: Dependence on Excitation Amplitude

The effective nonlinearity of compressed granular media has previously been shown to depend on the ratio of the interparticle displacements due to dynamic and static loads, such that there exist near-linear, weakly nonlinear, and strongly nonlinear dynamical regimes [52]. To study the dependence of wave speed on excitation amplitude in our granular multilayer, we excite high- and low- amplitude acoustic pulses at static loads F_{min} and F_{max}. The transducer displacements of the low- and high-amplitude excitations are estimated to be 0.51 and 1.9 nm by interferometrically measuring the free surface displacement of a separate microscope slide that is coated with 100 nm of Au, but which is not in contact with any spheres, at the same pump energies used in the experiments, as detailed in Appendix D. In comparison, effective static overlaps at F_{min} and $F_0 = 2.0$ N estimated from DMT contact mechanics are 0.95 and 3.4 nm, respectively (see Appendix D.3). The relative excitation amplitudes and static overlaps suggest weakly nonlinear dynamics, where, assuming Hertzian nonlinearity,

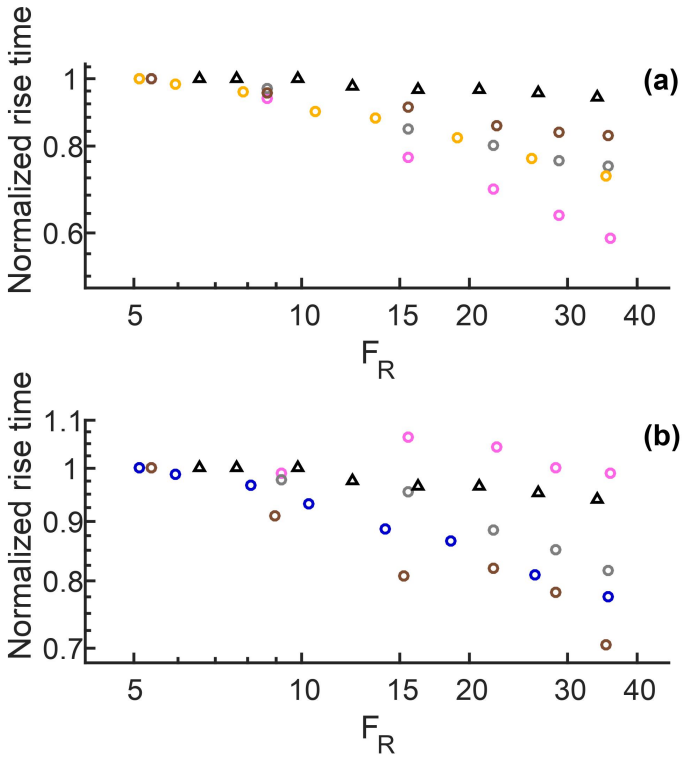

Figure 5.8: [Color online] Dependence of pulse rise time, normalized to the pulse rise time at F_{min}, on normalized static load F_R. a Pre-collapse case. (b) Post-collapse case. The black triangles denote the rise time measured for a 270μm thick PDMS sample. The markers with the same colors as in Figs. 5.5 and 5.7 correspond to the same experiment

the wave speed is expected to increase with excitation amplitude, and increase faster at lower static loads. In our experiments, the high amplitude excitation is limited by melting of the Au layer on the transducer. Even without the melting of the Au layer, similar challenges in studying higher amplitude, highly nonlinear phenomena in adhesive, microscale granular media arise due to the stochastic and irreversible reformation of the particle networks [207]. For the amplitude dependence experiments, we follow the procedure previously described in Sect. 5.3, wherein high- and low- amplitude excitations are characterized at F_{min} and then F_{max}. Acoustic signals measured over three repetitions of this process are shown in Fig. 5.9.

The amplitude dependence for all experiments is shown in Fig. 5.10 (also see Appendix D), where the lower static load is set to F_{min} and the high static load is set to the various levels of F_{max}, ranging from $F_0 = 2.0$ N ($F_R = 36$) to $F_0 = 6.3$ N ($F_R = 110$). In all cases, the increase of the high amplitude excitation sound speed relative to the low amplitude excitation is greater at smaller static loads. The data appears to fall mostly into two groups, namely, pre- and post-collapse cases. Overall, the post-collapse data generally shows a larger increase in sound speed compared to the pre-collapse data. A possible explanation for this result is that the contact geometry, and thus nonlinearity of the contact, is altered as a result of the multilayer collapse and particle rearrangement.

5.6 Simulation of Dependence on Excitation Amplitude

We compare the experimental results with simulations of a DEM of waves propagating through a 1D chain of adhesive spheres. We consider the sound speed as a function of excitation amplitude and static load. The equations of motion (shown in Appendix D.3) are solved via direct numerical integration, using a fourth-order Runge–Kutta scheme. The chain is composed of 2μm diameter silica spheres represented as point masses connected by Hertzian springs. Adhesion is modeled as a constant static load of F_{adh}. We model the pre- and post-collapse cases by probing the 90th and 25th spheres to approximately match the experimental multilayer thicknesses. To avoid capturing signals that contain boundary reflections, chain lengths are chosen to be 30 spheres longer than the probing lengths. The externally applied static loads considered range from 0.83 to 22μN, such that F_R in our simulations spans the entire range tested in the experiments, as determined from the range of F_0 tested, divided by the number of spheres covering the transducer area, assuming a hexagonal-close-packed arrangement. The excitations are modeled as a displacement applied to the first sphere, with a time profile obtained by interferometrically measuring the surface displacement of the previously described separate Au-coated microscope slide. In analyzing the simulated data, arrival times are determined using the same criteria as for the experimental data. Simulated time domain signals, with static loads chosen to match

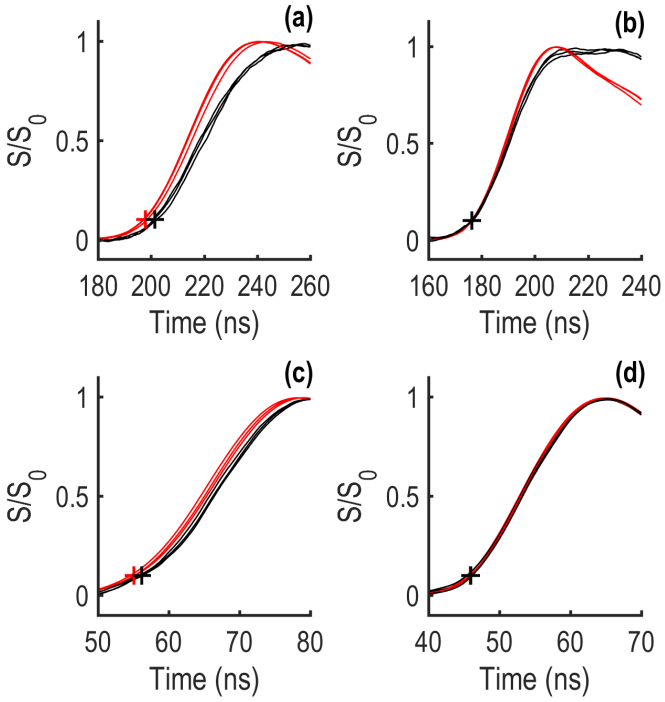

Figure 5.9: (a,b) Representative acoustic signals from the pre-collapse case at F_{min} (a) and F_{max} (b) static loads for the experiment denoted by yellow markers in Figs. 5.5 and 5.8(a). (c,d) Representative signals from the post-collapse case at F_{min} (c) and F_{max} (d) static loads for the experiment denoted by blue markers in Figs. 5.7 and 5.8(b). Red and black curves correspond to high- and low-excitation amplitudes, respectively. Cross markers denote a threshold of $S/S_0 = 0.1$. In panels (b,d), $F_{max} = 2.0$ N

those used in Fig. 5.9, are shown in Fig. 5.11. We note significant differences between the measured and simulated pulse shapes, which we attribute, in part, to disorder of the granular media. The percent increase in sound speed for the high amplitude excitation with respect to the low amplitude excitation as a function of the full range of static loads tested is shown in Fig. 5.10. We find that while the simulated trend of less amplitude dependence of the sound speed with increasing static load is in qualitative agreement with the experimen-

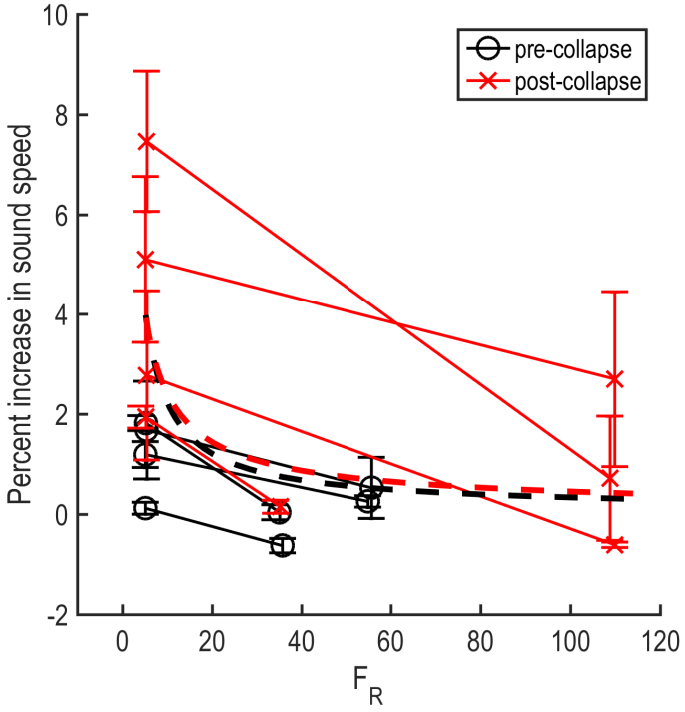

Figure 5.10: Percent increase in sound speed of high amplitude excitation, relative to low amplitude excitation, as a function of static load. The black circles represent the pre-collapse case and the red x's represent the post-collapse case. Data obtained from the same location and state (pre- or post-collapse) are connected by solid lines. The error bar height corresponds to the difference between sound speeds being calculated using thresholds of $S/S_0 = 0.1$ and $S/S_0 = 0.3$. The average increase in sound speed at F_{min} is $1.2 \pm 0.8\%$ and $4.3 \pm 2.5\%$ for the pre- and post-collapse cases, respectively, where the error is equal to the standard deviation of all four experiments. Black and red dashed lines represent simulation results for the pre- and post-collapse cases, respectively

tal data, the experimentally observed difference between pre- and post-collapse cases is not captured in the simulations. Additional plots showing the simulated dependence of sound speed on excitation amplitude and static load, for a larger range of excitation amplitudes,

can be found in the supplementary material (see Appendix D).

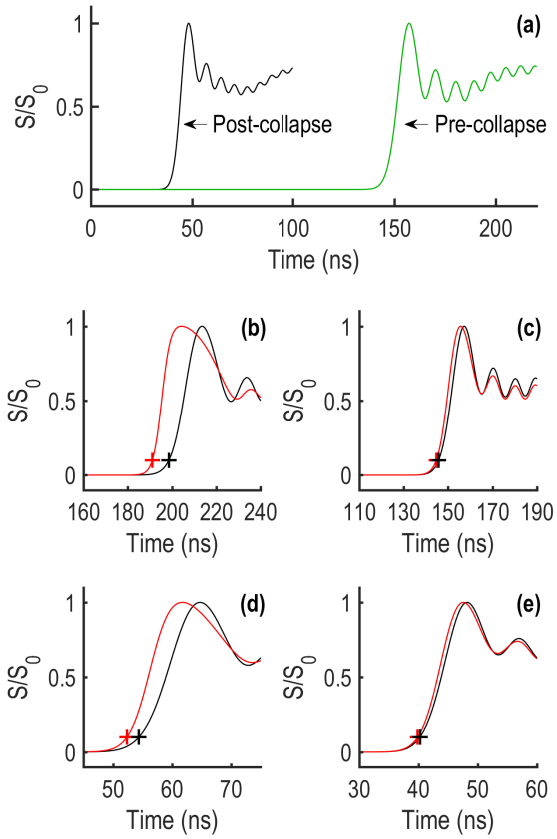

Figure 5.11: (a) Representative simulated displacement signals at the 90th (green curve) and 25th (black curve) spheres, representing the pre- and post-collapse cases, respectively. Both signals are simulated using the low-amplitude excitation and F_{max}. (b,c) Signals from the 90th sphere, representing the pre-collapse case, at F_{min} (b) and F_{max} (c) static loads. (d,e) Signals from the 25th sphere, representing the post-collapse case, at F_{min} (d) and F_{max} (e) static loads. Red and black curves in (b–e) correspond to high- and low-excitation amplitudes, respectively. Cross markers denote a threshold of $S/S_0 = 0.1$. In panels (a,c,e), $F_{max} = 2.0$ N

5.7 Discussion

A surprising finding of this study is the stark difference between the measured dependence of sound speed on applied static load for the pre- and post-collapse states. A potential cause for this observation is that, during the drying process, small amounts of contaminants in the colloidal suspension may be drawn to the interparticle contacts via capillary forces, forming solid bridges. Possible sources of contaminants could be residual silica, or polymers that have leached from the plastic vial containing the microsphere solution. Solid bridges could weaken the nonlinearity of the contact, reducing the sensitivity of sound speed to applied static loads. During the collapsing process, new contacts would be formed in the dry state. This explanation is also supported by the amplitude dependence experiments, in which we find greater dependence of sound speed on excitation amplitude for the post-collapse case, suggesting enhanced nonlinearity compared to the pre-collapse case.

Another potential explanation for the difference in sound speed dependence is that the stress distribution across the transducer-multilayer interface is less uniform for the pre-collapse case. For instance, if a significant portion of the static load is supported by a small region of the multilayer, which is not being probed during the experiments, then the sound speed could appear less sensitive to changes in static load than in a case with uniform stress. However, while the dependence of sound speed on static load varied between different probed regions of the transducer area, the measured exponents for the post-collapse case were consistently higher than those of the pre-collapse case (i.e. for all positions except one). Furthermore, if there had been reduced stress at the probe location for the pre-collapse case, then the dependence of sound speed on excitation amplitude would be more sensitive (due to lower static load) than the post-collapse case, which is the opposite of our findings. These results suggest that the differences in pre- and post-collapse behavior are not due to inhomogeneity of the applied load. Another possible cause of spatially dependent sound speed measurements is elastic heterogeneity, which may result from variation in sphere packing. However, the measurements made herein do not allow us to distinguish between the contributions of

elastic heterogeneity and nonuniform stress application. Whatever the cause, this position dependence is undesirable when determining the dependence of sound speed on static load, particularly with the large variations shown in Appendix D.2. Our finding of an average post-collapse exponent reasonably close to the predicted value of 1/6 suggests Hertzian mechanics, although confirmation requires further investigation due to the large uncertainty in our measurements.

The decrease of rise time with increasing static loads may be influenced by multiple mechanisms, one of which is dispersion induced by the discreteness of a granular medium. For instance, in a 1D discrete model system, acoustic waves travel with negligible dispersion at low frequencies, but become dispersive near, and attenuated above, the cutoff frequencies of the contact-based acoustic modes of the system. Within this context, the retention of higher frequency content due to stiffening of the interparticle contacts would lead to decreased rise times with increased static loading. Our granular medium is also disordered, which may cause further dispersion via disorder-induced scattering and mode localization. Such phenomena may result from inhomogeneity of the particle network, e.g., the existence of force chains, where a subset of particles bear significantly higher loads compared to the average of the entire assembly [91]. Force chain networks have been found to be dependent on static load, with the distribution of contact forces, and thus contact stiffnesses, becoming more uniform when static load is increased [92]. The distribution of contact stiffnesses has been found to affect scattering of acoustic pulses in a frequency dependent manner, with higher frequencies being predominantly affected and greater uniformity resulting in less scattering [208].

5.8 Conclusion

In this work, we have examined the dependence of the sound speed and pulse shape of acoustic waves in a disordered, multilayer aggregate of silica microspheres on static loading and excitation amplitude. Two cases are considered: the "pre-collapse" case, in which the particle networks are similar to their as-fabricated state, and the "post-collapse" case, in which the

applied static load is increased until the multilayer collapses, causing rearrangement and a decrease in thickness. By incrementally increasing the applied static load on themultilayer and measuring the time of flight of a laser generated acoustic pulse, we find that the sound speed increases in approximate agreement with predictions from the Hertz contact theory ($c \propto F^{1/6}$) for the post-collapse case. For the pre-collapse case, we find an anomalous dependence, where the increase in sound speed is much lower than predicted. We also find a decrease in rise time of the leading acoustic pulse with increasing applied static load, which we attribute to contact stiffening and a decrease of the inhomogeneity of the contact networks. Finally, we find an amplitude dependence of the sound speed that is consistent (with the exception of the observed differences between pre- and post-collapse behavior) with 1D DEM simulations of an adhesive Hertzian granular chain under compression.

This work may lead to future studies of nonlinear wave phenomena in microscale granular systems. In particular, studies of well-ordered multilayers could help facilitate comparisons with existing models of two- and three-dimensional granular materials [131,192,209] and their underlying contact mechanics, as has been the case for macroscale granular crystals [52,128]. Rotational dynamics are also more prevalent for microspheres than their macroscale counterparts, due to stronger interparticle shear forces caused by adhesion [119,130]. Experiments on microscale granular materials may assist in the development of effective models to account for such rotational dynamics [210], as well as provide a useful platform to study the interplay between rotation and nonlinearity [211]. Finally, this work may find use in the future study of the dynamics of powder-like materials, including energetic materials and geological materials, such as silts, as well as emerging types of self-assembled, microsphere-based materials [93].

5.9 Collaborator Contributions

S. P. Wallen provided overall guidance and wrote the code for the one-dimensional granular chain simulation used in this chapter.

Chapter 6

STRONGLY NONLINEAR ACOUSTIC WAVE PROPAGATION WITHIN ORDERED THREE-DIMENSIONAL MICROSCALE GRANULAR CRYSTALS [1]

6.1 Abstract

Nonlinearity, stemming from the contact geometry between discrete elastic particles, is a central element of granular crystals and the various proposed applications. A basic feature resulting from the geometric nonlinearity is that the sound speed can depend on the acoustic wave amplitude, wherein the sound speed has been observed to asymptotically approach a power law relation in the strongly nonlinear regime of three-dimensional aggregates of millimeter-sized macroscale spheres. On the other hand, highly nonlinear dynamics of granular crystals with microscale particles have thus far remained unexplored, and the dynamic response can not be assumed to be the same as their macroscale counterparts because different physics, such as adhesive forces, becomes important at small scales. Here, the nonlinear dynamic response of a three-dimensional granular crystal is characterized by measuring the sound speed of an acoustic pulse at variable excitation amplitudes spanning the linear, weakly nonlinear, and strongly nonlinear regimes. By accounting for the laser ultrasonic generation mechanism, a power law dependence of sound speed on acoustic wave amplitude is observed, with similar characteristics to macroscale experiments. This work is a preliminary exploration of strongly nonlinear dynamics of a three-dimensional granular crystal with particle diameter of a few microns or smaller and acts as a guide toward further research.

---

[1] Material within this chapter is from unpublished preliminary research.

6.2 Introduction

Much of the unique phenomena observed in granular crystals stems from a collective nonlinear dynamic response that depends on excitation amplitude [52, 56, 69, 76]. The field was born out of the discovery that nonlinear waves called solitons, which form due to the interplay between nonlinearity and dispersion, can be supported in one-dimensional granular crystals made of centimeter sized spheres [52, 65, 66, 68–71]. Nonlinearity is similarly essential for discrete breathers and shockwaves, both of which have subsequently been explored with great interest [52, 69, 72, 212]. Such complex nonlinear dynamics allow for highly tunable systems [76], with applications such as acoustic lenses [78], switches and rectifiers [79], and various schemes for controlling wave front shape and direction for impact mitigation [56, 62, 80].

The main source of nonlinearity in granular crystals comes from the mechanics of elastic spheres in contact, often modeled as the power law force-displacement relationship of $F \sim u^{3/2}$, derived by Heinrich Hertz in the nineteenth century [75]. One of the most fundamental consequences of this relationship is that sound speed can depend on the applied force, which has been experimentally investigated in assemblies of macroscale spheres. The simplest case of a statically compressed one dimensional chain of macroscale spheres with diameters ranging from millimeters to centimeters has been studied extensively, where the phase velocity is known to depend on the relative magnitudes of the amplitude of wave F_{max} and the static compressive force F_0, in which three regimes exist [52]. In the strongly nonlinear regime, solitons can form with phase velocities that are proportional to $c \sim {F_{max}}^{1/6}$, where F_{max} is the force amplitude of the wave [102], provided that F_{max} is much larger than the static compressive force F_0. In the linear regime, when $F_0 >> F_{max}$ and nonlinearity is negligible, the phase velocity becomes dispersive and no longer depends on F_{max}, instead increasing proportional to $c \sim F_0^{1/6}$. The transition between the two, when $F_{max} \approx F_0$, is called the weakly nonlinear regime, where soliton formation occurs but the phase velocity depends on both F_{max} and F_0.

Wave propagation in macroscale three-dimensional granular crystals is more complex than the one dimensional case [190], in part due to assemblies being highly sensitive to disorder and polydispersity [107,213], which produce nonuniform contact force distributions [92], even in hexagonally-close-packed crystalline arrays [214]. Contact force disorder can cause force chains to develop [91, 111], which are particle networks that bear higher loads compared to neighboring regions, and have been found to be responsible for wave front characteristics in certain systems [89, 90]. Because of the disorder in three-dimensional granular crystals, coherent solitons may not form in the same manner as one-dimensional crystals, however, it has been found that disordered packings of macroscale spheres still exhibit qualitatively similar dependence of phase velocity on wave amplitude, with linear, weakly nonlinear, and strongly nonlinear regimes that scale with F_{max} and F_0 according to power law relationships in agreement with the Hertzian contact solution [105, 215].

While there have been many studies examining nonlinear dynamics of macroscale granular crystals, there is relatively little understanding for their microscale counterparts, where sphere diameters are of a few micrometers or below. The distinction is critical because different factors come into play at small length scales, such as interparticle adhesive forces [121,216] that can: i) linearize the system for low amplitudes [77,118,119,139,151,169], ii) induce plasticity in the contact region [88,151], and iii) increase the role of shear forces and rotational dynamics [119], which are known to be supported in three-dimensional macroscale systems under static compression [86, 192], and are especially relevant in the context of nonlinear dynamics [211, 217].

Several studies on granular assemblies with particle diameters on the order of a few micrometers or smaller have been conducted [95–97, 169, 187], however, all were limited to low-amplitude excitation in the linear regime and did not explore nonlinear dynamics. Wave front velocity has been explored in a floating two-dimensional microscale granular crystal [98], however, the presence of liquid introduces large viscous and fluid dynamical forces and reduces interparticle adhesive forces [100], such that the dynamic response is expected to be

significantly different from the dry state.

The contact mechanics of single micro- and nanospheres have been probed by quasi-statically measuring force-displacement profiles, and mostly found Hertzian behavior up till the point of plastic deformation and fracture [87,113–116]. Another work, focused on single-sphere dynamics, investigated the relationship between two vibrational modes of single gold nanospheres adhered to a substrate and found behavior suggesting Hertzian contact mechanics, however, only sphere diameter was varied, and the nonlinear dynamics were not directly probed. Resonant frequency doubling of single-microspheres adhered to a substrate has been experimentally observed and modeled by Saeedi Vahdat et. al. [218, 219], wherein the frequency doubling resulted from nonlinear coupling between in-plane and out-of-plane modes. While research on the contact mechanics of single sphere behavior provides valuable insight, the collective nonlinear dynamics of three-dimensional granular crystals is expected to be more complex.

A recent work published by the author of this thesis [198], reviewed in Chapter 5, explored the effect of both static and dynamic force amplitudes on sound speed by measuring time-of-flight of acoustic pulses through a three-dimensional disordered microscale granular assembly while varying the static compressive force and excitation amplitude. While weakly nonlinear dynamics were observed, with reversible sound speed increases of a few percent, the strongly nonlinear regime was not explored because further amplitude increase caused melting of the gold film acting as a laser ultrasonic transducer, which was undesirable for the repeatability and the use of averaging over multiple excitation laser shots to improve the signal to noise ratio.

In this chapter, a preliminary study of nonlinear dynamics of an ordered three-dimensional microscale granular crystal is presented, wherein the sound speed is measured via time-of-flight of high-amplitude acoustic pulses excited with laser-induced ablation. The amplitude of the acoustic wave was found to not scale linearly with laser pulse energy, likely due to transitioning generation mechanisms, and by taking this into account, a sound speed

dependence on amplitude similar to macroscale experiments is observed. Comparison with a previous experiment of similar design, but with laser spot sizes, did not show a clear amplitude dependence, potentially suggesting the importance of large defects within the granular crystal.

6.3 Methods and Results

For the granular crystal fabrication, we use monodisperse polystyrene spheres of diameter D = 390 nm that form a high crystalline order. The granular crystal is assembled on a substrate that consists of a 1.5 mm thick glass microscope slide, which is coated with a 100 nm thick layer of aluminum to reflect the probe laser and then a 20 nm thick silica layer to facilitate the self-assembly process. The polystyrene spheres are synthesized using a surfactant-free emulsion polymerization process [188]. The crystals are fabricated using a vertical convective self-assembly technique [174, 189], and suspended in ethanol. A 20 mL capacity glass scintillation vial is filled with 10 mL of the colloidal suspension. The substrate is then held vertically while being immersed in the suspension. The substrate and suspension are then left to dry in ambient laboratory conditions. After complete drying, colloidal crystals are obtained, as shown in Fig. 6.1(b), although cracks and defects exist over large domains, as shown in Fig. 6.2. The free surface of the granular crystal is coated with 500 nm of aluminum via electron beam evaporation to absorb the pump laser light for ultrasound generation.

Laser ultrasonic characterization is performed with optical pump pulses (450 ps pulse duration, 532 nm wavelength) incident on the 500 nm aluminum film on the free surface of the granular crystal. The pump pulse is focused to an 80 μm diameter circular spot at $1/e^2$ intensity. The motion of the substrate surface attached to the granular crystal is detected with a phase-mask based interferometer [136], in which a single continuous wave (CW) laser beam (514 nm wavelength) is incident on a phase-mask and split into ± 1 diffraction orders to produce probe and reference beams focused to 40 μm diameter spots at $1/e^2$ intensity.

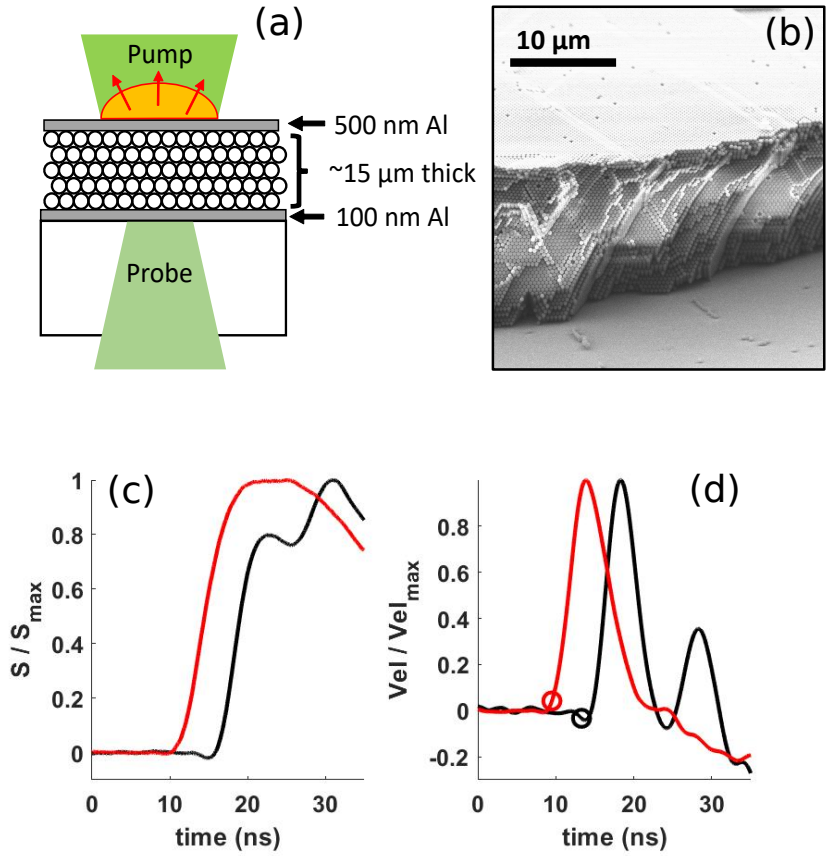

Figure 6.1: (a) Laser ultrasonic experimental setup. (b) Respresentative SEM image the edge of a fractured granular crystal to show the thickness and packing order. (c) Representative displacement profiles S divided by the maximum displacement amplitude S_{max} at one sample location. Black and red curves correspond to thermoelastic (0.05 μJ) and ablative (54.9 μJ) signals, respectively. (d) Velocity profiles Vel divided by the maximum velocity amplitude Vel_{max}. Black and red curves correspond to thermoelastic (0.05 μJ) and ablative (54.9 μJ) signals, respectively. Arrival times are determined when the normalized velocities cross a threshold of 0.03, indicated by the open circles. Velocities in (d) are found by numerically taking the derivatives of the displacements in (c).

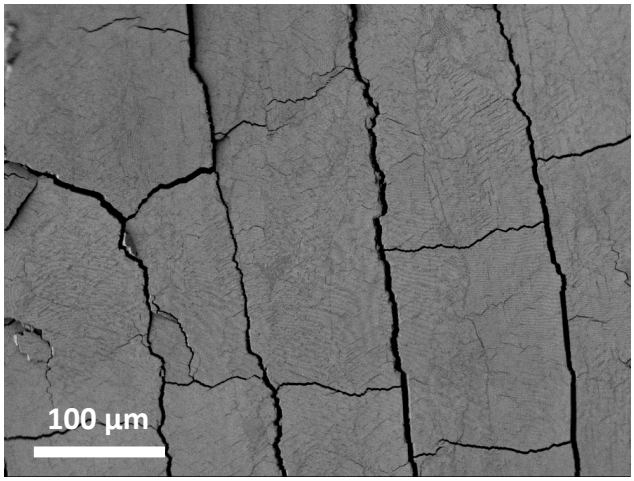

Figure 6.2: Top view SEM image of large domains with cracks and defects.

The probe and reference beams are focused through the glass substrate onto the 100 nm aluminum film, such that the probe is axially aligned with the pump, while the references is focused on a stationary portion of the substrate. The separation between the probe and reference is large enough that surface waves traveling perpendicular to the optical axis are not detected in the time frame of interest. Upon reflection from the sample, the probe and reference are recrossed onto the phase mask, and recombined interferometrically onto an amplified silicon photodetector (ET-2030A, Electro-Optics Technology Inc., 2 GHz bandwidth) where the signal is digitized and recorded using an oscilloscope.

To excite acoustic amplitudes sufficient to reach the strongly nonlinear regime, thermoelastic generation, which is non-destructive, is not sufficient. Further increase of excitation amplitude beyond the thermoelastic threshold results in ablation, in which the 500 nm aluminum film evaporates and forms a high-pressure plasma that exerts a reaction force on the granular crystal surface [134, 220]. Since this process is destructive, a new region of the sample must be tested for each experiment, which introduces variability due to uneven thickness over large sample areas and localized defects or alteration of crystalline arrangement, e.g., small regions of square packing. Packing arrangement and defects were shown to alter contact stiffness

and have a large effect on the dynamics of a two-dimensional granular crystal in Chapter 2 [119]. To account for this, a control experiment is first performed on the granular crystal at each new sample region by exciting low-amplitude acoustic pulses with non-destructive thermoelastic excitation (0.05 μJ pulse energy, 1 kHz rep rate, averaged over 1E4 pump pulses). Next, the single-shot high-amplitude ablative excitation is performed using pump energies ranging from 0.3 μJ $-$ 54.9 μJ. Representative thermoelastic and ablative signals, which are proportional to displacement of the interface between the granular crystal and substrate, are shown in Fig. 6.1(c) after being smoothed over 40 data points.

Sound speed is determined by the arrival of the acoustic pulse at the substrate after traveling through the granular crystal using a threshold of 0.03 of the normalized velocity profiles, calculated by taking the derivative of the displacement and smoothed again, as shown in Fig. 6.1(d). From here on, 'velocity' refers to the particle velocity Vel caused by the acoustic wave, and 'speed' refers to the speed of sound c, i.e., the speed at which disturbances propagate. Calculating time-of-flight from the velocity profile is preferable because it is also less sensitive to low-frequency noise and, for thermoelastic signals, occasionally there is a small dip in the displacement before the main pulse, which approaches the noise floor and does not consistently cross a suitable threshold, as can be seen in the thermoelastic data in Fig. 6.1(c). This dip may be caused by transient effects of thermal diffusion during the thermoelastic generation of acoustic waves [221, 222], though it is not always observed which we speculate is due to local packing differences that may also affect the pulse waveform and change depending on the region tested. While small, the dip occurs over a short time period, such that the amplitude is more pronounced in the velocity profile, as seen in Fig. 6.1(d).

The thermoelastic control experiment is incorporated into the analysis by calculating the normalized sound speed as $c_{L,norm} = \frac{c_{L,abl}}{c_{L,therm}}$, where $c_{L,abl}$ and $c_{L,therm}$ are the ablative and thermoelastic sound speeds, respectively. The calculated $c_{L,norm}$ for ablative pump energies ranging from 0.3 μJ $-$ 54.9 μJ increases with greater pump energies, as shown in Fig. 6.3. If the amplitude of the excitation scales linearly with pump energy, then a system with contacts

described by the Hertzian force-displacement relationship would be expected to approach $c_{L,norm} \sim (\text{pump energy})^{1/6}$ in the strongly nonlinear regime. However, excitation amplitude and pump energy may not have a linear relationship if ablative pump energies are near the transition to thermoelastic generation, which is governed by different mechanisms [134, 220]. Ideally, measurement of the granular crystal's free surface displacement during ultrasound generation would directly provide the excitation amplitude, however, such measurement is difficult due to the vaporization of the metal film and subsequent plasma formation. Instead, the excitation amplitude can be estimated by observing the velocity amplitude $Vel_{max,abl}$ of the acoustic pulse, launched by the single-shot ablative excitation, that has transmitted through the granular crystal and reaches the 100 nm aluminum film coated on the glass substrate. This measure of acoustic wave amplitude, $Vel_{max,abl}$, is plotted against pump energy in Fig. 6.4 and shows the relationship is not linear, especially near $\sim$ 1 μJ where a large jump in amplitude occurs. Note that units of velocity are given in millivolt per second (mV/s) because interferometer calibration data was not taken at the time of the experiment. The output of the interferometer, measured by the photodetector in units of millivolts, is proportional to displacement, thus the unit of millivolt per second is equivalent to an arbitrary unit of velocity.

To account for the effects of generation mechanism on excitation amplitude, $c_{L,norm}$ can be plotted against the velocity amplitude of the transmitted acoustic pulse $Vel_{max,abl}$ for each position on the granular crystal, as shown in Fig. 6.5(a). Note that $Vel_{max,abl}$ is the velocity of the 100 nm aluminum film coated on the substrate, which can be assumed to be a linear elastic material, and therefore proportional to the stress of the acoustic wave by means of the characteristic impedance. Except for one outlier, the data largely appears to follow the trend observed in [215], where low amplitudes showing little amplitude dependence are in the linear regime, moderate amplitudes showing sound speed increases of a few percent are in the weakly nonlinear regime, and high amplitudes showing sound speed increases of more than $\sim$10% approach the strongly nonlinear regime where a power law relationship is observed.

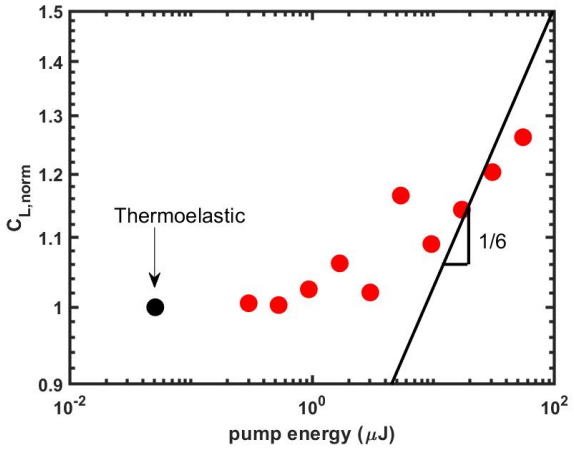

Figure 6.3: Normalized sound speed $c_{L,norm}$ as a function of ablative pump energy on a log-log scale. Each red point represents one experiment at a single position on the sample. The black point represents the thermoelastic control experiments and has $c_{L,norm}$ set to 1. The solid black line with a slope of 1/6 is added for a visual guide and corresponds to the Hertzian solution for sound speed's dependence on excitation amplitude in the strongly nonlinear regime.

A slope of 1/6, representing the power law relationship for Hertzian contacts, is added as a visual guide, and the data roughly approaches a similar trend as excitation amplitude is increased. Just as variations of the local granular crystal thickness and packing is accounted for by using the normalized sound speed, a similar procedure can be applied to the maximum velocity, where the normalized maximum velocity is defined as $Vel_{max,norm} = \frac{Vel_{max,abl}}{Vel_{max,therm}}$, where $Vel_{max,therm}$ is the velocity amplitude of the thermoelastic acoustic wave. Plotting $c_{L,norm}$ against $Vel_{max,norm}$, as shown in Fig. 6.5(b), displays a similar trend as Fig. 6.5(a).

6.4 Discussion

Although the dependence of sound speed on excitation amplitude was observed to follow a 1/6 power law relation in strongly nonlinear macroscale experiments [105, 215] and simula-

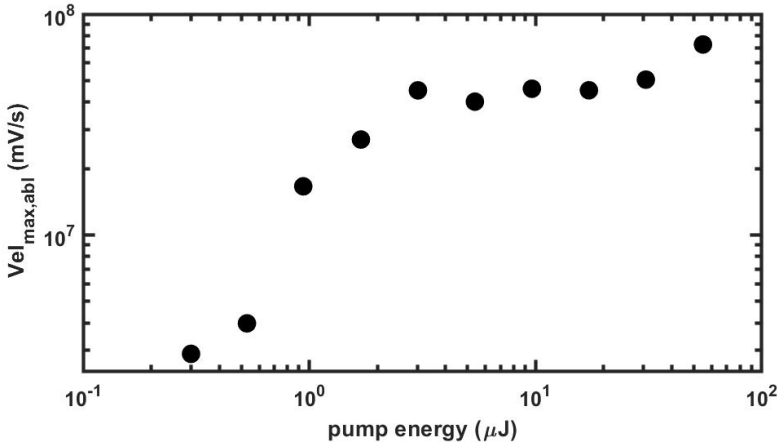

Figure 6.4: Amplitude of the transmitted acoustic particle velocity $Vel_{max,abl}$, launched from the single-shot ablative excitation and measured at 100 nm aluminum film coated on the substrate, plotted against pump energy. The velocity unit is given in millivolts per second (mV/s) by taking the derivative of the interferometer output, measured by a photodetector in units of millivolts.

tions [223], it is not necessarily obvious a similar result would be expected with microscale polymer spheres. In Chapter 4 [169], using the same polystyrene nanospheres, large contact stiffnesses and contact radii were observed that suggest initial plasticity may be present due to adhesive forces. Chapter 3 [151] similarly observed contact properties that suggest plastic deformation induced by adhesion. If plastic deformation is present in the static granular crystal, dynamic plasticity due to high-amplitude acoustic pulses should become an even greater factor. The effects of plasticity have been studied at the level of single contacts [224, 225] or along one-dimensional [226, 227] or two-dimensional [213] macroscale granular crystals. A model and experimental validation for the sound speed of elastic-plastic waves traveling through a macroscale one-dimensional granular chain was developed by Burgoyne et. al. [226], wherein the strongly nonlinear sound speed deviated from the power law relationship with excitation amplitude according to the Hertzian model and asymptoti-

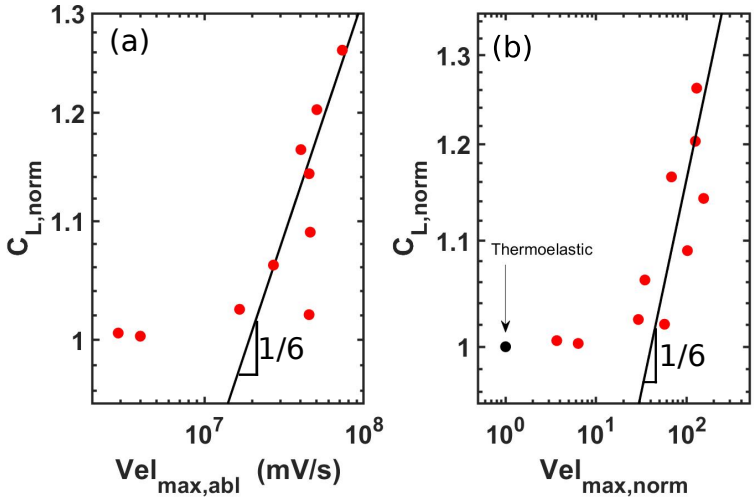

Figure 6.5: (a) Normalized sound speed $c_{L,norm}$ versus the amplitude of the ablation-generated particle velocity $Vel_{max,abl}$ measured at the 100 nm aluminum film on the substrate after transmitting through the granular crystal. (b) Normalized sound speed $c_{L,norm}$ versus the normalized amplitude of particle velocity $Vel_{max,norm}$, defined as $Vel_{max,abl}$ divided by the amplitude of the thermoelastic-generated particle velocity $Vel_{max,therm}$. The black point represents the thermoelastic control experiments and has both $c_{L,norm}$ and $Vel_{max,norm}$ set to 1.

cally approached a constant limiting value determined by the material properties. Given the likelihood of preexisting plastic deformation, one could reasonably expect similar behavior at the microscale, and this may indeed be true upon improving the accuracy of the experiment described in this chapter by expanding the number of data points per pump energy or increasing the maximum excitation amplitude by use of a higher powered laser. Further complexity is expected to arise from strain-rate dependent mechanical properties of materials, which has been studied in the context of plastic deformation of macroscale metallic spheres [225], and has been characterized for bulk polystyrene [228].

Lastly, it should be emphasized that the results presented in this chapter are preliminary

and serve only as a possible preview of what to expect from a more rigorous study. The whole picture may become more complicated upon expansion of the data set, as was the case for the initial attempt at this experiment, where the laser spot diameters were twice as large (pump = 160 μm $1/e^2$, probe = 80 μm $1/e^2$). These larger spot sizes have an area similar to the large crystal domains shown in Fig. 6.2, and special care was not taken in this initial experiment to avoid the large cracks and other defects from the region being tested. The data for this experiment, shown in Fig. 6.6 using the same experimental procedure as described previously, displays an increase in sound speed for all pump energies compared to the thermoelastic control experiment, however, there is significant scatter and no correlation between sound speed and excitation amplitude. This scatter and lack of correlation prompted the change to smaller spot sizes and taking close care in selection of the testing region.

6.5 Conclusion

The dependence of sound speed on excitation amplitude was explored in a three-dimensional microscale granular crystal using high-amplitude single-shot excitation, such that linear, weakly nonlinear, and strongly nonlinear regimes were reached. Sound speeds appear to have a power law dependence similar to macroscale experiments, though confirmation requires more data points per pump energy. Analysis reaveals that the generation mechanism needs to be accounted for by measuring the amplitude of the transmitted acoustic pulse, since the lowest energy single-shot ablative pump pulses appear to approach the transition from ablative to thermoelastic regimes. Special care must also be taken to avoid measuring on or near large cracks in the granular crystal, which may explain the different behavior compared to a previous data set where this was not the case.

Moving forward, more data points are needed, particularly for lower pump energies where the signal to noise ratio is not as good for single-shot measurements. Improved sample fabrication methods to avoid large cracks and defects, such using optical tweezers to place individual microspheres [229], is another avenue to increase repeatability, however, perfect

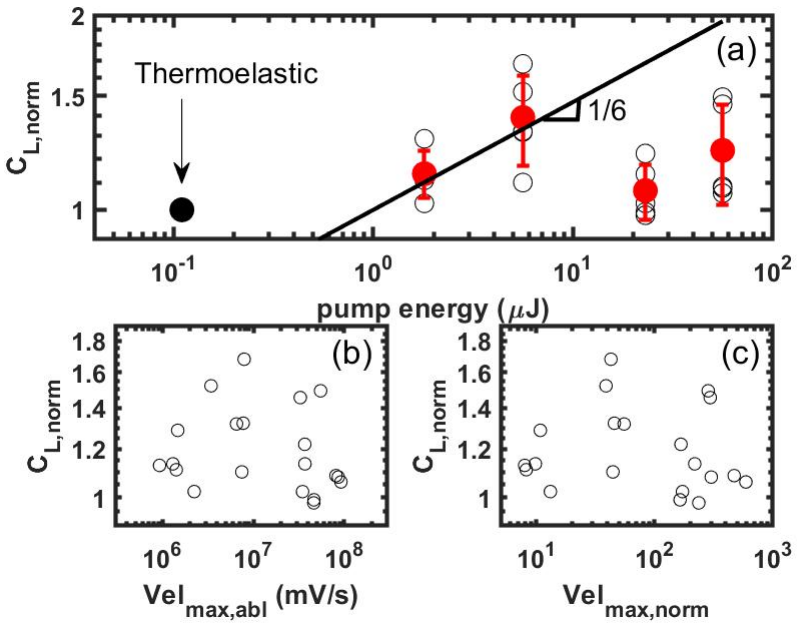

Figure 6.6: (a) Normalized sound speed $c_{L,norm}$ as a function of ablative pump energy on a log-log scale. Red points represent the average $c_{L,norm}$ at each pump energy (n=5) and the errorbars are the standard deviation. Each open black circle represents one experiment at a single position on the sample. The solid black point represents the thermoelastic control experiments and has $c_{L,norm}$ set to 1. The solid black line with a slope of 1/6 is added for a visual guide. (b) Normalized sound speed $c_{L,norm}$ versus the amplitude of the ablation-generated particle velocity $Vel_{max,abl}$ measured at the 100 nm aluminum film on the substrate after transmitting through the granular crystal. (c) Normalized sound speed $c_{L,norm}$ versus the normalized amplitude of particle velocity $Vel_{max,norm}$, defined as $Vel_{max,abl}$ divided by the the amplitude of the thermoelastic-generated particle velocity $Vel_{max,therm}$.

ordering in the context of contact-mediated acoustic waves is likely not realistic with currently available methods, as disorder and non-repeatable wave forms remains an issue even in macroscale two-dimensional granular crystals that are built manually by hand, with sphere-by-sphere placement [107, 213]. Another change that may help distinguish the effects of

intrinsic material nonlinearity, such as plasticity, from the effects of geometric nonlinearity is the use of nanospheres that have a greater yield strength, e.g., the silica spheres used in Chapter 5 [198]. The greater density of silica poses challenges for the vertical convective self-assembly technique used in this chapter due to sedimentation, though others have solved this by mechanical agitation through solution injection [230] or convection induced by a temperature gradient [231]. Another factor to consider is the role of solid bridges caused by debris in the self assembly process [169] that may decrease the effects of geometric nonlinearity compared to the case without bridges, which could possibly be removed through selective chemical etching. This work is the first characterization of strongly nonlinear dynamics in an ordered microscale three-dimensional granular crystal and serves as a starting point for further exploration of nonlinear phenomena that may be supported in similar systems, such as solitary waves [52,65,66,68–71], discrete breathers [69,72], and shear to longitudinal mode conversion [211,217].

6.6 Collaborator Contributions

Nicolas Vogel provided guidance on the vertical convective self assembly sample fabrication method used in this chapter.

Chapter 7

CONCLUSIONS AND OUTLOOK

The work contained in this thesis was performed as piece-by-piece building blocks to explore whether three-dimensional microscale granular crystals can support nonlinear dynamics similar to macroscale systems, which have produced a large body of research over the past few decades.

In Chapter 2, elements essential to three dimensional microgranular crystals were studies in a two-dimensional system to simplify and reduce the number of variables. The first element was exploring the linear dynamics of a monolayer of spheres when motion within a plane is considered, i.e., vertical, horizontal, and rotational degrees of freedom. These degrees of freedom are known to affect wave propagation in three-dimensional macroscale granular crystals [86], yet experimental observation and analysis of the two horizontal-rotational monolayer modes through the lens of a unified theory in a microscale granular crystal was lacking until the results from this chapter. Not only is this a step forward to understanding dynamics of three-dimensional microgranular crystals, it also has implications for nonlinear dynamics such as longitudinal to shear mode conversion, where particle rotations are essential. Furthermore, the importance of adhesion is apparent because horizontal-rotation modes were supported in the as-fabricated microgranular crystal, which was not the case for macroscale systems that required application of externally applied loads [179, 192, 232]. The second element was to study interparticle mediated vibrational modes in a monolayer, which is important to wave propagation in three-dimensional granular crystals as such waves are purely composed of interparticle-mediated modes. The findings within this chapter demonstrate the importance of particle packing and network formation, which is a factor that

dominates the microscale due to adhesion. Small packing variations and changes to the interparticle network, tuned by deposition of a thin nanometric film of aluminum, altered the resonant frequencies of interparticle modes drastically. Interparticle mediated modes in two-dimensional macroscale systems have proven instrumental to understanding phenomena such as force chains [90], thought to heavily influence the behavior of three-dimensional systems, and the results in this chapter represent a potential avenue to do similar at the microscale. Monolayer dynamics had been studied in a similar system previously, however, interparticle mediated modes were not identified in that work, likely due to using a different acoustic generation and detection technique.

In Chapter 3, the contact mechanics of a monolayer of polymer microspheres adhered to substrate were explored, which is expected to be the fundamental source of geometric nonlinearity that produces nonlinear dynamics in microgranular crystals. Three different methods of quantifying the contact behavior were compared by assuming a purely elastic Hertzian contact, which accurately describes macroscale spheres in nearly all cases. However, with polymer microspheres the results of the three techniques varied widely if Hertzian behavior was assumed, suggesting inaccuracy of this model for the microspheres used in this chapter and the possibility of plastic deformation in the contact region causing significant deviations in nonlinear dynamics between micro- and macroscale granular crystals. This point should be carefully considered when observing nonlinear behavior of polymer micropspheres and when choosing microsphere material to conduct such studies. In addition to probing the contact mechanics, one of the three methods used for comparison was particle ejection via high-amplitude acoustic excitation, which is an intermediate step towards similar excitation of three-dimensional microgranular crystals to observe nonlinear dynamics. Lastly, this chapter further demonstrates the importance of particle network and adhesion by observing the morphology of the monolayer after ejection, namely, the formation of monolayer "flakes" mostly composed of single crystalline domains from a sample with mixed ordered and disordered regions.

In Chapter 4 the linear dynamic behavior of a multi-layered three-dimensional microgranular crystal was investigated by exciting low-amplitude standing acoustic waves and fitting the measurements with a discrete coupled oscillator model. The stiffness was found to be much higher than an elastic adhesive model prediction, due to solid bridges that form during the fabrication process, in addition to the likely adhesion-induced plasticity. It was discovered the fabrication technique used to produce three-dimensional microgranular crystals is especially susceptible to solid bridge formation, compared to a technique for monolayers. Solid bridges, and the accompanying increase is contact stiffness, are highly detrimental to the observation of nonlinear dynamics because the alteration on contact geometry requires a greater excitation amplitude to reach the nonlinear regime. These results inform nonlinear studies by drawing attention to the use of fabrication techniques and significant influence of solid bridges in the contact region that may form as a result.

In Chapter 5, the nonlinear nature of the contact and its effect on wave propagation was directly investigated in a disordered three-dimensional system of many silica microspheres layers by measuring the sound speed of acoustic pulses under different static and dynamic loads. A disordered arrangement was specifically chosen to better facilitate uniform application of static loads across the entire sample. Informed by results of chapters Chapters 3 and 5, the choice of silica over polystyrene was made to reduce plasticity and the equilibrium static overlap, such that nonlinear dynamics due to geometric nonlinearity can be observed at lower amplitudes. By changing the static load the sound speed was reversibly tuned qualitatively analogous to macroscale granular crystals, however, the nonlinearity was initially much weaker until the sample was mechanically conditioned with large scale rearrangement, after which the sound speed was observed to increase roughly approximate to Hertzian prediction. Following results from Chapter 4, it is hypothesized that the initial reduction in nonlinearity was due to debris and contaminants in the contact region from fabrication creating solid bridges and altering the geometry, which subsequently break upon particle rearrangement. Nonlinear dynamics were also studied by comparing low- and high-excitation amplitudes,

which was the first of its kind for a system of uniform spheres of a few microns or smaller where adhesive forces are dominant. Similar to the static load results, the dynamic nonlinear behavior was in roughly approximate agreement with Hertzian theory after rearrangement conditioning, but significantly weaker prior to that. While analysis of nonlinear behavior was mostly limited to the measured sound speed, this work hints that the complex nonlinear dynamics seen in macroscale applications may be possible at the microscale because the fundamental element of geometric nonlinearity similarly influences the dynamics in certain cases. However, special consideration must be taken regarding the fabrication method and conditioning, possibly through particle rearrangement or perhaps conditioning the contacts to remove debris through horizontal-rotational modes.

In Chapter 6 the nonlinear dynamic response of a three-dimensional granular crystal was explored in a preliminary study by measuring the sound speed of an acoustic pulse at variable excitation amplitudes spanning the linear, weakly nonlinear, and strongly nonlinear regimes. A particular challenge is that near the transition from ablative to thermoelastic generation of acoustic waves, the amplitude does not increase steadily, likely due being in a transitional regime between generation mechanisms. By accounting for this, a power law dependence of sound speed on acoustic wave amplitude is observed, with similar characteristics to macroscale experiments. The full picture may be more complex, as comparison to an earlier experiment with larger spot sizes revealed a nearly constant increase in sound speed, independent of excitation amplitude. Expanding the data set to include multiple measurements for each excitation amplitude is needed for a rigorous analysis.

The overall results of this thesis demonstrate the important role of several phenomena stemming from adhesion in microscale granular systems. The findings regarding horizontal-rotational modes, network formation in two-dimensional systems, alterations of contact geometry during fabrication, adhesion-induced plasticity, and the dependence of sound speed on static and dynamic loads are expected to be crucial considerations for any future research in this field. By taking a systemic, gradual approach towards understanding the afore-

mentioned phenomena, this thesis provides a platform to further explore the possibility of architectured materials with tailored nonlinear dynamic functionalities similar to macroscale granular crystals.

The next logical step on this path would be to further study nonlinear dynamics in a three-dimensional microgranular crystal in detail. While Chapter 6 presented an initial exploration, additional work is needed to improve the accuracy, by increasing the number of measurements at each amplitude, and to elucidate the role of plasticity by performing similar measurements with particles that have a greater yield strength. Another proposal involves restricting dynamics to a two-dimensional system, as in Chapter 2, which facilitates closer experimental inspection of spatial information such as force chains along the interparticle networks. The clarity of horizontal-rotational modes, and the ease of exciting such modes via Rayleigh waves, provides a platform that may be well suited to exploration of highly nonlinear dynamics such as longitudinal to shear mode conversion. Two-dimensional imaging of path propagation and position-dependent frequency analysis of a high-amplitude point source excitation in such a system may reveal such dynamics, however, the experimental design must consider possible issues such as confinement of particle motion to keep particles from completely ejecting from the monolayer and interaction with confining surfaces, as discussed in the following.

A particular challenge of microscale granular crystals is that, for strongly nonlinear dynamics to be observed, dynamic interparticle forces due to the acoustic wave need to be greater than the static adhesive force, such that excitation will likely cause particles to separate from their neighbors. Separated particles will either be completely ejected or adhere to another surface after coming into contact, forming new contact networks that can alter the dynamic response. Two- and three-dimensional macroscale granular crystals are known to be highly sensitive to small changes in the contact network, despite spheres being able to move relative to each other and settle in nominally well-ordered arrays without adhering. At the microscale or smaller, this issue is only exacerbated. Confinement of the granular crystal

within a chamber would likely retain the nominal crystal ordering after high-amplitude excitation, however, alteration of the contact network may persist due to introduction of new surfaces that particles can adhere to. Therefore, experimentally investigating strongly nonlinear dynamics in microgranular crystals will likely involve destruction of the entire crystal, or at least a permanent change of the contact network, requiring experiments that are single-shot, bringing about additional issues of repeatability and signal to noise ratio, as described in Chapter 6. Disorder is another challenge that is especially prevalent at the microscale due to the fabrication methods and adhesion restricting "settling" of three-dimensional arrangements, as described in Chapter 6, though advances in assembly may start to address this [229]. This thesis confronts some of the particular experimental challenges when faced while exploring microscale granular crystals, while simultaneously demonstrating the rich physics that make these structures so attractive for manipulation of mechanical waves.

Although much of this work is a fundamental exploration of the dynamical response of granular crystals, it also makes progress toward some immediate, practical applications on multiple fronts. Observation of new monolayer hortizontal-rotational modes, and demonstration of their tunability through modification of interparticle contacts, may find use in configurable SAW filters for radio frequency signal processing in mobile devices by introduction of multiple attenuation zones that can be tuned through altering the interparticle contact stiffness, as achieved by metal deposition in Chapter 2. Additionally the rotational modes were found to be highly sensitive to interparticle stiffness, which may be of useful for sensing applications such as bioanalytical devices [150]. Characterizing nonlinearity stemming from contact mechanics is important for nearly all granular crystal applications that have been proposed or demonstrated with macroscale spheres, such as acoustic rectification [79] and logic elements [233]. By reducing particle size to the microscale or smaller, similar devices may be possible at much higher frequencies, even approaching that of lattice vibrations that contribute to thermal conductivity [81]. Furthermore, since solitary waves in one-dimensional chains interacting via Hertzian potentials have a constant spatial length of five particle di-

ameters, extremely short wavelengths may be possible as particle sizes are reduced, allowing for higher resolution acoustic microscopy [18, 19]. Measuring the dependence of sound speed on static and dynamic loads is one of the most fundamental ways to characterize the root of more complex nonlinear dynamics, in addition to having a direct influence on several applications. For example, the dependence of sound speed on static and dynamic loads this is central to acoustic lenses [78], which have applications in medical ultrasound or flaw detection in structural materials. This is similarly important for some impact mitigation structures made of granular crystals that have shown performance enhancements compared to commonly use materials [62] or wave front shaping through designed anisotropy [80]. Lastly, the systems studied in this thesis can be thought of as idealized and simplified models for natural granular media, such as sand or soil, and provide insights to geological exploration [101, 199].

Whether microscale granular crystals can successfully be utilized for such applications depends on addressing the challenges noted above, particularly disorder, which is likely to be a limiting factor of translating the dynamics seen in macroscale granular crystals to the microscale because many are predicated on dispersion induced by the crystalline order. Disorder tends to increase when macroscale granular crystals are composed of two- or three-dimensional assemblies, so developing a fabrication method that creates a microscale one-dimensional chain could address this issue, though one must consider motion of additional degrees of freedom if free-standing or, if the chain is confined, interaction with confining surfaces. Beyond the obvious solution of improving the crystal order through more precise fabrication methods, it may also be beneficial to research phenomena that require disorder, instead of being hampered by it, such as Anderson localization [234, 235] or the evolution of force chain propagation [89–91].

BIBLIOGRAPHY

[1] C. Hopkins, *Sound insulation*. Routledge, 2012.

[2] M. L. Munjal, *Acoustics of ducts and mufflers with application to exhaust and ventilation system design*. John Wiley & Sons, 1987.

[3] E. I. Rivin, "Passive vibration isolation," 2003.

[4] A. M. S. Baz, *Active and passive vibration damping*. Hoboken, NJ: John Wiley & Sons Inc., 2019.

[5] J. C. Snowdon, "Vibration isolation: Use and characterization," *The Journal of the Acoustical Society of America.*, vol. 66, no. 5, pp. 1245–1274, 1979.

[6] M. A. Meyers, *Dynamic behavior of materials*. New York: Wiley, 1994.

[7] N. V. David, X.-L. Gao, and J. Q. Zheng, "Ballistic resistant body armor: Contemporary and prospective materials and related protection mechanisms," *Applied Mechanics Reviews*, vol. 62, no. 5, 2009.

[8] A. Subic, ed., *Materials in sports equipment*. Woodhead Publishing Series in Composites Science and Engineering, Duxford: Woodhead Publishing, an imprint of Elsevier, second edition. ed., 2019.

[9] J. Webster, "Special issue on personal protective equipment in sport," *Proceedings of the Institution of Mechanical Engineers.*, vol. 230, no. 1, pp. 3–4, 2016.

[10] J. A. Ambrósio, M. F. S. Pereira, and F. P. da Silva, *Crashworthiness of transportation systems: structural impact and occupant protection*, vol. 332. Springer Science & Business Media, 2012.

[11] A. G. Mamalis, D. E. Manolakos, G. A. Demosthenous, and M. B. Ioannidis, "Vehicle crashworthiness," in *Crashworthiness of Composite Thin-Walled Structural Components*, pp. 5–18, CRC Press, 1 ed., 1998.

[12] W. W. Johnson, *Crashworthiness of vehicles : an introduction to aspects of collision of motor cars, ships, aircraft and railway coaches*. London: Mechanical Engineering Publications, 1978.

[13] E. Grossman, I. Gouzman, and R. Verker, "Debris/micrometeoroid impacts and synergistic effects on spacecraft materials," *MRS bulletin*, vol. 35, no. 1, pp. 41–47, 2010.

[14] B. S. Hertzberg, *Ultrasound : the requisites*. Requisites in radiology, Philadelphia, PA: Elsevier, third edition. ed., 2016.

[15] S. K. Edelman, *Understanding ultrasound physics*. ESP Woodlands, 2012.

[16] P. J. Shull, *Nondestructive evaluation: theory, techniques, and applications*. CRC press, 2002.

[17] P. E. Mix, *Introduction to nondestructive testing: a training guide*. John Wiley & Sons, 2005.

[18] R. G. Maev, *Acoustic microscopy: Fundamentals and applications*. John Wiley & Sons, 2008.

[19] A. Briggs, *Advances in acoustic microscopy*, vol. 1. Springer Science & Business Media, 2013.

[20] Z. Yu and S. Boseck, "Scanning acoustic microscopy and its applications to material characterization," *Reviews of Modern Physics*, vol. 67, no. 4, p. 863, 1995.

[21] A. D. Waite and A. Waite, *Sonar for practising engineers*, vol. 3. Wiley New York, 2002.

[22] V. Robertson, F. Duck, K. G. Baker, V. J. Robertson, and F. A. Duck, "A review of therapeutic ultrasound: Biophysical effects," *Physical therapy : journal of the American Physical Therapy Association.*, vol. 81, no. 7, pp. 1351–1358, 2001.

[23] K.-y. Ng and Y. Liu, "Therapeutic ultrasound: Its application in drug delivery," *Medicinal research reviews.*, vol. 22, no. 2, pp. 204–223, 2002.

[24] N. B. Smith, M. R. Bailey, G. J. Czarnota, K. Hynynen, D. L. Miller, N. B. Smith, M. R. Bailey, G. J. Czarnota, and I. R. S. Makin, "Overview of therapeutic ultrasound applications and safety considerations," *Journal of ultrasound in medicine.*, vol. 31, no. 4, pp. 623–634, 2012.

[25] C.-J. Wang, "Extracorporeal shockwave therapy in musculoskeletal disorders," *Journal of orthopaedic surgery and research.*, vol. 7, no. 1, p. 11, 2012.

[26] C. Coussios and G. ter Haar, "High intensity focused ultrasound: Physical principles and devices," *International journal of hyperthermia.*, vol. 23, no. 2, pp. 89–104, 2007.

[27] A. Ozcelik, J. Rufo, F. Guo, Y. Gu, P. Li, J. Lata, and T. J. Huang, "Acoustic tweezers for the life sciences," *Nature Methods*, vol. 15, no. 12, pp. 1021–1028, 2018.

[28] C. S. Wu, G. K. Padhy, W. Ding, S. Kumar, C. Wu, G. Padhy, and W. Ding, "Application of ultrasonic vibrations in welding and metal processing: A status review," *Journal of manufacturing processes.*, vol. 26, pp. 295–322, 2017.

[29] C. C. W. Ruppel, "Acoustic wave filter technology–a review," *IEEE transactions on ultrasonics, ferroelectrics, and frequency control.*, vol. 64, no. 9, pp. 1390–1400, 2017.

[30] C. Campbell, *Surface Acoustic Wave Devices for Mobile and Wireless Communications, Four-Volume Set*. Academic press, 1998.

[31] A. D. Pierce, *Acoustics: An Introduction to Its Physical Principles and Applications*. Springer, 2019.

[32] K. F. Graff, *Wave motion in elastic solids*. Knovel Library, New York: Dover Publications, 1991.

[33] R. Christensen, *Theory of viscoelasticity: an introduction*. Elsevier, 2012.

[34] P. Deymier, *Acoustic Metamaterials and Phononic Crystals*. Springer Series in Solid-State Sciences, Springer Berlin Heidelberg, 2013.

[35] M. H. Lu, L. Feng, and Y. F. Chen, "Phononic crystals and acoustic metamaterials," *Materials Today*, vol. 12, no. 12, pp. 34–42, 2009.

[36] M. I. Hussein, M. J. Leamy, and M. Ruzzene, "Dynamics of phononic materials and structures: Historical origins, recent progress, and future outlook," *Applied Mechanics Reviews*, vol. 66, no. 4, pp. 1–38, 2014.

[37] F. R. Montero de Espinosa, E. Jiménez, and M. Torres, "Ultrasonic band gap in a periodic two-dimensional composite," *Phys. Rev. Lett.*, vol. 80, pp. 1208–1211, Feb 1998.

[38] J. V. Sánchez-Pérez, D. Caballero, R. Mártinez-Sala, C. Rubio, J. Sánchez-Dehesa, F. Meseguer, J. Llinares, and F. Gálvez, "Sound attenuation by a two-dimensional array of rigid cylinders," *Phys. Rev. Lett.*, vol. 80, pp. 5325–5328, Jun 1998.

[39] M. A. Ghanem, A. Khanolkar, H. Zhao, and N. Boechler, "Nanocontact Tailoring via Microlensing Enables Giant Postfabrication Mesoscopic Tuning in a Self-Assembled Ultrasonic Metamaterial," *Advanced Functional Materials*, vol. 30, no. 10, pp. 1–7, 2020.

[40] N. Fang, D. Xi, J. Xu, M. Ambati, W. Srituravanich, C. Sun, and X. Zhang, "Ultrasonic metamaterials with negative modulus.," *Nature materials*, vol. 5, pp. 452–6, jun 2006.

[41] Z. Liu, "Locally Resonant Sonic Materials," *Science*, vol. 289, pp. 1734–1736, sep 2000.

[42] V. E. Gusev and O. B. Wright, "Double-negative flexural acoustic metamaterial," *New Journal of Physics*, vol. 16, no. 12, p. 123053, 2014.

[43] H. Huang, C. Sun, and G. Huang, "On the negative effective mass density in acoustic metamaterials," *International Journal of Engineering Science*, vol. 47, pp. 610–617, apr 2009.

[44] X. Zhang and Z. Liu, "Negative refraction of acoustic waves in two-dimensional phononic crystals," *Applied Physics Letters*, vol. 85, no. 2, pp. 341–343, 2004.

[45] M. Ke, Z. Liu, C. Qiu, W. Wang, J. Shi, W. Wen, and P. Sheng, "Negative-refraction imaging with two-dimensional phononic crystals," *Phys. Rev. B*, vol. 72, p. 064306, Aug 2005.

[46] Y. H. Liu, C. C. Chang, R. L. Chern, and C. C. Chang, "Phononic band gaps of elastic periodic structures: A homogenization theory study," *Physical Review B - Condensed Matter and Materials Physics*, vol. 75, no. 5, pp. 1–8, 2007.

[47] Y. Jin, B. Djafari-Rouhani, and D. Torrent, "Gradient index phononic crystals and metamaterials," *Nanophotonics*, vol. 8, no. 5, pp. 685–701, 2019.

[48] A. Banerjee, R. Das, and E. P. Calius, "Waves in Structured Mediums or Metamaterials: A Review," *Archives of Computational Methods in Engineering*, vol. 26, no. 4, pp. 1029–1058, 2019.

[49] F. di Cosmo, M. Laudato, and M. Spagnuolo, *c*, pp. 247–274. Cham: Springer International Publishing, 2018.

[50] V. Fokin, M. Ambati, C. Sun, and X. Zhang, "Method for retrieving effective properties of locally resonant acoustic metamaterials," *Physical Review B - Condensed Matter and Materials Physics*, vol. 76, no. April, pp. 1–5, 2007.

[51] A. Srivastava, "Elastic metamaterials and dynamic homogenization: A review," *International Journal of Smart and Nano Materials*, vol. 6, no. 1, pp. 41–60, 2015.

[52] V. Nesterenko, *Dynamics of heterogeneous materials*. Springer Science & Business Media, 2013.

[53] R. Martínez-Sala, J. Sancho, J. V. Sánchez, V. Gómez, J. Llinares, and F. Meseguer, "Sound attenuation by sculpture," *Nature*, vol. 378, no. 6554, p. 241, 1995.

[54] S. Yang, J. H. Page, Z. Liu, M. L. Cowan, C. T. Chan, and P. Sheng, "Ultrasound Tunneling through 3D Phononic Crystals," *Physical Review Letters*, vol. 88, no. 10, p. 4, 2002.

[55] Y. Achaoui, V. Laude, S. Benchabane, and A. Khelif, "Local resonances in phononic crystals and in random arrangements of pillars on a surface," *Journal of Applied Physics*, vol. 114, p. 104503, sep 2013.

[56] E. Kim and J. Yang, "Review: Wave propagation in granular metamaterials," *Functional Composites and Structures*, vol. 1, no. 1, p. 012002, 2019.

[57] S. A. Cummer, J. Christensen, and A. Alù, "Controlling sound with acoustic metamaterials," *Nature Reviews Materials*, vol. 1, no. 3, p. 16001, 2016.

[58] M. R. Haberman and A. N. Norris, "Acoustic metamaterials," *Acoustics Today*, vol. 12, no. 3, p. 31, 2016.

[59] J. von Neumann and E. Wigner, "Über das verhalten von eigenwerten bei adiabatischen prozessen," *Phys. Z.*, vol. 30, pp. 467–470, 1929.

[60] Y. Zheng, R. G. Maev, and I. Y. Solodov, "Review / Sythèse Nonlinear acoustic applications for material characterization: A review," *Canadian Journal of Physics*, vol. 77, no. 12, pp. 927–967, 2000.

[61] Z. Lu, Z. Wang, Y. Zhou, and X. Lu, "Nonlinear dissipative devices in structural vibration control: A review," *Journal of Sound and Vibration*, vol. 423, pp. 18–49, 2018.

[62] A. Leonard, L. Ponson, and C. Daraio, "Exponential stress mitigation in structured granular composites," *Extreme Mechanics Letters*, vol. 1, pp. 23–28, 2014.

[63] D. Grady, "Shocks and structured waves," in *Physics of Shock and Impact, Volume 1*, 2053-2563, pp. 1–1 to 1–103, IOP Publishing, 2017.

[64] J. Wang, R. L. Weaver, and N. R. Sottos, "Laser-induced decompression shock development in fused silica," *Journal of Applied Physics*, vol. 93, no. 12, p. 9529, 2003.

[65] A. N. Lazaridi and V. F. Nesterenko, "Observation of a new type of solitary waves in a one-dimensional granular medium," *Journal of Applied Mechanics and Technical Physics*, vol. 26, no. 3, pp. 405–408, 1985.

[66] C. Coste, E. Falcon, and S. Fauve, "Solitary waves in a chain of beads under Hertz contact," *Physical Review E*, vol. 56, no. 5, pp. 6104–6117, 1997.

[67] P. Hess and A. M. Lomonosov, "Solitary surface acoustic waves and bulk solitons in nanosecond and picosecond laser ultrasonics.," *Ultrasonics*, vol. 50, no. 2, pp. 167–71, 2010.

[68] A. Rosas and K. Lindenberg, "Pulse propagation in granular chains," *Physics Reports*, vol. 735, pp. 1–37, 2018.

[69] C. Chong, M. A. Porter, P. G. Kevrekidis, and C. Daraio, "Nonlinear coherent structures in granular crystals," *Journal of Physics: Condensed Matter*, vol. 29, p. 413003, sep 2017.

[70] S. Sen, J. Hong, J. Bang, E. Avalos, and R. Doney, "Solitary waves in the granular chain," *Physics Reports*, vol. 462, no. 2, pp. 21–66, 2008.

[71] V. F. Nesterenko, "Waves in strongly nonlinear discrete systems," *Philosophical Transactions of the Royal Society A: Mathematical, Physical and Engineering Sciences*, vol. 376, no. 2127, 2018.

[72] S. Flach and A. V. Gorbach, "Discrete breathers - Advances in theory and applications," *Physics Reports*, vol. 467, no. 1-3, pp. 1–116, 2008.

[73] T. K. Kim, J. K. Kim, and O. C. Jeong, "Measurement of nonlinear mechanical properties of PDMS elastomer," *Microelectronic Engineering*, vol. 88, no. 8, pp. 1982–1985, 2011.

[74] M. Destrade and G. Saccomandi, "Finite amplitude elastic waves propagating in compressible solids," *Physical Review E - Statistical, Nonlinear, and Soft Matter Physics*, vol. 72, no. 1, pp. 1–12, 2005.

[75] H. Hertz, "On the contact of elastic solids," *Z. Reine Angew. Mathematik*, vol. 92, pp. 156–171, 1881.

[76] M. A. Porter, P. G. Kevrekidis, and C. Daraio, "Granular crystals: Nonlinear dynamics meets materials engineering," *Physics Today*, vol. 68, no. 11, pp. 44–50, 2015.

[77] N. Boechler, J. Eliason, A. Kumar, A. Maznev, K. Nelson, and N. Fang, "Interaction of a contact resonance of microspheres with surface acoustic waves," *Physical review letters*, vol. 111, no. 3, p. 036103, 2013.

[78] A. Spadoni and C. Daraio, "Generation and control of sound bullets with a nonlinear acoustic lens," *Proceedings of the National Academy of Sciences of the United States of America*, vol. 107, no. 16, pp. 7230–7234, 2010.

[79] N. Boechler, G. Theocharis, and C. Daraio, "Bifurcation-based acoustic switching and rectification," *Nature Materials*, vol. 10, no. 9, pp. 665–668, 2011.

[80] A. Leonard and C. Daraio, "Stress wave anisotropy in centered square highly nonlinear granular systems," *Physical Review Letters*, vol. 108, no. 21, pp. 1–4, 2012.

[81] M. Maldovan, "Sound and heat revolutions in phononics.," *Nature*, vol. 503, no. 7475, pp. 209–17, 2013.

[82] B. V. Derjaguin, V. M. Muller, and Y. P. Toporov, "Effect of contact deformation on the adhesion of elastic solids," *Journal of Colloid and Interface Science*, vol. 53, no. 2, pp. 314–326, 1975.

[83] K. L. Johnson, K. Kendall, and A. D. Roberts, "Surface energy and the contact of elastic solids," *Proceedings of the Royal Society of London. A. Mathematical and Physical Sciences*, vol. 324, no. 1558, pp. 301–313, 1971.

[84] D. Maugis, "Adhesion of spheres: The JKR-DMT transition using a dugdale model," *Journal of Colloid And Interface Science*, vol. 150, no. 1, pp. 243–269, 1992.

[85] D. Tabor, "Surface forces and surface interactions," *Journal of Colloid And Interface Science*, vol. 58, no. 1, pp. 2–13, 1977.

[86] a. Merkel, V. Tournat, and V. Gusev, "Experimental evidence of rotational elastic waves in granular phononic crystals," *Physical Review Letters*, vol. 107, no. 22, pp. 1–5, 2011.

[87] S. Romeis, J. Paul, M. Hanisch, V. R. R. Marthala, M. Hartmann, R. N. K. Taylor, J. Schmidt, and W. Peukert, "Correlation of enhanced strength and internal structure for heat-treated submicron Stöber silica particles," *Particle and Particle Systems Characterization*, vol. 31, no. 6, pp. 664–674, 2014.

[88] X. D. Wang, Z. X. Shen, J. L. Zhang, H. F. Jiao, X. B. Cheng, X. W. Ye, L. Y. Chen, and Z. S. Wang, "Contact between submicrometer silica spheres," *Langmuir*, vol. 26, no. 8, pp. 5583–5586, 2010.

[89] A. H. Clark, L. Kondic, and R. P. Behringer, "Particle Scale Dynamics in Granular Impact," *Physical Review Letters*, vol. 109, no. 23, p. 238302, 2012.

[90] A. H. Clark, A. J. Petersen, L. Kondic, and R. P. Behringer, "Nonlinear force propagation during granular impact," *Physical Review Letters*, vol. 114, no. 14, pp. 1–5, 2015.

[91] T. S. Majmudar and R. P. Behringer, "Contact force measurements and stress-induced anisotropy in granular materials.," *Nature*, vol. 435, no. 7045, pp. 1079–1082, 2005.

[92] H. A. Makse, D. L. Johnson, and L. M. Schwartz, "Packing of Compressible Granular Materials," *Phys. Rev. Lett.*, vol. 84, no. 18, pp. 4160–4163, 2000.

[93] N. Vogel, M. Retsch, C.-A. Fustin, A. del Campo, and U. Jonas, "Advances in colloidal assembly: the design of structure and hierarchy in two and three dimensions," *Chemical reviews*, vol. 115, no. 13, pp. 6265–6311, 2015.

[94] W. Cheng, J. Wang, U. Jonas, G. Fytas, and N. Stefanou, "Observation and tuning of hypersonic bandgaps in colloidal crystals.," *Nature materials*, vol. 5, pp. 830–836, oct 2006.

[95] M. Mattarelli, M. Montagna, T. Still, D. Schneider, and G. Fytas, "Vibration spectroscopy of weakly interacting mesoscopic colloids," *Soft Matter*, vol. 8, pp. 4235–4243, 2012.

[96] A. Ayouch, X. Dieudonné, G. Vaudel, H. Piombini, K. Vallé, V. Gusev, P. Belleville, and P. Ruello, "Elasticity of an assembly of disordered nanoparticles interacting via either Van der Waals-bonded or covalent-bonded coating layers," *ACS Nano*, vol. 6, no. 12, pp. 10614–10621, 2012.

[97] I. Lisiecki, D. Polli, C. Yan, G. Soavi, E. Duval, G. Cerullo, and M. P. Pileni, "Coherent longitudinal acoustic phonons in three-dimensional supracrystals of cobalt nanocrystals," *Nano Letters*, vol. 13, no. 10, pp. 4914–4919, 2013.

[98] I. Buttinoni, J. Cha, W. H. Lin, S. Job, C. Daraio, and L. Isa, "Direct observation of impact propagation and absorption in dense colloidal monolayers," *Proceedings of the National Academy of Sciences of the United States of America*, vol. 114, no. 46, pp. 12150–12155, 2017.

[99] J. Brum, J. L. Gennisson, M. Fink, A. Tourin, and X. Jia, "Drastic slowdown of the Rayleigh-like wave in unjammed granular suspensions," *Physical Review E*, vol. 99, no. 4, pp. 1–9, 2019.

[100] J. Visser, "Particle Adhesion and Removal: A Review," *Particulate Science and Technology*, vol. 13, no. 3-4, pp. 169–196, 1995.

[101] J. Duffy and R. D. Mindlin, "Stress-strain relations and vibrations of a granular medium," *Journal of Applied Mechanics*, vol. 24, pp. 585–593, 1957.

[102] C. Coste and B. Gilles, "On the validity of Hertz contact law for granular material acoustics," *European Physical Journal B*, vol. 7, no. 1, pp. 155–168, 1999.

[103] X. Jia, C. Caroli, and B. Velicky, "Ultrasound Propagation in Externally Stressed Granular Media," *Physical Review Letters*, vol. 82, no. 9, pp. 1863–1866, 1999.

[104] H. A. Makse, N. Gland, D. L. Johnson, and L. Schwartz, "Granular packings: Nonlinear elasticity, sound propagation, and collective relaxation dynamics," *Physical Review E - Statistical, Nonlinear, and Soft Matter Physics*, vol. 70, no. 6, p. 061302, 2004.

[105] F. Santibanez, R. Zuñiga, and F. Melo, "Mechanical impulse propagation in a packing of 3D spheres confined at constant pressure," *Physical Review E - Statistical, Nonlinear, and Soft Matter Physics*, vol. 93, no. 1, p. 012908, 2015.

[106] S. N. Domenico, "Elastic properties of unconsolidated porous sand reservoirs," *Geophysics*, vol. 42, no. 7, pp. 1339–1368, 1977.

[107] B. Gilles and C. Coste, "Low-Frequency Behavior of Beads Constrained on a Lattice," *Physical Review Letters*, vol. 90, no. 17, p. 174302, 2003.

[108] P. J. Digby, "The effective elastic moduli of porous granular rocks," *Journal of Applied Mechanics, Transactions ASME*, vol. 48, no. 4, pp. 803–808, 1981.

[109] L. Ostrovsky and P. Johnson, "Dynamic nonlinear elasticity in geomaterials," *Rivista del nuovo cimento*, vol. 24, no. 7, pp. 1–46, 2001.

[110] V. E. Nazarov, a. V. Radostin, and I. a. Soustova, "Effect of an intense sound wave on the acoustic properties of a sandstone bar resonator. Experiment," *Acoustical Physics*, vol. 48, no. 1, pp. 76–80, 2002.

[111] H. M. Jaeger, S. R. Nagel, and R. P. Behringer, "The physics of granular materials," *Physics Today*, vol. 49, no. 4, pp. 32–38, 1996.

[112] R. A. Guyer and P. A. Johnson, "Nonlinear Mesoscopic Elasticity: Evidence for a New Class of Materials," *Physics Today*, vol. 52, no. 4, pp. 30–36, 1999.

[113] J. Paul, S. Romeis, J. Tomas, and W. Peukert, "A review of models for single particle compression and their application to silica microspheres," *Advanced Powder Technology*, vol. 25, no. 1, pp. 136–153, 2014.

[114] J. Y. He, Z. L. Zhang, M. Midttun, G. Fonnum, G. I. Modahl, H. Kristiansen, and K. Redford, "Size effect on mechanical properties of micron-sized PS-DVB polymer particles," *Polymer*, vol. 49, no. 18, pp. 3993–3999, 2008.

[115] K.-K. Liu, "Deformation behaviour of soft particles: a review," *Journal of Physics D: Applied Physics*, vol. 39, no. 11, pp. R189–R199, 2006.

[116] B. J. Briscoe, K. K. Liu, and D. R. Williams, "Adhesive contact deformation of a single microelastomeric sphere," *Journal of Colloid and Interface Science*, vol. 200, no. 2, pp. 256–264, 1998.

[117] I. U. Vakarelski, A. Toritani, M. Nakayama, and K. Higashitani, "Deformation and adhesion of elastomer microparticles evaluated by AFM," *Langmuir*, vol. 17, no. 17, pp. 4739–4745, 2001.

[118] Y. Guillet, B. Audoin, M. Ferrié, and S. Ravaine, "All-optical ultrafast spectroscopy of a single nanoparticle-substrate contact," *Physical Review B*, vol. 86, p. 035456, jul 2012.

[119] M. Hiraiwa, M. Abi Ghanem, S. Wallen, A. Khanolkar, A. Maznev, and N. Boechler, "Complex Contact-Based Dynamics of Microsphere Monolayers Revealed by Resonant Attenuation of Surface Acoustic Waves," *Physical Review Letters*, vol. 116, no. 19, p. 198001, 2016.

[120] A. Geslain, S. Raetz, M. Hiraiwa, M. Abi Ghanem, S. P. Wallen, A. Khanolkar, N. Boechler, J. Laurent, C. Prada, A. Duclos, P. Leclaire, and J.-P. Groby, "Spatial laplace transform for complex wavenumber recovery and its application to the analysis of attenuation in acoustic systems," *Journal of Applied Physics*, vol. 120, no. 13, p. 135107, 2016.

[121] J. N. Israelachvili, *Intermolecular and surface forces*. Waltham, MA: Academic press, 3 ed., 2011.

[122] K. L. Mittal and R. Jaiswal, *Particle adhesion and removal*. Beverly, MA: Wiley-Scrivener, 2015.

[123] Y. Min, M. Akbulut, K. Kristiansen, Y. Golan, and J. Israelachvili, "The role of interparticle and external forces in nanoparticle assembly.," *Nature materials*, vol. 7, no. 7, pp. 527–538, 2008.

[124] J. Duran and P. Sands, *Grains: An Introduction to the Physics of Granular Materials*. New York: Springer-Verlag, 2000.

[125] H. Masuda, K. Higashitani, and H. Yoshida, *Powder Technology Handbook*. Boca Raton, FL: CRC Press, 2006.

[126] P. A. L. Fernandes, M. Delcea, A. G. Skirtach, H. Möhwald, and A. Fery, "Quantification of release from microcapsules upon mechanical deformation with AFM," *Soft Matter*, vol. 6, no. 9, p. 1879, 2010.

[127] Y. Sato and T. Usami, "Basic Study on the oscillation of a homogeneous elastic sphere," *Geophysical Magazine*, vol. 31, no. 15, 1962.

[128] G. Theocharis, N. Boechler, and C. Daraio, "Nonlinear periodic phononic structures and granular crystals," in *Acoustic Metamaterials and Phononic Crystals*, pp. 217–251, Berlin, Heidelberg: Springer, 2013.

[129] D. Schneider, M. Schmitt, C. M. Hui, R. Sainidou, P. Rembert, K. Matyjaszewski, M. R. Bockstaller, and G. Fytas, "Role of polymer graft architecture on the acoustic eigenmode formation in densely polymer-tethered colloidal particles," *ACS Macro Letters*, vol. 3, no. 10, pp. 1059–1063, 2014.

[130] S. P. Wallen, A. A. Maznev, and N. Boechler, "Dynamics of a monolayer of microspheres on an elastic substrate," *Physical Review B - Condensed Matter and Materials Physics*, vol. 92, no. 17, p. 174303, 2015.

[131] V. Tournat, I. Pèrez-Arjona, A. Merkel, V. Sanchez-Morcillo, and V. Gusev, "Elastic waves in phononic monolayer granular membranes," *New Journal of Physics*, vol. 13, p. 073042, jul 2011.

[132] J. Sun, C.-J. Tang, P. Zhan, Z.-L. Han, Z.-S. Cao, and Z.-L. Wang, "Fabrication of centimeter-sized single-domain two-dimensional colloidal crystals in a wedge-shaped cell under capillary forces," *Langmuir*, vol. 26, pp. 7859–7864, jun 2010.

[133] B. H. Lee, H. Shin, and M. M. Sung, "Patterning a Two-Dimensional Colloidal Crystal by Water-Mediated Particle Transfer Printing," *Chemistry of Materials*, vol. 19, pp. 5553–5556, nov 2007.

[134] C. B. Scruby and L. E. Drain, *Laser Ultrasonics: Techniques and Applications*. New York: Taylor & Francis, 1990.

[135] E. Garova, A. Maradudin, and A. Mayer, "Interaction of Rayleigh waves with randomly distributed oscillators on the surface," *Physical Review B*, vol. 59, pp. 13291–13296, may 1999.

[136] C. Glorieux, J. D. Beers, E. H. Bentefour, K. Van de Rostyne, and K. A. Nelson, "Phase mask based interferometer: Operation principle, performance, and application

to thermoelastic phenomena," *Review of Scientific Instruments*, vol. 75, no. 9, pp. 2906–2920, 2004.

[137] R. D. Mindlin, "Compliance of elastic bodies in contact," *Journal of Applied Mechanics*, vol. 16, p. 259, 1949.

[138] V. Muller, B. Derjaguin, and Y. Toporov, "On two methods of calculation of the force of sticking of an elastic sphere to a rigid plane," *Colloids and Surfaces*, vol. 7, no. 3, pp. 251–259, 1983.

[139] A. Khanolkar, S. Wallen, M. A. Ghanem, J. Jenks, N. Vogel, and N. Boechler, "A self-assembled metamaterial for Lamb waves," *Applied Physics Letters*, vol. 107, no. 7, p. 071903, 2015.

[140] J. N. D'Amour, J. J. Stålgren, K. K. Kanazawa, C. W. Frank, M. Rodahl, and D. Johannsmann, "Capillary Aging of the Contacts between Glass Spheres and a Quartz Resonator Surface," *Physical Review Letters*, vol. 96, p. 058301, feb 2006.

[141] K. L. Johnson, *Contact Mechanics*. Cambridge: Cambridge University Press, 1985.

[142] D. M. Lipkin, J. N. Israelachvili, and D. R. Clarke, "Estimating the metal-ceramic van der Waals adhesion energy," *Philosophical Magazine A*, vol. 76, no. 4, pp. 715–728, 1997.

[143] A. V. Akimov, Y. Tanaka, A. B. Pevtsov, S. F. Kaplan, V. G. Golubev, S. Tamura, D. R. Yakovlev, and M. Bayer, "Hypersonic modulation of light in three-dimensional photonic and phononic band-gap materials," *Physical Review Letters*, vol. 101, no. 3, p. 033902, 2008.

[144] P. M. Jais, D. B. Murray, R. Merlin, and A. V. Bragas, "Metal nanoparticle ensembles: Tunable laser pulses distinguish monomer from dimer vibrations," *Nano Letters*, vol. 11, no. 9, pp. 3685–3689, 2011.

[145] P. J. Yunker, K. Chen, M. D. Gratale, M. A. Lohr, T. Still, and A. G. Yodh, "Physics in ordered and disordered colloidal matter composed of poly(n-isopropylacrylamide) microgel particles," *Reports on Progress in Physics*, vol. 77, p. 056601, may 2014.

[146] B. Li, F. Wang, D. Zhou, Y. Peng, R. Ni, and Y. Han, "Modes of surface premelting in colloidal crystals composed of attractive," *Nature*, vol. 531, pp. 485–488, March 2016.

[147] M. D. Murthy Peri and C. Cetinkaya, "Non-contact microsphere–surface adhesion measurement via acoustic base excitations.," *Journal of colloid and interface science*, vol. 288, pp. 432–443, aug 2005.

[148] E. Vittorias, M. Kappl, H. J. Butt, and D. Johannsmann, "Studying mechanical microcontacts of fine particles with the quartz crystal microbalance," *Powder Technology*, vol. 203, no. 3, pp. 489–502, 2010.

[149] R. Fuchs, T. Weinhart, J. Meyer, H. Zhuang, T. Staedler, X. Jiang, and S. Luding, "Rolling, sliding and torsion of micron-sized silica particles: Experimental, numerical and theoretical analysis," *Granular Matter*, vol. 16, pp. 281–297, 2014.

[150] T. M. Gronewold, "Surface acoustic wave sensors in the bioanalytical field: Recent trends and challenges," *Analytica Chimica Scta*, vol. 603, pp. 119–128, 2007.

[151] M. Hiraiwa, M. Stossel, A. Khanolkar, J. Wang, and N. Boechler, "Laser-Induced Spallation of Microsphere Monolayers," *Langmuir*, vol. 32, no. 31, pp. 7730–7734, 2016.

[152] C. Dominik and A. G. G. M. Tielens, "The Physics of Dust Coagulation and the Structure of Dust Aggregates in Space," *The Astrophysical Journal*, vol. 480, no. 2, pp. 647–673, 1997.

[153] B. Luk'yanchuk, *Laser Cleaning*. Singapore: World Scientific, 2002.

[154] A. A. Kolomenskii, H. A. Schuessler, V. G. Mikhalevich, and A. A. Maznev, "Interaction of laser-generated surface acoustic pulses with fine particles: Surface cleaning and adhesion studies," *Journal of Applied Physics*, vol. 84, no. 5, pp. 2404–2410, 1998.

[155] T. Geldhauser, F. Ziese, F. Merkt, A. Erbe, J. Boneberg, and P. Leiderer, "Acoustic laser cleaning of silicon surfaces," *Applied Physics A*, vol. 89, pp. 109–113, jul 2007.

[156] J. Wang, R. Weaver, and N. Sottos, "A parametric study of laser induced thin film spallation," *Experimental Mechanics*, vol. 42, no. 1, pp. 74–83, 2002.

[157] N. Vogel, S. Goerres, K. Landfester, and C. K. Weiss, "A convenient method to produce close- and non-close-packed monolayers using direct assembly at the air-water interface and subsequent plasma-induced size reduction," *Macromolecular Chemistry and Physics*, vol. 212, no. 16, pp. 1719–1734, 2011.

[158] L.-O. Heim, J. Blum, M. Preuss, and H.-J. Butt, "Adhesion and Friction Forces between Spherical Micrometer-Sized Particles," *Physical Review Letters*, vol. 83, no. 16, pp. 3328–3331, 1999.

[159] J. Wang, N. R. Sottos, and R. L. Weaver, "Tensile and mixed-mode strength of a thin film-substrate interface under laser induced pulse loading," *Journal of the Mechanics and Physics of Solids*, vol. 52, no. 5, pp. 999–1022, 2004.

[160] J. K. Eliason, A. Vega-Flick, M. Hiraiwa, A. Khanolkar, T. Gan, N. Boechler, N. Fang, K. A. Nelson, and A. A. Maznev, "Resonant attenuation of surface acoustic waves by a disordered monolayer of microspheres," *Applied Physics Letters*, vol. 108, no. 6, p. 061907, 2016.

[161] ASM International Handbook Committee, *ASM Handbook, Vol. 2 - Properties and Selection: Nonferrous Alloys and Special-Purpose Materials*. Materials Park, OH: ASM International, 1990.

[162] M. Pashley, "Further consideration of the DMT model for elastic contact," *Colloids and Surfaces*, vol. 12, pp. 69–77, 1984.

[163] D. S. Rimai, L. P. Demejo, and R. C. Bowen, "Adhesion-induced deformations of polymeric substrates: Particle size dependence of the contact area," *Journal of Applied Physics*, vol. 66, no. 8, pp. 3574–3578, 1989.

[164] D. S. Rimai, L. P. DeMejo, and R. C. Bowen, "Surface-force-induced deformations of monodisperse polystyrene spheres on planar silicon substrates," *Journal of Applied Physics*, vol. 68, no. 12, pp. 6234–6240, 1990.

[165] R. A. Bowling, "A theoretical review of particle adhesion," in *Particles on Surfaces 1*, pp. 129–142, New York: Plenum Press, 1989.

[166] S. D. Mesarovic and K. L. Johnson, "Adhesive contact of elastic-plastic spheres," *Journal of the Mechanics and Physics of Solids*, vol. 48, no. 2000, pp. 2009–2033, 2000.

[167] N. T. Kattamis, P. E. Purnick, R. Weiss, and C. B. Arnold, "Thick film laser induced forward transfer for deposition of thermally and mechanically sensitive materials," *Applied Physics Letters*, vol. 91, no. 17, p. 171120, 2007.

[168] L. Hu and J. Wang, "Pure-shear failure of thin films by laser-induced shear waves," *Experimental Mechanics*, vol. 46, no. 5, pp. 637–645, 2006.

[169] M. Abi Ghanem, A. Khanolkar, S. P. Wallen, M. Helwig, M. Hiraiwa, A. A. Maznev, N. Vogel, and N. Boechler, "Longitudinal eigenvibration of multilayer colloidal crystals and the effect of nanoscale contact bridges," *Nanoscale*, vol. 11, no. 12, pp. 5655–5665, 2019.

[170] G. von Freymann, V. Kitaev, B. V. Lotsch, and G. A. Ozin, "Bottom-up assembly of photonic crystals," *Chem. Soc. Rev.*, vol. 42, pp. 2528–2554, 2013.

[171] A. Klinkova, R. M. Choueiri, and E. Kumacheva, "Self-assembled plasmonic nanostructures," *Chem. Soc. Rev.*, vol. 43, pp. 3976–3991, 2014.

[172] P. Alivisatos, "The use of nanocrystals in biological detection," *Nature Biotechnology*, vol. 22, pp. 47–52, 2004.

[173] B. Sepúlveda, P. C. Angelomé, L. M. Lechuga, and L. M. Liz-Marzán, "Lspr-based nanobiosensors," *Nano Today*, vol. 4, no. 3, pp. 244 – 251, 2009.

[174] P. Jiang, J. F. Bertone, K. S. Hwang, and V. L. Colvin, "Single-crystal colloidal multilayers of controlled thickness," *Chemistry of Materials*, vol. 11, no. 8, pp. 2132–2140, 1999.

[175] J.-H. Lee, C. Y. Koh, J. P. Singer, S.-J. Jeon, M. Maldovan, O. Stein, and E. L. Thomas, "25th anniversary article: Ordered polymer structures for the engineering of photons and phonons," *Advanced Materials*, vol. 26, no. 4, pp. 532–569, 2014.

[176] F. Gallego-Gómez, V. Morales-Flórez, M. Morales, A. Blanco, and C. López, "Colloidal crystals and water: Perspectives on liquid–solid nanoscale phenomena in wet particulate media," *Advances in Colloid and Interface Science*, vol. 234, pp. 142 – 160, 2016.

[177] K. R. Phillips, G. T. England, S. Sunny, E. Shirman, T. Shirman, N. Vogel, and J. Aizenberg, "A colloidoscope of colloid-based porous materials and their uses," *Chem. Soc. Rev.*, vol. 45, pp. 281–322, 2016.

[178] We note that such "dry" colloidal crystals are not strictly colloids, even though they are typically prepared from a colloid.

[179] F. Allein, V. Tournat, V. Gusev, and G. Theocharis, "Transversal–rotational and zero group velocity modes in tunable magneto-granular phononic crystals," *Extreme Mechanics Letters*, vol. 12, pp. 65 – 70, 2017. Frontiers in Mechanical Metamaterials.

[180] L. Bonanomi, G. Theocharis, and C. Daraio, "Wave propagation in granular chains with local resonances," *Phys. Rev. E*, vol. 91, p. 033208, Mar 2015.

[181] T. Still, W. Cheng, M. Retsch, R. Sainidou, J. Wang, U. Jonas, N. Stefanou, and G. Fytas, "Simultaneous occurrence of structure-directed and particle-resonance-induced phononic gaps in colloidal films," *Phys. Rev. Lett.*, vol. 100, p. 194301, May 2008.

[182] A. Vega-Flick, R. A. Duncan, S. P. Wallen, N. Boechler, C. Stelling, M. Retsch, J. J. Alvarado-Gil, K. A. Nelson, and A. A. Maznev, "Vibrational dynamics of a two-dimensional microgranular crystal," *Phys. Rev. B*, vol. 96, p. 024303, Jul 2017.

[183] A. Vega-Flick, R. Duncan, S. Wallen, N. Boechler, C. Stelling, M. Retsch, J. Alvarado-Gil, K. Nelson, and A. Maznev, "Contact-based and spheroidal vibrational modes of a hexagonal monolayer of microspheres on a substrate," *Wave Motion*, vol. 76, pp. 122 – 133, 2018.

[184] W. Cheng, J. J. Wang, U. Jonas, W. Steffen, G. Fytas, R. S. Penciu, and E. N. Economou, "The spectrum of vibration modes in soft opals," *The Journal of Chemical Physics*, vol. 123, no. 12, p. 121104, 2005.

[185] J. Avice, C. Boscher, G. Vaudel, G. Brotons, V. Juvé, M. Edely, C. Méthivier, V. E. Gusev, P. Belleville, H. Piombini, and P. Ruello, "Controlling the nanocontact nature and the mechanical properties of a silica nanoparticle assembly," *The Journal of Physical Chemistry C*, vol. 121, no. 42, pp. 23769–23776, 2017.

[186] C. L. Poyser, T. Czerniuk, A. Akimov, B. T. Diroll, E. A. Gaulding, A. S. Salasyuk, A. J. Kent, D. R. Yakovlev, M. Bayer, and C. B. Murray, "Coherent acoustic phonons in colloidal semiconductor nanocrystal superlattices," *ACS Nano*, vol. 10, no. 1, pp. 1163–1169, 2016. PMID: 26696021.

[187] P. Ruello, A. Ayouch, G. Vaudel, T. Pezeril, N. Delorme, S. Sato, K. Kimura, and

V. E. Gusev, "Ultrafast acousto-plasmonics in gold nanoparticle superlattices," *Phys. Rev. B*, vol. 92, p. 174304, Nov 2015.

[188] M. Rey, T. Yu, R. Guenther, K. Bley, and N. Vogel, "A dirty story: Improving colloidal monolayer formation by understanding the effect of impurities at the air/water interface," *Langmuir*, vol. 35, no. 1, pp. 95–103, 2019.

[189] J.-M. Meijer, F. Hagemans, L. Rossi, D. V. Byelov, S. I. Castillo, A. Snigirev, I. Snigireva, A. P. Philipse, and A. V. Petukhov, "Self-assembly of colloidal cubes via vertical deposition," *Langmuir*, vol. 28, no. 20, pp. 7631–7638, 2012. PMID: 22515482.

[190] V. Tournat and V. E. Gusev, "Acoustics of unconsolidated model granular media: An overview of recent results and several open problems," *Acta Acustica united with Acustica*, vol. 96, no. 2, pp. 208–224, 2010.

[191] J. Yin, M. Retsch, E. L. Thomas, and M. C. Boyce, "Collective mechanical behavior of multilayer colloidal arrays of hollow nanoparticles," *Langmuir*, vol. 28, no. 13, pp. 5580–5588, 2012. PMID: 22416999.

[192] A. Merkel, V. Tournat, and V. Gusev, "Dispersion of elastic waves in three-dimensional noncohesive granular phononic crystals: properties of rotational modes," *Physical Review E*, vol. 82, no. 3, p. 031305, 2010.

[193] A. R. Goodall, M. C. Wilkinson, and J. Hearn, "Mechanism of emulsion polymerization of styrene in soap-free systems," *Journal of Polymer Science: Polymer Chemistry Edition*, vol. 15, no. 9, pp. 2193–2218, 1977.

[194] X.-D. Wang, B. Chen, H.-F. Wang, and Z.-S. Wang, "Adhesion between submicrometer polystyrene spheres," *Powder Technology*, vol. 214, no. 3, pp. 447 – 450, 2011.

[195] J. Tomas, "Adhesion of ultrafine particles—a micromechanical approach," *Chemical Engineering Science*, vol. 62, no. 7, pp. 1997 – 2010, 2007.

[196] A.-C. Hladky-Hennion, A. Devos, and M. de Billy, "Quantitative analysis of the vibration modes in a finite set of coupled spheres," *The Journal of the Acoustical Society of America*, vol. 116, no. 1, pp. 117–124, 2004.

[197] M. Haldimann, A. Luible, and M. Overend, *"Structural Use of Glass" Volume 10 of Structural Engineering Documents*. Zurich, Switzerland: IABSE, 2008.

[198] M. Hiraiwa, S. P. Wallen, and N. Boechler, "Acoustic wave propagation in disordered microscale granular media under compression," *Granular Matter*, vol. 19, no. 3, p. 62, 2017.

[199] J. B. Haldorsen, D. L. Johnson, T. Plona, B. Sinha, H. P. Valero, and K. Winkler, "Borehole acoustic waves," *Oilfield Review*, vol. 18, no. 1, pp. 34–43, 2006.

[200] B. O. Hardin and F. E. Richart Jr., "Elastic wave velocities in granular soils," *Journal of the Soil Mechanics and Foundations Division ASCE*, vol. 94, p. 27, 1966.

[201] W. K, "The effective elastic moduli of a random packing of spheres," *Journal of the Mechanics and Physics of Solids*, vol. 35, p. 213, 1987.

[202] J. D. Goddard, "Nonlinear Elasticity and Pressure-Dependent Wave Speeds in Granular Media," *Proceedings of the Royal Society A: Mathematical, Physical and Engineering Sciences*, vol. 430, no. 1878, pp. 105–131, 1990.

[203] D. L. Johnson, L. M. Schwartz, D. Elata, J. G. Berryman, B. Hornby, and A. N. Norris, "Linear and Nonlinear Elasticity of Granular Media: Stress-Induced Anisotropy of a Random Sphere Pack," *Journal of Applied Mechanics*, vol. 65, no. 2, p. 380, 1998.

[204] B. Velický and C. Caroli, "Pressure dependence of the sound velocity in a two-dimensional lattice of hertz-mindlin balls: Mean-field description," *Physical Review E*, vol. 65, p. 021307, Jan 2002.

[205] F. Santibanez, R. Zuñiga, and F. Melo, "Mechanical impulse propagation in a three-dimensional packing of spheres confined at constant pressure," *Physical Review E*, vol. 93, p. 012908, Jan 2016.

[206] A. Onabajo, T. Dorfmuller, and G. Fytas, "Ultrasonic and Hypersonic Dispersion in Polysiloxanes," *Journal of Polymer Science: Part B*, vol. 25, pp. 749–763, 1987.

[207] J. Bunyan, A. F. Vakakis, and S. Tawfick, "Mechanisms for impulsive energy dissipation and small-scale effects in microgranular media," *Physical Review E*, vol. 92, no. 6, p. 062206, 2015.

[208] V. Langlois and X. Jia, "Sound pulse broadening in stressed granular media," *Physical Review E*, vol. 91, no. 2, p. 022205, 2015.

[209] A. S. J. Suiker, A. V. Metrikine, and R. De Borst, "Comparison of wave propagation characteristics of the cosserat continuum model and corresponding discrete lattice models," *International Journal of Solids and Structures*, vol. 38, no. 9, pp. 1563–1583, 2001.

[210] A. Merkel and S. Luding, "Enhanced micropolar model for wave propagation in ordered granular materials," *International Journal of Solids and Structures*, vol. 106, pp. 91–105, 2017.

[211] S. P. Wallen and N. Boechler, "Shear to longitudinal mode conversion via second harmonic generation in a two-dimensional microscale granular crystal," *Wave Motion*, vol. 68, pp. 22–30, 2017.

[212] E. Hascoët, H. J. Herrmann, and V. Loreto, "Shock propagation in a granular chain," *Phys. Rev. E*, vol. 59, pp. 3202–3206, Mar 1999.

[213] R. F. Waymel, E. Wang, A. Awasthi, P. H. Geubelle, and J. Lambros, "Propagation and dissipation of elasto-plastic stress waves in two dimensional ordered granular media," *Journal of the Mechanics and Physics of Solids*, vol. 120, pp. 117–131, 2018.

[214] D. L. Blair, N. W. Mueggenburg, A. H. Marshall, H. M. Jaeger, and S. R. Nagel, "Force distributions in three-dimensional granular assemblies: Effects of packing order and interparticle friction," *Physical Review E - Statistical, Nonlinear, and Soft Matter Physics*, vol. 63, no. 4, pp. 413041–413048, 2001.

[215] S. Van Den Wildenberg, R. Van Loo, and M. Van Hecke, "Shock waves in weakly compressed granular media," *Physical Review Letters*, vol. 111, no. 21, pp. 1–5, 2013.

[216] M. Ciavarella, J. Joe, A. Papangelo, and J. R. Barber, "The role of adhesion in contact mechanics," *Journal of the Royal Society Interface*, vol. 16, no. 151, 2019.

[217] V. Tournat, V. E. Gusev, V. Y. Zaitsev, and B. Castagnède, "Acoustic second-harmonic generation with shear to longitudinal mode conversion in granular media," *Europhysics Letters (EPL)*, vol. 66, no. June, pp. 798–804, 2007.

[218] A. Saeedi Vahdat, S. Azizi, and C. Cetinkaya, "Doubling of rocking resonance frequency of an adhesive microparticle vibrating on a surface," *Applied Physics Letters*, vol. 101, no. 10, p. 101602, 2012.

[219] A. S. Vahdat, S. Azizi, and C. Cetinkaya, "Nonlinear dynamics of adhesive microspherical particles on vibrating substrates," *Journal of Adhesion Science and Technology*, vol. 27, no. 15, pp. 1712–1726, 2013.

[220] T. W. Murray and J. W. Wagner, "Laser generation of acoustic waves in the ablative regime," *Journal of Applied Physics*, vol. 85, no. 4, pp. 2031–2040, 1999.

[221] J. E. Sinclair, "Epicentre solutions for point multipole sources in an elastic half-space," *Journal of Physics D: Applied Physics*, vol. 12, pp. 1309–1315, aug 1979.

[222] P. A. Doyle, "On epicentral waveforms for laser-generated ultrasound," *Journal of Physics D: Applied Physics*, vol. 19, pp. 1613–1623, sep 1986.

[223] L. R. Gómez, A. M. Turner, M. Van Hecke, and V. Vitelli, "Shocks near jamming," *Physical Review Letters*, vol. 108, no. 5, pp. 1–5, 2012.

[224] E. Wang, P. Geubelle, and J. Lambros, "An experimental study of the dynamic elasto-plastic contact behavior of metallic granules," *Journal of Applied Mechanics, Transactions ASME*, vol. 80, no. 2, 2013.

[225] H. A. Burgoyne and C. Daraio, "Strain-rate-dependent model for the dynamic compression of elastoplastic spheres," *Physical Review E - Statistical, Nonlinear, and Soft Matter Physics*, vol. 89, no. 3, pp. 1–5, 2014.

[226] H. A. Burgoyne and C. Daraio, "Elastic-plastic wave propagation in uniform and periodic granular chains," *Journal of Applied Mechanics, Transactions ASME*, vol. 82, no. 8, pp. 1–10, 2015.

[227] T. On, P. A. Lavigne, and J. Lambros, "Development of plastic nonlinear waves in one-dimensional ductile granular chains under impact loading," *Mechanics of Materials*, vol. 68, pp. 29–37, 2014.

[228] M. Yokouchi, H. Uchiyama, and Y. Kobayashi, "Effect of tensile strain rate on the mechanical properties of polystyrene and high-impact polystryene," *Journal of Applied Polymer Science*, vol. 25, no. 6, pp. 1007–1015, 1980.

[229] S. Chizari, M. P. Lim, L. A. Shaw, S. P. Austin, and J. B. Hopkins, "Automated optical-tweezers assembly of engineered microgranular crystals," *Small*, vol. n/a, no. n/a, p. 2000314, 2020.

[230] R. G. Shimmin, A. J. DiMauro, and P. V. Braun, "Slow vertical deposition of colloidal crystals: A langmuir-blodgett process?," *Langmuir*, vol. 22, no. 15, pp. 6507–6513, 2006.

[231] S. Wong, V. Kitaev, and G. A. Ozin, "Colloidal Crystal Films: Advances in Universality and Perfection," *Journal of the American Chemical Society*, vol. 125, no. 50, pp. 15589–15598, 2003.

[232] F. Allein, V. Tournat, V. E. Gusev, and G. Theocharis, "Tunable magneto-granular phononic crystals," *Applied Physics Letters*, vol. 108, no. 16, 2016.

[233] F. Li, P. Anzel, J. Yang, P. G. Kevrekidis, and C. Daraio, "Granular acoustic switches and logic elements," *Nature Communications*, vol. 5, p. 5311, 2014.

[234] H. Hu, A. Strybulevych, J. H. Page, S. E. Skipetrov, and B. A. Van Tiggelen, "Localization of ultrasound in a three-dimensional elastic network," *Nature Physics*, vol. 4, no. 12, pp. 945–948, 2008.

[235] A. Lagendijk, B. Van Tiggelen, and D. S. Wiersma, "Fifty years of Anderson localization," *Physics Today*, vol. 62, no. 8, pp. 24–29, 2009.

[236] N. P. Bansal and R. H. Doremus, *Handbook of Glass Properties*. Orlando: Academic Press, 1986.

[237] See supplementary information at https://doi.org/10.1007/s10035-017-0744-3 for images of transducer tilt correction, estimation of excitation amplitudes, and additional plots and tables of the sound speed dependence on excitation amplitude and static load.

Appendix A

DETAILS FOR CHAPTER 2: COMPLEX CONTACT-BASED DYNAMICS OF MICROSPHERE MONOLAYERS REVEALED BY RESONANT ATTENUATION OF SURFACE ACOUSTIC WAVES

A.1 Sample Fabrication

The aluminum-coated, soda lime glass microscope slide was purchased from EMF Corp. The slide was rinsed with deionized water, acetone and isopropanol, and dried under air flow. It was then hydrophilized in a hydrogen peroxide bath (80C°) for fifteen minutes. The microspheres were purchased from Corpuscular Inc. as a suspension of 5.0 wt% in water. Prior to the deposition, the suspension was further diluted to 1.25 wt%, and was ultrasonicated for 3 minutes. The angle of the wedge formed between the substrate and the top glass slide was 3°. We deposited 40μL of the diluted suspension into the wedge. The whole setup was then placed on a tilt, such that the meniscus drying front receded upwards on an incline of 15°. The assembly was allowed to dry in ambient lab environment (40% relative humidity, 22°C). The PDMS stamp was made of Sylgard 184 with a curing agent to base ratio of 1 : 10 and left to cure in an oven at 70°C for a day to ensure solidification. The aluminum coating was deposited via electron-beam evaporation. The thickness of the evaporated aluminum layer was measured with a quartz crystal microbalance (QCM).

A.2 Sample Fabrication

The pulsed laser source used as the pump has 532 nm wavelength, 430 ps pulse duration, energy of 4μJ per pulse, and 1 kHz repetition rate. In the scanned photodeection measure-

ments, the light was focused to a spot of 1.2 mm $\times$ 20μm (axis length, at $1/e^2$ intensity level). The resulting surface displacement of the propagating SAW pulse is estimated to be 150 pm [77]. The continuous probe laser has a wavelength 514 nm and average power of 4 mW at the sample. The probe passes through the glass substrate and is focused at the aluminum film to a 6μm diameter spot (at $1/e^2$ intensity level). A balanced detection scheme is used, in which a metal coated right-angle prism acts as the knife edge for two photodetectors. The separation between the focused pump and the probe beams was 850μm. In the grating interferometer experiments, the probe has a diameter of 80μm (at $1/e^2$ intensity level) and a power of 20 mW at the sample.

A.3 Spatiotemporal Signal Processing

For the spatiotemporal data shown in Fig. 2.1 1(c-e) and Fig. 2.3 3 in Chapter 2, we compensate for the fixed pump-probe separation distance by shifting each measured signal in time by $x_s = c_R$ (where x_s is the distance from a reference position, and $c_R = 3128$ m/s is the Rayleigh wave speed in the aluminum-coated glass substrate [236]). We then zero-pad the signal at both beginning and end to obtain signals of uniform duration, and smooth with a 500 MHz bandpass filter.

A.4 Images of the Contact

Figure A.1(a-c) shows scanning electron microscope (SEM) images for the same interparticle contact in the uncoated sample, and after coating it with 20 nm and 40 nm of aluminum.

Figure A.2 shows SEM images for isolated spheres that demonstrate that the particle-substrate contact is shaded from the aluminum deposition by the microsphere.

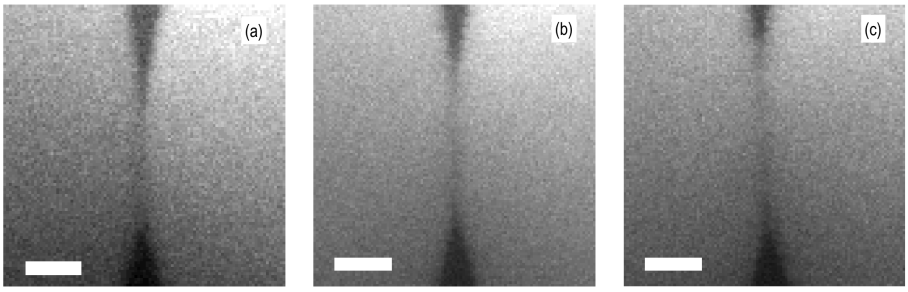

Figure A.1: (a-c) SEM images of the same interparticle contact, corresponding to the spectra of Fig. 2.2(a-c) in Chapter 2, respectively. The scale bar is 100 nm.

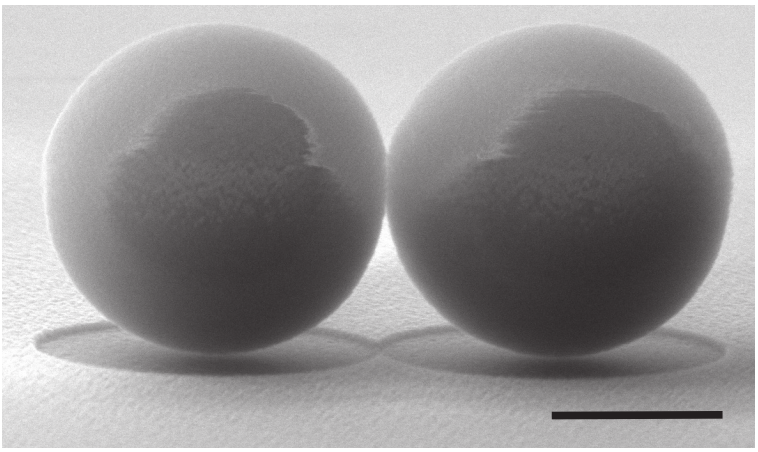

Figure A.2: SEM images showing the particle-substrate contact is shaded from the aluminum deposition. The scale bar is 1μm.

A.5 Material Properaties Used in Calculations

A Young's modulus of $E_1 = 73$ GPa and shear modulus of $G_1 = 31$ GPa were used for the silica microspheres [236], and moduli $E_2 = 62$ GPa and $G_2 = 25$ GPa were used for the aluminum-coated substrate [161]. The microsphere mass was calculated using a density for silica of $\rho = 2.0$ g/cm^3, as provided by the manufacturer. For the calculation of the dispersion

curves, the following parameters were used: longitudinal wave speed in the substrate c_L = 5574 m/s, transverse wave speed in the substrate c_T = 3438 m/s [2], substrate density ρ_s = 2.5 g/cm^3 [197], and unit cell area of $A_s = \sqrt{3}D^2/2$. For the estimation of contact stiffnesses from adhesive contact models, we use work of adhesions $w = 0.094$ J/m^2 between silica and alumina [77] (assuming a native oxide layer on the aluminum), and w = 0.063 J/m^2 between silica particles [121].

A.6 Contact Resonance Frequencies

The frequencies of the identified attenuation maxima are listed in Table A.1. Each maximum was identified based on when the transmission spectra reaches a specified threshold for each of the three resonances. However, due to asymmetry in many of the transmission dips and noise in the measured spectra these frequencies should be considered as approximate. Table A.2 lists the fitted contact resonance frequencies plotted in Fig. 2.2 and Fig. 2.4 of the main text.

Table A.1: Frequencies of the measured attenuation maxima.

Aluminum (nm)	0	20	40
f_I (MHz)	49	53	61
f_I (MHz)	108	106	106
f_I (MHz)	197	242	290

Table A.2: Fitted contact resonance frequencies.

Aluminum (nm)	0	20	40
f_{HR} (MHz)	48	54	66
f_N (MHz)	108	106	106
f_{RH} (MHz)	209	213	233

A.7 Images of the Contact Network

Fig. A.3 shows scanning electron microscope (SEM) images of the microsphere contact network.

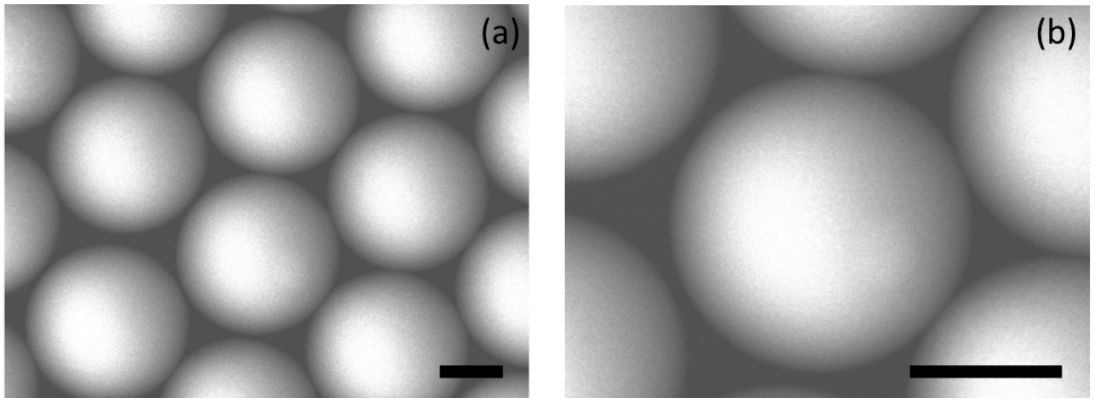

Figure A.3: SEM images of the microsphere contact network. (b) Zoomed image of the center of (a). The scale bar in both panels is 1μm.

Appendix B

DETAILS FOR CHAPTER 3: LASER-INDUCED SPALLATION OF MICROSPHERE MONOLAYERS

B.1 Interferometric signal processing procedure

The inteferometric signal measured for a pump energy of 32 mJ (corresponding to the data presented in Fig. 3.1(c) of the main text), is shown in Fig. B.1(a). The arrival of the acoustic pulse at the sample surface causes surface displacements, such that the interferometer's output intensity is altered. The measured interferometer signal intensity is related to the surface displacement by:

$$V(t) = \frac{V_{max} + V_{min}}{2} + \frac{V_{max} - V_{min}}{2}\sin(\frac{4\pi u(t)}{\lambda_0} + \phi) \tag{B.1}$$

where V_max and V_min are the maximum and minimum measured interferometric signal when the inteferometer is in- and out-of-phase, respectively, ϕ is the phase angle, λ_0 is the wavelength of the probe laser, and $u(t)$ is the surface displacement [156]. We smooth the photodetector output by applying a moving average filter with a span of 60 data points, as shown in Fig. B.1(a). The surface displacements are found by solving the above equation for $u(t)$, which is smoothed with a span of 100 data points, as shown in Fig. B.1(b). The surface velocity is obtained by numerical differentiation of the smoothed surface displacements, and is again smoothed with a span of 100 data points, as shown in Fig. B.1(c). Lastly, the acceleration is obtained by numerical differentiation of the smoothed surface velocity, after which, the data is smoothed with a span of 100 data points, as shown in Fig. B.1(d). With the rigid body model, the maximum tensile force occurs at the point of minimum acceleration,

as shown by the marker in Fig. B.1(d). The error for individual spallation experiments is determined by finding the difference between smoothed and unsmoothed curves at the point of minimum acceleration. This is then averaged across all 10 spallation experiments and multiplied by the microsphere mass to obtain the average error due to smoothing. The total error associated with the inertial force at the spallation threshold of 32 mJ is calculated by summing the average smoothing error and the standard deviation of the maximum tensile inertial force of all 10 spallation experiments.

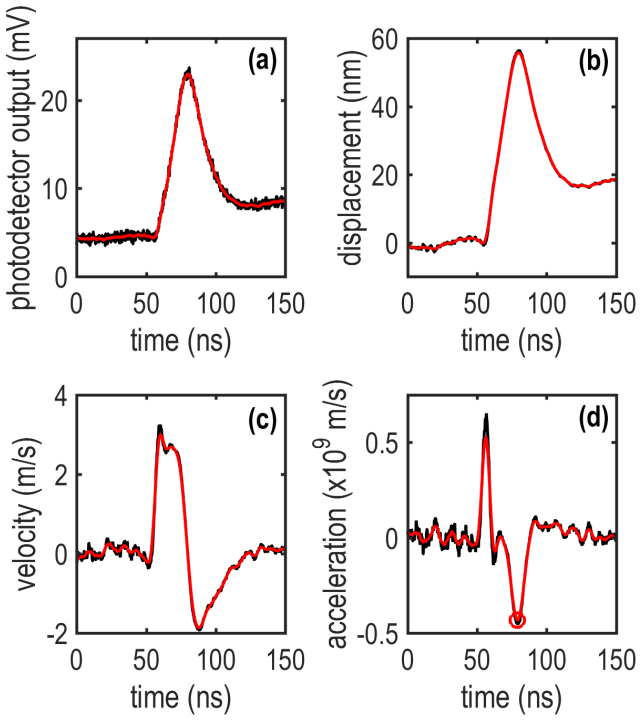

Figure B.1: (a) Photodetector output from the interferometer for a pump energy of 32 mJ. (b) Surface displacements. (c) Surface velocity. (d) Surface acceleration. The marker in (d) denotes the point of maximum deceleration. Black and red lines are the unsmoothed and smoothed signals, respectively.

Appendix C

DETAILS FOR CHAPTER 4: LONGITUDINAL EIGENVIBRATION OF MULTILAYER COLLOIDAL CRYSTALS AND THE EFFECT OF NANOSCALE CONTACT BRIDGES

C.1 Sample Fabrication

The aluminum-coated soda lime glass substrates were cleaned by soaking in isopropanol and acetone for ten minutes each, and then rinsed with deionized (DI) water and dried under nitrogen flow. Following this, the substrates were coated with a 20-nm-thick silica layer via chemical vapor deposition. The colloidal suspensions for these samples were purified by centrifuging the suspension at 4000 rpm, discarding the supernatant and redispersing the particles in DI water or ethanol. This purification procedure was repeated three times for all samples, except in the case of Sample 2, where the colloidal suspension was centrifuged once. Details of the self-assembly parameters and the layer thicknesses characterized for the multilayer samples in this study are listed in Table C.1. The samples with the microsphere suspension in water were left to dry in an oven at 75C°, while the samples immersed in the ethanol suspension were placed under a plastic container to avoid external air flows and left to dry under ambient laboratory conditions.

Table C.1: Details of sample fabrication parameters for the multilayer samples.

Sample	Concentration (%v/v)	Solvent	Drying Environment	Centrifuged	Layer Thicknesses Characterized	Monolayer Resonance Detected
1	0.2	Ethenol	Ambient	3x	1,2,3,4,5,7,8,12	Yes
2	0.01	DI Water	Over, 75°C	1x	1,2,3,4,5,9,12	Yes
3	1	Ethanol	Ambient	3x	6,7	No
4	0.5	Ethanol	Ambient	3x	2,3,4,5,6,7,8,9	No
5	0.3	Ethanol	Ambient	3x	2,3,4,5,6,7,9	No
6	0.01	DI Water	Oven, 75°C	3x	2,3,4	No
7	0.01	DI Water	Oven, 75°C	3x	2,3,4,5,6	No

C.2 Laser Ultrasonic Setup Details

For the measurements on Sample 2, the pump beam was focused to an elliptical spot (436μm $\times$ 76μm at the $1/e^2$ intensity level), whereas for all the other samples, the pump beam was focused to a 200μm diameter circular spot. The interferometric signals were averaged over 10^4 pump pulses for all samples, except in the case of the measurements on the monolayer, five-, seven-, eight- and twelve-layer regions of Sample 1, which were averaged over 10^6 pump pulses to achieve an improved signal-to-noise ratio.

C.3 Signal Processing Procedure

Time-resolved signals were recorded at a positive and negative phase setting by varying the optical path difference between the probe and the reference beams via a rotating fused silica window placed in the path of the probe beam. The net signal was obtained by subtracting the averaged waveforms collected at positive and negative phase settings. A segment of 0.75μs of the signal starting from the sharp initial rise (corresponding to the arrival of the pump pulse) was used for further signal processing. This segment of the signal was zero-padded after the oscillations completely decayed below the noise floor, differentiated with respect to time to remove the thermal decay component from the signal, and normalized with respect to its maximum amplitude. A Fast Fourier Transform (FFT) was then applied to the normalized signal.

C.4 Work of Adhesion At TheSphere-Substrate and Sphere-Sphere Interfaces

We estimate the work of adhesion between identical polystyrene microspheres w_{P-P} and that between the polystyrene microspheres and the silica-coated substrate w_{P-S} in terms of the Hamaker constant A, using $w = \frac{A}{12\pi {D_0}^2}$ ($D_0 = 0.165$ nm is a standard value used for the interfacial cutoff separation distance for a variety of media [121]). This coeffcient takes into account the van der Waals forces between the two surfaces in contact. The expression for the Hamaker constant A_{131} for two polystyrene surfaces (denoted as medium 1) interacting across medium 3 (air) is:

$$A_{131} = \frac{3kT}{4}\left(\frac{\epsilon_1 - \epsilon_3}{\epsilon_1 + \epsilon_3}\right)^2 + \frac{3h\nu_{e1}}{16\sqrt{(2)}}\frac{({n_1}^2 - {n_3}^2)^2}{({n_1}^2 + {n_3}^2)^{3/2}} \tag{C.1}$$

where $T = 293$ K is room temperature, $\nu_{e1} = 2.3 \cdot 10^{15}$ Hz is the main electronic absorption frequency of polystyrene in the UV, k is Boltzmann's constant, h is Planck's constant, $\epsilon_1 = 2.55$ F/m and $\epsilon_3 = 1.0$ F/m are the permittivities of polystyrene and air, respectively, and $n_1 = 1.56$ and $n_3 = 1.00$ are the refractive indices of polystyrene and air, respectively. All of the preceding constants are tabulated in Ref. [121]. Using Eq. C.1, we calculate $A_{131} = 6.53 \cdot 10^{-20}$ J. This gives a work of adhesion $w_{P-P} = 0.06$ J/m^2 between the polystyrene microspheres.

Similarly, we use Eq. C.1 to calculate the Hamaker constant for two silica surfaces (denoted as medium 2) interacting in air (medium 3), with the corresponding material properties of silica: permittivity $\epsilon_2 = 3.8$ F/m, refractive index $n_2 = 1.45$, and electronic absorption frequency in the UV $\nu_{e2} = 3.2 \cdot 10^{15}$ Hz [121]. We obtain $A_{232} = 6.36 \cdot 10^{-20}$ J. We use a combining relation to obtain an approximate value for the Hamaker constant between polystyrene and silica, $A_{132} \approx \sqrt{A_{131}A_{232}}$, such that $A_{132} \approx 6.44 \cdot 10^{-20}$ J. The corresponding work of adhesion between polystyrene and silica is $w_{P-S} = 0.06$ J/m^2.

C.5 Calculation of the effective Interlayer Contact Stiffness Using the DMT Model

The normal contact stiffness between two colloidal particles $G_{N,DMT}$ is derived from the linearized force-displacement curve prescribed by the DMT model [138], and is expressed as, $G_{N,DMT} = \frac{3}{2}(2\pi w_{P-P} {R_e}^2 {E^*_{P-P}}^2)^{1/3}$ where w_{P-P} is the work of adhesion between the two polystyrene surfaces, R_e is the effective radius (equal to half the radius of the particle), and E^*_{P-P} is the effective modulus of the contact and is defined in terms of the Young's modulus E_P and the Poisson's ratio ν_P of the particle, $E^*_{P-P} = \frac{2}{3}\frac{E_P}{1-{\nu_P}^2}$. The effective interlayer normal contact stiffness $G_{e,DMT}$ is then derived by accounting for the contributions of the three normal $G_{N,DMT}$ and transverse G_S contact springs each in an HCP unit cell along the out-of-plane direction to be $G_{e,DMT} = G_{N,DMT}(2 + \nu^*)$. where $\nu^* = \frac{G_S}{G_{N,DMT}} = 2\frac{1-\nu_P}{2-\nu_P}$ is the ratio of the interparticle shear and normal contact stiffnesses [137, 192].

C.6 Estimation of Displacement Amplitude in the Aluminum Film

We estimate the thermoelastic strain in the aluminum film induced by the pump laser pulse using the relation in reference [161], $\eta_0 = 3\kappa\alpha_L(1-R)/(A_P C\xi_0\rho_0 {c_L}^2)$, where $\kappa = 67.6$ GPa is the bulk modulus, $\alpha_L = 23.1\mu$m/m$\cdot K$ is the linear thermal expansion coefficient, $\rho_0 = 2.7$ g/cm^3 is the density, $C = 2.46$ MJ/m^3, K is the volumetric heat capacity, $R = 0.92$ is the optical intensity reflection coefficient, $\xi_0 = 6.8$ nm is the optical penetration depth, $c_L = 6300$ m/s is the longitudinal wave speed in aluminum [161], A_P is the area of the pump spot, and $Q = 7$ μJ/pulse is the pump pulse energy at the sample. From the thermoelastic strain, we estimate the displacement in the aluminum film to be $u_z = \eta_0\xi_0 = 340$ pm.

Appendix D

DETAILS FOR CHAPTER 5: ACOUSTIC WAVE PROPAGATION IN DISORDERED MICROSCALE GRANULAR MEDIA UNDER COMPRESSION

D.1 Experiment list

Tabulated lists of the experiments conducted, which detail the measured multilayer thicknesses T, absolute measured sound speeds $C_{L,min}$ at the minimum static loads (based on the measured thickness), maximum conditioning static loads F_C, maximum measurement static loads F_{max}, and the marker colors used in Figs. 5.5, 5.7, and 5.8, are given in Tables D.1 and D.2 for the pre- and post-collapse cases, respectively.

Table D.1: Pre-collapse multiayer thicknesses, absolute sound speeds $C_{L,min}$ at the minimum static load, maximum conditioning loads F_C used during cyclic loading, and maximum static loads F_{max} used in amplitude dependence measurements. Marker color refers to Figs. 5.5 and 5.8(a) in the main text.

Exp.	T (μm)	$C_{L,min}$ (m/s)	F_C (N)	F_{max} (N)	Color
#1	180	990	3.1	3.2	Pink
#2	180	970	3.1	3.1	Grey
#3	180	1100	2.0	2.0	Brown
#4	180	900	2.0	2.0	Yellow

Table D.2: Post-collapse multiayer thicknesses, absolute sound speeds $C_{L,min}$ at the minimum static load, maximum conditioning loads F_C used during cyclic loading process, and maximum static loads F_{max} used in amplitude dependence measurements. Marker color refers to Figs. 5.7 and 5.8(b) in the main text.

Exp.	T (μm)	$C_{L,min}$ (m/s)	F_C (N)	F_{max} (N)	Color
#1	42	600	6.4	6.3	Pink
#2	48	1100	6.4	6.2	Grey
#3	36	710	6.4	6.3	Brown
#4	56	1000	6.4	2.0	Blue

Tabulated lists that detail the samples, and positions on those samples, tested for each experiment for the pre- and post-collapse cases are listed in Tables D.3 and D.4, respectively. All post-collapse experiments (except #4) were performed directly after pre-collapse experiments of the same number, e.g., after completing pre-collapse experiment #1, the multilayer was immediately collapsed and post-collapse experiment #1 was conducted.

Table D.3: Sample, and position on that sample, tested for each experiment in the pre-collapse case. Experiment #5 denotes the position dependence experiments as detailed in Appendix D.2.

Exp.	Sample	Region
#1	1	1
#2	1	2
#3	2	1
#4	2	2
#5	2	4

Table D.4: Sample, and position on that sample, tested for each experiment in the post-collapse case. Experiment #5 denotes the position dependence experiments as detailed in Appendix D.2.

Exp.	Sample	Region
#1	1	1
#2	1	2
#3	2	1
#4	2	3
#5	2	4

D.2 Position Dependence

Sound speed measurements are conducted at five locations arranged in a cross pattern across the transducer with a spacing of 0.25 mm, namely, left, center, right, up, and down. All experiments, except for the ones listed in Table D.5, are performed at the center location. The experimental procedure is the same as presented in Sec. 5.3 of the main text, although fewer (4) static loads are measured. The power law exponent β at each position, its mean $\bar{\beta}$, and ratio of standard deviation σ_β to $\bar{\beta}$, is shown in Table D.5.

Table D.5: Position dependence of the power law exponent β at five positions along transducer surface, as a function of the collapse state (e.g. pre- and post-).

State	Left	Center	Right	Up	Down	$\bar{\beta}$	σ_β / $\bar{\beta}$
Pre	0.01	0.04	0.03	0.01	0.03	0.02	0.62
Post	0.21	0.07	0.04	0.02	0.22	0.11	0.82

D.3 Discrete Element Model Simulations

A statically compressed chain of adhesive spheres can be modeled as a one-dimensional lattice of point masses interacting via nonlinear springs that follow the Hertzian force-displacement law [52]. For identical spheres of mass m, the equation of motion of the displacement x_n of the n^{th} sphere is given by

$$m\ddot{x}_n = A[\alpha_0 + x_{n-1} - x_n]_+^{3/2} - A[\alpha_0 + x_n - x_{n+1}]_+^{3/2},$$

where $A = R^{1/2}[(3/2)((1-\nu^2)/E)]^{-1}$ is a constant that depends on the geometric and material properties of the spheres and R is the effective radius of contact, equal to half the sphere radius [75]. For the material properties of silica, we use a Young's modulus of $E = 73$ GPa and a Poisson's ratio of $\nu = 0.17$ [236]. We use a density of $\rho = 2.0$ g/cm^3, as provided by the manufacturer. The subscript $(+)$ indicates that the bracketed terms vanish if their arguments become negative, indicating loss of contact.

We consider left and right boundaries with prescribed displacements $d(t)$ and 0, respectively, where $d(t)$ is the displacement of the excited surface (determined experimentally, see Ref. [237]). The equations of motion of the left and right boundary spheres (having displacements x_1 and x_N, respectively), are given by:

$$\begin{aligned} m\ddot{x}_1 &= A[\alpha_0 + d(t) - x_1]_+^{3/2} - A[\alpha_0 + x_1 - x_2]_+^{3/2} \\ m\ddot{x}_N &= A[\alpha_0 + x_{N-1} - x_N]_+^{3/2} - A[\alpha_0 + x_N]_+^{3/2}. \end{aligned}$$

For Fig. 5.10, external static loads applied to the chain range from 0.83 μN to 22 μN, and for Fig. 5.11, $F_{min} = 0.25$ N and $F_{max} = 2.0$ N are considered by applying static loads of 0.85 μN and 6.89 μN to the chain, respectively. Adhesion is accounted for by adding a constant force of $F_{adh} = 0.20$ μN in all simulations. The external static loads applied

to the chain are found by dividing the total static loads applied to the transducer by the number of spheres that cover the transducer area, assuming hexagonal-close-packing. The static overlap, as a function of adhesive force F_{adh} and externally applied static load F_0, is $\alpha_0 = ((F_{adh} + F_0)/(A))^{2/3}$, according to the Hertzian contact model [75]. Assuming total static loads of $F_{min} = 0.25$ N and $F_{max} = 2.0$ N, we find static overlaps of $\alpha_{0,min} = 0.95$ nm and $\alpha_{0,max} = 3.4$ nm.

D.4 Transducer Tilt Correction With PDMS Blacking Slab

The role of the PDMS backing slab in our experiment is to compensate for slight misalignment between the Au-coated transducer and the sample, such that contact uniformity is improved between the transducer and the multilayer. To illustrate the effectiveness of this approach, microscope images are taken looking at the interface between the transducer and an Al-coated slide. Initially the Au-coated transducer is nearly brought into contact with the Al-coated slide, such that a small gap remains, as shown in Fig. D.1(a). We first observe uniform contact along the entire length of the Au-coated transducer edge at a static load of 0.08 N, as shown in Fig. D.1(b), which is well below the minimum static load of 0.25 N used in our experiments.

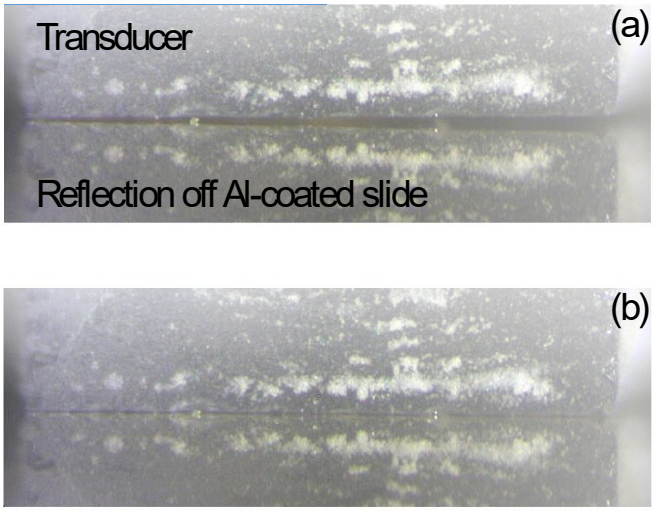

Figure D.1: Microscope images of the transducer being compressed against an Al-coated slide in the experimental setup just prior to contact (a) and at a static load of 0.08 N (b)

D.5 Excitation Amplitude

We estimate the excitation amplitudes by calibrating the interferometer sensitivity and measuring the free surface displacements of an Au-coated slide. Following [136], the sensitivity is calculated as:

$$dV_{sig}/du = (V_{max} - V_{min})\frac{\pi}{\lambda} \tag{D.1}$$

where V_{sig} is the measured photodetector output voltage of the interferometer due to the acoustic signal, u is the displacement normal to the surface, V_{max} is the photodetector output voltage at constructive interference, V_{min} is the photodetector output voltage at destructive interference, and $\lambda = 514$ nm is the wavelength of the probe. From Eq. D.1, we find the maximum displacements of the high- and low-amplitude signals to be 1.9 nm and 0.51 nm, respectively.

D.6 Measured Dependence of Sound Speed on Excitation Amplitude

Tables D.6 and D.7 list the measured dependence of sound speed on excitation amplitude and static load, as shown in Fig. 5.10 in Chapter 5, for the pre- and post-collapse states, respectively.

Table D.6: Pre-collapse percent increase in sound speed for high amplitude relative to low amplitude excitation for each experiment as a function of static load, where the F_{max} is listed in Table D.1.

Exp.	Increase at F_{min} (%)	Increase at F_{max} (%)
#1	1.7	0.53
#2	1.2	0.26
#3	0.12	-0.63
#4	1.8	0.038

Table D.7: Post-collapse percent increase in sound speed for high amplitude relative to low amplitude excitation for each experiment as a function of static load, where the F_{max} is listed in Table D.2.

Exp.	Increase at F_{min} (%)	Increase at F_{max} (%)
#1	5.1	2.7
#2	7.5	0.72
#3	2.8	-0.61
#4	1.9	0.15

D.7 Additional Plots of the Simulated Sound Speed Dependence on Excitation Amplitude and Static Load

We simulate the sound speed as a function of excitation amplitude for static loads of $F_{min} =$ 0.25 N and $F_{max} = 2.0$ N. In our simulation, the excitation amplitude is varied from 0.038 nm to 76 nm, and the sound speed is determined by probing the 90th and 25th spheres for the pre- and post-collapse cases, respectively. The results are shown in Fig. D.2, with the experimental excitation amplitudes indicated by the vertical lines.

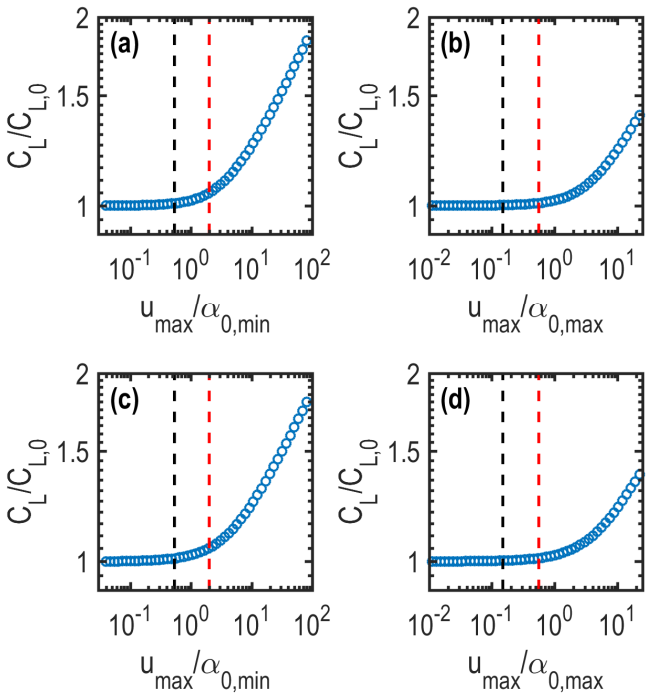

Figure D.2: Sound speed C_L (normalized by the sound speed at the lowest excitation amplitude $C_{L,0}$ versus maximum excitation amplitude u_{max} for the pre-collapse case at static loads of F_{min} (a) and F_{max} (b), and the post-collapse case at static loads of F_{min} (c) and F_{max} (d). Black and red dashed lines represent the maximum excitation amplitude of the low- and high-amplitude excitations, respectively. The excitation amplitude u_{max} has been scaled by the static overlap at the minimum ($\alpha_{0,min}$) or maximum ($\alpha_{0,max}$) static load. The minimum and maximum applied static loads are set to $F_{min} = 0.25$ N and $F_{max} = 2.0$ N, respectively.